University of Alberta

Inhomogeneous Superconductivity

by

Lucian Covaci 

A thesis submitted to the Faculty of Graduate Studies and Research
in partial fulfillment of the requirements for the degree of

Doctor of Philosophy

Department of Physics

Edmonton, Alberta
Fall 2006

Your file Votre référence
ISBN: 978-0-494-23010-7
Our file Notre référence
ISBN: 978-0-494-23010-7

Abstract

We have studied the effects of inhomogeneities like surfaces, interfaces and disorder on the properties of s-wave and d-wave superconductors. The description of such inhomogeneous scenarios is very important, as they have a big influence on experimental observations. Tunneling experiments on the surface of superconductors will have a direct look into these peculiar surface states, like the zero bias conductance peak and the Andreev bound states.

Using the tight-binding Extended Hubbard Hamiltonian, we numerically solve the discretized Bogoliubov-de Gennes equations applied to various inhomogeneous problems. We use simplifications due to the symmetries of surfaces, to solve problems like superconductivity near a surface, the giant proximity effect and the formation of Andreev bound states. Full two-dimensional calculations are employed to describe rough surfaces, finite size systems and the localization of the Andreev bound states in finite size samples.

We find that the order parameter near surfaces exhibits Friedel-like oscillations on the order of the Fermi wavelength, and that interference effects occur in finite size systems. Major differences between the properties of d-wave superconductors near the (100) surface as compared to the (110) surface are uncovered. Zero energy bound states are present not only at the (110) surface of a d-wave superconductor, but also in a normal metal layer sitting on top of a d-wave superconductor. We demonstrate that rough surfaces of d-wave superconductors will acquire zero energy bound states at any surface orientation. We observe that Andreev bound states form in a normal metal when it is in proximity to a superconductor, and we show that in the case of finite size systems these states are localized in different locations depending on their energy.

Table of Contents

TABLE OF CONTENTS

List of Figures

LIST OF FIGURES

Chapter 1

Introduction

Our knowledge about the existence of superconductivity came into being in 1911 when Kamerlingh Onnes [1] discovered that the resistance of Hg drops sharply when cooled below 4K. Since then, superconductivity was observed in a large variety of materials from simple elements to complex compounds. These materials can be grouped in several types depending either on their properties or on the magnitude of their critical temperature.

One group holds the conventional superconductors, discovered early in the history of the field, which have low critical temperature. We can list here simple elements like Hg ($T_c = 4.2$K), Pb ($T_c = 7.2$K), Al ($T_c = 1.17$K), alloys like Nb_3Ge ($T_c = 23$K) and the recently discovered MgB_2 ($T_c = 39$K).

Another group holds the so called high-T_c superconductors (HTS). The first high-T_c superconductor developed was the $La_{2-x}Ba_xCuO_4$ compound discovered in 1986 by Bednorz and Müller [2] and had a critical temperature of around 36K. In a short period of time it became clear that ceramics based on the La_2CuO_4 insulating parent compound, $La_{2-x}A_xCuO_4$ with A = Ba, Sr, Ca, exhibit superconductivity [3]. The critical temperature was subsequently increased with the development of a multitude of layered pervoskite compounds having as a common building block the CuO_2 planes. The HTS also include $YBa_2Cu_3O_{7-y}$ (YBCO) with $T_c = 90$K [4], $Bi_2Sr_2Ca_2CuO_8$ (BSCCO) with $T_c = 92$K [5], $Tl_2Ba_2Ca_2Cu_3O_{10}$ with $T_c = 128$K [6] and $HgBa_2Ca_3Cu_3O_{8+\delta}$ with the highest critical temperature , $T_c = 138$K, known so far [7].

Other known types of superconductors are the heavy fermion superconductors, like $CeCu_2Si_2$ [8], UBe_{13} [9] and UPt_3 [10], all with critical temperatures around 1K, and the organic superconductors like $(BEDT\text{-}TTF)_2Cu(NCS)_2$ [11] with $T_c = 10.4$K.

All these superconductors have a common electronic property, which is the pairing of electrons. The pairing can be between electrons with opposite spin and momenta for singlet superconductors (conventional and HTS) and same spin but opposite momenta for triplet superconductors (heavy fermion). In the conventional superconductors, the pairing is established to be due to interactions between electrons and phonons. Even

though, in the last two decades, an impressive amount of research has been dedicated to the understanding of the microscopic pairing mechanism in HTS, it is still being debated.

The superconducting state is a quantum mechanical coherent state, described by off-diagonal long range order [12]. From a thermodynamic point of view the transition from normal to superconducting state is a continuous phase transition. For superconductivity, the order parameter is defined by an anomalous average $< c_{k\uparrow}c_{-k\downarrow} >$, describing the pairing between electrons. A continuous phase transition is usually accompanied by a spontaneous symmetry breaking. For example, for a ferromagnet the order parameter is the spontaneous magnetization. Above the critical temperature, the spontaneous magnetization is zero, but upon cooling, the ferromagnet becomes magnetized and loses the directional symmetries it had. The symmetry to be broken in a superconductor is the gauge symmetry. Below the critical temperature, the order parameter of the superconductor has the same phase throughout the entire sample. The ordered state is always less symmetric than the normal state.

Superconductivity is usually defined in the thermodynamic limit (infinite system), but questions regarding properties of real superconductors near interfaces, surfaces and impurities might arise. In our view inhomogeneities are defined by whatever breaks the translational symmetry in any or all directions. Inhomogeneous systems are those that contain surfaces, interfaces, impurities and disorder. There is also a growing interest in mesoscopic and nanoscale devices, as they promise great technological advances. Unfortunately, this field is still mostly limited to experimental manipulations. As the size of the studied systems become smaller and smaller, the influence of the surface states is not negligible anymore. In the description of superconducting nano-wires and dots, one is obliged to take in account the inhomogeneous character of the system.

Inhomogeneities can have a strong effect on the experimental measurements. Some experiments might probe directly inhomogeneities, and thus it is important to be able to describe superconductivity in all these inhomogeneous scenarios and then subsequently to be able to explain the experimental results.

Several experimental techniques are well suited for probing surfaces and inhomogeneous systems. Among these techniques are transport measurements, and more exactly tunneling experiments. It has been demonstrated [13, 14] early in the field, that the dI/dV characteristic will be a direct measure of the density of states in the superconductor. Tunnelling experiments are an important tool mostly because they have a high energy resolution limited only by the thermal smearing and because they can detect both occupied an unoccupied states around the Fermi surface. These experiments can be classified into different categories: scanning tunneling microscopy/spectroscopy (STM), thin-film junctions, grain boundary junctions, point contact junctions and break junctions. The most valuable tool is the scanning tunnelling microscope because it has atomic-scale resolution and is able to gather both spectroscopic and geometrical data from measurements on surfaces.

One important difference between the conventional superconductors and the HTS is the symmetry of the order parameter. The conventional superconductors have an isotropic s-wave order parameter, while the order parameter in the HTS is momentum dependent and has a d-wave symmetry. The determination of the d-wave symmetry is a difficult task because standard methods, like the angle resolved photo emission spectroscopy (ARPES) or the measurement of the penetration depth, specific heat and of the thermal conductance, will only shine light on the magnitude of the order parameter. Phase sensitive methods were developed in order to address the question. The d-wave symmetry of YBCO was demonstrated with the use of tri-crystal HTS experiments [15]. In these experiments a scanning SQUID-system was used to show that flux quanta are half-integer in superconducting rings formed by three differently oriented HTS grains separated by grain boundary Josephson junctions. Of utmost importance in these experiments was the phase dependence of the order parameter and the peculiarities near a surface.

Opposite to s-wave superconductors, for which the orientation of the surface does not influence significantly the properties at the surface, the d-wave superconductors show dramatic changes in the local density of states near the surface. The most important feature is the appearance of a large zero bias conductance peak (ZBCP) at the (110) surface of a HTS [16–19]. The existence of the ZBCP was explained by the formation of an Andreev state at the surface [20]. This is due to the change in sign of the order parameter felt by a quasi-particle scattering on the surface. In addition to the existence of the ZBCP, some experiments also report that the ZBCP becomes split at low temperatures [21, 22]. This feature is explained by specific surface properties, namely the appearance of an induced extended s-wave component phase shifted by $\pi/2$. The induced state is one in which time-reversal symmetry is broken [23–25].

Because there is a significant difference between the properties of quasiparticles at the (100) and (110) interfaces of a d-wave superconductor, the ability to describe rough surfaces is also very important. In practice every surface is rough on a larger scale, usually the surface shows facets, sometimes of atomic sizes. A rough (100) surface will present regions with (110) orientation, and vice-versa. In addition, different step-like structures might appear, like the ones present in (210) or (220) surfaces. The presence of the ZBCP even for (100) surfaces [22, 26, 27] was an indication that rough surfaces are inevitable and that they have a significant influence on the surface states. In another experiment the roughness of a (110)-interface is varied by ion irradiation [28]. Surprisingly the ZBCP broadens only weakly with increasing roughness, whereas its height is clearly reduced.

Josephson junctions in HTS can be obtained either from thin-film junctions or by using intrinsic junctions formed in a HTS sample, namely the grain boundary junctions; a comprehensive review of grain boundary junctions has been published [29]. For Josephson junctions between unconventional superconductors, interesting effects were observed because of the phase dependent order parameters [30, 31]. Different orienta-

tions of the superconductors will give rise to surprising effects. A review of these effects is presented in several review articles [32, 33].

Another class of inhomogeneities are the impurities either non-magnetic or magnetic. A review of impurity induced states in superconductors can be found in a recent paper [34]. The presence of impurities in conventional s-wave superconductors was shown not to influence the critical temperature if their concentration is low. According to the Anderson theorem [35] superconductivity is robust in disordered conventional superconductors. Although this theorem applied mostly in the thermodynamic limit by considering averages over the impurity configurations, local variations of the order parameter around impurities are observed. For superconductors with short coherence length, it has been found that Anderson's theorem is actually violated [36–38].

The influence of impurities in d-wave superconductors is more drastic, mainly because of the scattering of nodal quasi-particles on the impurities. It was initially predicted that strong non-magnetic and magnetic scatterers will produce localized bound states near the impurities [39–41]. This was observed directly in STM experiments on BSCCO surfaces doped with non-magnetic Zn impurities [42–44]. Strong ZBCP located near the Zn impurities are observed, giving an indication of the Andreev scattering on the impurities and of the d-wave nature of the order parameter. Such ZBCP in the STM spectra is not observed for impurities in conventional superconductors [45].

Although STM experiments obtain local information about the superconducting state, a method was developed in order to link the real-space measurements with the momentum-space quantities. This was done by Fourier transforming the STM data. Around the impurities, the LDOS and the order parameter exhibit Friedel-like oscillations, and as the impurity concentration rises, these oscillations will interfere and thus create standing waves on the surface of the superconductor. By Fourier transforming the STM spectra one can obtain momentum-space information about the scattering of quasiparticles with the impurities. This was first done in STM experiments Be(0001) surfaces [46], and then extended to STM data on BSCCO surfaces [47–49].

Another important manifestation of inhomogeneities is the intrinsic disorder of the HTS compounds. Disorder is inevitable in HTS because they are complex materials with a large number of atoms per unit lattice, with a high uncertainty in the location of the oxygen dopants. Granular superconductivity has been observed in recent STM experiments on underdoped BSCCO [50, 51]. Regions with small superconducting gaps are embedded into regions with large gaps suggesting that the underdoped BSCCO is a mixture of two electronic states. Furthermore, the configuration of oxygen dopants has been observed to be correlated with the gap disorder configuration [52]. It is expected that such inhomogeneities are present in all HTS superconductors.

From a theoretical point of view, the methods needed to describe inhomogeneous superconductors need to be quantum mechanical and real-space methods. Among these methods are the Ginzburg-Landau equations, the Gorkov equations and their quasiclassical approximation and the Bogoliubov de Gennes equations.

The earliest method used in the treatment of surfaces in superconductors is the Ginzburg Landau method [53]. This method arises from the fact that the superconducting transition is a continuous phase transition and the order parameter varies continuously as a function of temperature. Ginzburg and Landau introduced the order parameter as a macroscopic wave function, ψ for the whole superconductor. They expanded the free energy around T_c in terms of $\psi\psi^*$. In order to describe inhomogeneous systems, they considered the wave function to be space dependent. The Ginzburg-Landau equations are obtained by minimizing the free energy with respect to the order parameter. The main limitation of this method is that it is valid only near the critical temperature. This method has been used widely to describe superconductivity near surfaces, and the superconducting proximity effect [54, 55].

Soon after the Bardeen, Cooper, Schrieffer (BCS) solution for the conventional superconductor was presented [56], Gor'kov developed a Green's function method which recovers not only the BCS solution, but also the Ginzburg Landau equations for temperatures near T_c [57, 58]. Besides the usual electron Green's function he introduced the so called anomalous Green's function which describes superconducting correlations. The Gor'kov equations are obtained from the equations of motion, $i\hbar\dot{\psi} = [\psi, H]$, along with a Hartree-Fock mean field factorization of the interaction terms in the Hamiltonian. The Gor'kov equations involving the Green's functions are second order partial differential equations.

An important simplification of Gor'kov's equations can be made if the superconductor is subjected to weak perturbations and the order parameter varies slowly in space and time. This approximation is known as the quasiclassical Green's function method and was developed for the superconducting state by Eilenberger [59–61]. The Eilenberger equations for the quasiclassical Green's functions are simpler than the Gor'kov ones, as they are only ordinary differential equations. An even simpler version is obtained in the case of dirty superconductors, namely the Usadel equations [62]. Unfortunately, the quasi-classical approximation is valid on scales greater than the zero temperature coherence length, ξ_0, which must be assumed to be greater than the Fermi wavelength $\hbar/p_F$. This is certainly true in conventional superconductors but not for HTS which have a very short coherence length, on the order of the lattice constant. In some scenarios, like the rough surface one, due to the formation of atomic size facets, the quasi-classical method is not available. Another difficulty in using the quasi-classical method is the fact that boundary conditions at surfaces and interfaces must be put in by hand, taken from microscopic calculations. This method has been widely applied to various interface problems and is able to explain the general features of surfaces and interfaces in superconductors.

The most powerful method, but also the most difficult to solve, is the direct usage of the Bogoliubov de Gennes (BdG) equations [63]. These equations are in fact equivalent to Gor'kov's equations but they are written for the wave function of the system. By using a tight binding Hamiltonian, the equations are trivially discretized and ready to be

used in numerical calculations. The discretization allows for rapid variations of the order parameter, and does not need special boundary conditions.The method used throughout this work is the discretized version of the BdG equations applied to finite size system and to surfaces with various orientations.

The remainder of the thesis is organized in the following manner:

Chapter 2

- We start with the description of the extended Hubbard Hamiltonian and present the relevance of this effective Hamiltonian to the high-T_c superconductors. Next we give an overview of the homogeneous s-wave and d-wave superconductivity starting from the inhomogeneous real-space formulation of superconductivity. We also introduce the self-consistent Bogoliubov de Gennes equations in the discretized matrix form and show how different physical quantities can be calculated in the inhomogeneous scenario.

Chapter 3

- We describe the numerical methods used in order to solve the BdG equations. These include not only the simplifications introduced by various types of surfaces (100, 110 and c-axis), but also a full calculation on two-dimensional systems. We also introduce a Recursion Method, which is very useful when large systems are considered.

Chapter 4

- We present numerical results for various inhomogeneous problems. First we consider the effect of surfaces (100 and 110) on both s-wave and d-wave superconductivity. A fundamental difference exists between these symmetries at the (110) surface, where a Zero Bias Conductance Peak (ZBCP) is observed for d-wave superconductors. Rough surfaces and their influence on the formation of the ZBCP are also considered. Next, driven by the experimental discovery of a "giant proximity effect", we model a tri-layer comprised of strong/weak/strong superconductors and calculate the temperature dependence of the leaking distance in the middle layer and of the Josephson critical current. Superconducting pockets in the middle layer are considered and the Josephson current is calculated self-consistently. Finally, we discuss the formation of Andreev Bound States (ABS) in s-wave and d-wave superconductors. We consider various surface orientations and describe differences in the formation of the ABS at these surfaces. Finite size samples with a normal metal region embedded in a superconductor having different shapes are used in order to study the localization of the Andreev states.

Chapter 5

- We conclude with a summary of our results and make suggestions for improvements in future calculations.

Chapter 2

Theoretical aspects

2.1 The BCS model of superconductivity

Macroscopic quantum phenomena such as superconductivity and superfuidity occur because of the off-diagonal long range order [12]. The correlations are off-diagonal because of the non-zero anomalous averages like $\langle cc \rangle$ and $\langle c^\dagger c^\dagger \rangle$. The fundamental concept behind superconductivity was first introduced by Cooper in 1956 [64]. Even before the appearance of the BCS solution [56,65], Cooper showed that two interacting electrons in the presence of a filled Fermi sea will form a bound state. In contrast to the case of two free electrons, the Cooper pair will be bound for any finite strength of an attractive interaction. Bardeen, Cooper and Schrieffer (BCS) showed that in such a state the pairing is between electrons of opposite spin and momentum. The pair can form a singlet with total spin $S = 0$ (in the conventional electron-phonon and the high-T_c superconductors) or a triplet with total spin $S = 1$ (in ^3He and the heavy fermion superconductors). The order becomes long range when the pair-pair correlation function, $\langle c^\dagger_{i\uparrow} c^\dagger_{i\downarrow} c_{j\downarrow} c_{j\uparrow} \rangle$, is non-zero for $|R_i - R_j| \to \infty$. The pairs are correlated, and the order parameter $\Delta = \langle cc \rangle$ has the same phase throughout the system. The system is in a macroscopic quantum coherent state.

Because the electrons are paired, the ground state wave function of a superconductor must be constructed from pairs of electrons. Considering $N_e/2$ pairs with opposite momenta and spin, in the second quantization language the superconducting ground state wave-function can be constructed as:

$$\Psi_{N_e} = \sum_{k_1} \cdots \sum_{k_{N/2}} g_{k_1} \cdots g_{k_{N/2}} c^\dagger_{k_1\uparrow} c^\dagger_{-k_1\downarrow} \cdots c^\dagger_{k_{N/2}\uparrow} c^\dagger_{-k_{N_e/2}\downarrow} |0\rangle, \tag{2.1}$$

where $|0\rangle$ is the vacuum state and $c^\dagger_{k\uparrow}$ creates an electron with momentum k and spin $\uparrow$. The term $|c^\dagger_{k_1\uparrow} c^\dagger_{-k_1\downarrow}|0\rangle$ will describe a state with two paired electrons. The wave-function (2.1), although easy to understand is difficult to use. The main progress in

solving the problem of superconductivity was achieved when BCS introduced a slightly different wave-function:

$$|\Psi_{BCS}\rangle = \prod_k (u_k + v_k c^\dagger_{k\uparrow} c^\dagger_{-k\downarrow})|0\rangle. \tag{2.2}$$

The normalization condition of the wave function $\langle |\Psi_{BCS}\rangle|^2 = 1$ constrains the values of u_k and v_k to obey a normalization relation:

$$|u_k|^2 + |v_k|^2 = 1. \tag{2.3}$$

The normal state wave function describing a filled Fermi sea will be recovered if:

$$\begin{aligned} u_k &= 0, v_k = 1 \, for \, k < k_F \\ u_k &= 1, v_k = 0 \, for \, k > k_F \end{aligned}$$

The main difference between these two wave functions is reflected in the number of electrons these wave functions describe. Equation (2.1) describes a superconducting state with $N_e/2$ pairs of electrons, while equation (2.2) describes a state which contains all the possible number of pairs from 0 to $N_e/2$.

To see this, we need to calculate the average number of electrons in the BCS wave function which is given by:

$$\overline{N_e} = \langle \Psi_{BCS}|\hat{N}|\Psi_{BCS}\rangle \tag{2.4}$$

where $\hat{N}$ is the number operator $\hat{N} = \sum_{k\sigma} n_{k\sigma}$ with $n_{k\sigma} = c^\dagger_{k\sigma} c_{k\sigma}$ which in the case of fermions is either 0 or 1. Substituting Eq. (2.2) in Eq. (2.4) the average number of electrons becomes:

$$\overline{N_e} = \sum_k 2|v_k|^2. \tag{2.5}$$

Fluctuations in the number of particles for the BCS wave function can be calculated using the number operator:

$$\sqrt{var(\overline{N_e})} = \sqrt{\overline{N_e^2} - \overline{N_e}^2} \sim \sqrt{\overline{N_e}}. \tag{2.6}$$

Because in a typical material the number of electrons is large $\overline{N_e} \sim 10^{23}$, fluctuations around the average number of electron are negligible. Within a grand canonical formulation of the theory, by imposing the average number of particles through the use of the chemical potential, we can use the BCS wave function (2.2) instead of the fixed number of particles wave function (2.1). The absence of large fluctuations promoted BCS to the use of a mean-field formulation of superconductivity.

The Hamiltonian used by BCS for describing pairing of electrons in a solid was written in momentum space and has the following form:

$$\mathcal{H} = \sum_{k\sigma} \epsilon_k c^\dagger_{k\sigma} c_{k\sigma} + \sum_{kk'} V_{kk'} c^\dagger_{k\uparrow} c^\dagger_{-k\downarrow} c_{-k'\downarrow} c_{k'\uparrow} \tag{2.7}$$

where $V_{kk'}$ is the pairing potential and in general is momentum dependent. This form is called the "reduced form" because the lowest energy states, corresponding to zero center of mass momentum of the pair, are considered. The electrons forming the pair have opposite momenta and spins.

The Hamiltonian used by BCS is an effective Hamiltonian describing quasiparticle interactions in the context of a Fermi liquid. All normal state electron-electron interactions are incorporated in the fermionic quasiparticles. In conventional superconductors the origin of the attractive interactions between the electrons is to be found in the electron-phonon interactions. A theory of such interactions was first developed by Fröhlich [66]. The phonon mediated interaction between electrons was shown to be attractive for energies smaller than the Debye energy, $\hbar\omega_D$, which is much smaller than the Fermi energy. One of the electrons pertaining to the pair polarizes the lattice while the second one feels an effective attraction due to the deformation of the lattice.

2.2 The extended Hubbard Hamiltonian

High-T_c superconductors are complex materials with a large number of atoms in the unit cell. Although there exists a wide variety of high-T_c superconductors with transition temperatures ranging from less than $40K$ to above $130K$, their main feature is the presence of CuO_2 planes. It is believed that superconductivity resides in the CuO_2 planes and that the symmetry of the order parameter should reflect the symmetry of the CuO_2 planes (Figure 2.1). Details of the nature of the pairing symmetry in high-T_c superconductors has been uncovered experimentally [15]. It is widely accepted that the superconducting order parameter has d-wave symmetry. Even though the exact microscopic pairing mechanism is not yet known, for the purpose of this work we are only interested in an effective theory, which describes real-space pairing and exhibits anisotropic pairing potentials.

In real space, the high-T_c superconductors can be modeled with the use of an effective Hamiltonian. Since the discovery of high-T_c superconductors, different variations of the Hubbard Hamiltonian have been used. In our study we will use the extended Hubbard Hamiltonian [67], which captures the main feature of such Hamiltonians, namely nearest neighbor interactions between electrons:

$$\mathcal{H} = \sum_{\langle i,j\rangle\sigma} (-t_{ij} - (\mu - \xi_i)\delta_{ij}) c^\dagger_{i\sigma} c_{j\sigma} + \sum_i U_i n_{i\uparrow} n_{i\downarrow} + \frac{1}{2} \sum_{\langle i,j\rangle\alpha\beta} V_{ij} n_{i\alpha} n_{j\beta} \tag{2.8}$$

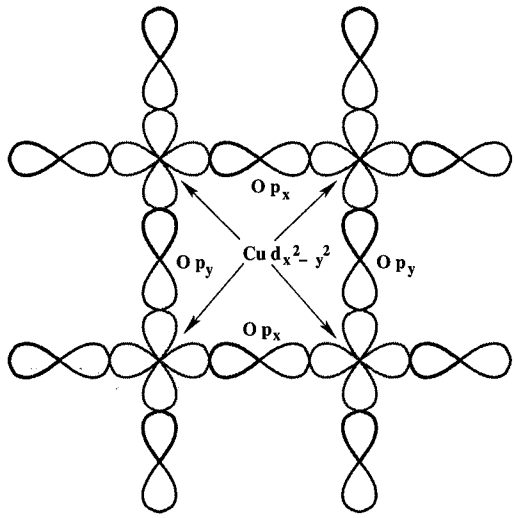

Figure 2.1: Square lattice formed in the CuO_2 plane by the hybridization of Cu $d_{x^2-y^2}$ orbitals and O p_x or p_y orbitals

where $\langle i, j \rangle$ represent the nearest neighbors, and α, β, σ represent the spin of the electrons.

The first term in the Hamiltonian describes a free electronic gas on a lattice. t_{ij} is the hopping integral which defines the kinetic energy, μ is the chemical potential which sets the filling of the system and ξ_i represents the energy of an impurity at site i. Effective interactions between electrons are introduced in the last two terms. The on-site Hubbard (U) term represents the interaction between two electrons with opposite spin sitting on the same site. The extended Hubbard Hamiltonian has an extra interaction term (V) which models effective nearest neighbor interactions. This Hamiltonian effectively describes electrons coupled with a bosonic field. Similar to the conventional superconductors where electrons polarize the lattice, the electrons polarize the bosonic field, which in turn interacts with the electrons. This way the electrons might experience short-range attractive correlations which can in some cases overcome the repulsive Coulomb correlations.

The extended Hubbard Hamiltonian even though simple in its formulation is hard to describe in a full many-body theory. Usually the first approximation done is the Hartree-Fock mean-field decomposition. Following the mean-field prescription, a 2-body term, which contains 4 electron operators becomes, a 1-body term multiplied with a mean-field, which has to be calculated self-consistently. In the mean-field approximation, an operator can be replaced by its average plus fluctuations around this average. For example, for superconducting correlations we have:

$$c_{i\uparrow}c_{i\downarrow} = \langle c_{i\uparrow}c_{i\downarrow} \rangle + (c_{i\uparrow}c_{i\downarrow} - \langle c_{i\uparrow}c_{i\downarrow} \rangle), \tag{2.9}$$

where the second term is considered to be a fluctuation term and second and higher orders are neglected.

For the on-site interaction, the mean-field decomposition gives:

$$\begin{aligned} n_{i\uparrow}n_{i\downarrow} &= c^{\dagger}_{i\uparrow}c_{i\uparrow}\langle c^{\dagger}_{i\downarrow}c_{i\downarrow}\rangle + \langle c^{\dagger}_{i\uparrow}c_{i\uparrow}\rangle c^{\dagger}_{i\downarrow}c_{i\downarrow} \\ &+ c^{\dagger}_{i\uparrow}c^{\dagger}_{i\downarrow}\langle c_{i\downarrow}c_{i\uparrow}\rangle + \langle c^{\dagger}_{i\uparrow}c^{\dagger}_{i\downarrow}\rangle c_{i\downarrow}c_{i\uparrow} \\ &- c^{\dagger}_{i\uparrow}c_{i\downarrow}\langle c^{\dagger}_{i\downarrow}c_{i\uparrow}\rangle - \langle c^{\dagger}_{i\uparrow}c_{i\downarrow}\rangle c^{\dagger}_{i\downarrow}c_{i\uparrow} \end{aligned} \tag{2.10}$$

where $\langle..\rangle$ represents both a quantum average and a thermal average. The magnetic interactions are irrelevant in this study, we set $\langle c^{\dagger}_{i\uparrow}c_{i\downarrow}\rangle = 0$. The mean fields obtained for the on-site interactions are the superconducting order parameter, Δ^{0}_{i},

$$\Delta_i = U_i\langle c_{i\downarrow}c_{i\uparrow}\rangle, \tag{2.11}$$

and a Hartree shift $U^{Hartree}_{0i\sigma}$, which will modify the chemical potential:

$$U^{Hartree}_{0i\sigma} = U_i\langle n_{i-\sigma}\rangle. \tag{2.12}$$

The same procedure can be applied the nearest neighbor interaction:

$$\begin{aligned} n_{i\alpha}n_{j\beta} &= c^{\dagger}_{i\alpha}c_{i\alpha}\langle c^{\dagger}_{j\beta}c_{j\beta}\rangle + \langle c^{\dagger}_{i\alpha}c_{i\alpha}\rangle c^{\dagger}_{j\beta}c_{j\beta} \\ &+ c^{\dagger}_{i\alpha}c^{\dagger}_{j\beta}\langle c_{j\beta}c_{i\alpha}\rangle + \langle c^{\dagger}_{i\alpha}c^{\dagger}_{j\beta}\rangle c_{j\beta}c_{i\alpha} \\ &- c^{\dagger}_{i\alpha}c_{j\beta}\langle c^{\dagger}_{j\beta}c_{i\alpha}\rangle - \langle c^{\dagger}_{i\alpha}c_{j\beta}\rangle c^{\dagger}_{j\beta}c_{i\alpha} \end{aligned} \tag{2.13}$$

For the non-local interaction term, we neglect magnetic interactions, $\langle c^{\dagger}_{i\uparrow}c_{j\downarrow}\rangle = 0$, and consider only singlet superconductivity, $\langle c_{i\alpha}c_{j\alpha}\rangle = 0$.

We define the non-local mean-fields, the superconducting order parameters, $\Delta^{\downarrow\uparrow}_{ij}$ and $\Delta^{\uparrow\downarrow}_{ij}$,

$$\Delta^{\downarrow\uparrow}_{ij} = \frac{V_{ij}}{2}\langle c_{i\downarrow}c_{j\uparrow}\rangle, \tag{2.14}$$

$$\Delta^{\uparrow\downarrow}_{ij} = \frac{V_{ij}}{2}\langle c_{i\uparrow}c_{j\downarrow}\rangle, \tag{2.15}$$

the Hartree shift which modifies the chemical potential, $U^{Hartree}_{i\sigma}$,

$$U^{Hartree}_{i\sigma} = \sum_{\delta}\frac{V_{ii+\delta}}{2}\langle n_{i+\delta-\sigma}\rangle, \tag{2.16}$$

where δ are the nearest neighbors of i, and the Fock shift which will modify the nearest neighbor hopping, $U^{Fock}_{ij\sigma}$:

$$U^{Fock}_{ij\sigma} = \frac{V_{ij}}{2}\langle c^{\dagger}_{i\sigma}c_{j\sigma}\rangle. \tag{2.17}$$

Using the above defined mean-fields the Hamiltonian can be written as a one-body Hamiltonian and will describe electrons moving in the potentials defined by the average interactions of the electron with the system:

$$\mathcal{H} = \sum_{\langle ij\rangle\sigma}[-\bar{t}_{ij}-\delta_{ij}(\bar{\mu}-\xi_i)]c^{\dagger}_{i\sigma}c_{j\sigma}+\sum_{i}(\Delta_i c^{\dagger}_{i\uparrow}c^{\dagger}_{i\downarrow}+h.c.)+\sum_{\langle ij\rangle}[(\Delta^{\uparrow\downarrow}_{ij}c^{\dagger}_{j\downarrow}c^{\dagger}_{i\uparrow}+\Delta^{\downarrow\uparrow}_{ij}c^{\dagger}_{j\uparrow}c^{\dagger}_{i\downarrow})+h.c.] \tag{2.18}$$

where $\bar{t}_{ij} = t_{ij} + U^{Fock}_{ij\sigma}$ and $\bar{\mu} = \mu + U^{Hartree}_{0i\sigma} + U^{Hartree}_{i\sigma}$. Because our main goal is to describe superconductivity, from this point forward we will neglect the Hartree-Fock shifts, as they only modify the nearest-neighbor hopping and the chemical potential. These shifts will not affect the properties of the superconducting order parameters.

2.3 Homogeneous s-wave and d-wave superconductivity

Before considering an inhomogeneous system we are interested in exploring the properties of a homogeneous two dimensional electronic system with periodic boundary conditions, modeled by the extended Hubbard Hamiltonian. The parameters in the Hamiltonian will now be independent of position, $t_{ij} = t$, $\xi_i = 0$, $U_i = U$ and $V_{ij} = V$. By Fourier transforming all the spatial operators, the momentum space Hamiltonian can be written as (see Appendix A):

$$\mathcal{H} = \frac{1}{N}\sum_{k\sigma}(\epsilon_k - \mu)c^{\dagger}_{k\sigma}c_{k\sigma} + \frac{1}{N}\sum_{k}(\Delta_k c^{\dagger}_{k\uparrow}c^{\dagger}_{-k\downarrow} + h.c.), \tag{2.19}$$

where

$$\Delta_k = \frac{1}{N}\sum_{k'} V_{kk'}\langle c_{-k'\downarrow}c_{k'\uparrow}\rangle. \tag{2.20}$$

with N being the total number of lattice sites. The pairing potential parameter $V_{kk'}$ is in general a function of momentum:

$$V_{kk'} = U + V\gamma_{k-k'}, \tag{2.21}$$

but for $2D$ lattices and Hamiltonians with nearest-neighbor terms, the pairing potential parameter can be separated into orthogonal components:

$$V_{kk'} = U + \frac{V}{4}\gamma_k\gamma_{k'} + \frac{V}{4}\eta_k\eta_{k'} + 2V\sin k_x a \sin k'_x a + 2V \sin k_y a \sin k'_y a, \tag{2.22}$$

where $\gamma_k = 2(\cos k_x a + \cos k_y a)$ and $\eta_k = 2(\cos k_x a - \cos k_y a)$.

The Hamiltonian Eq. (2.19) can be diagonalized by using a canonical transformation introduced by Bogoliubov [68] and Valatin [69]. The transformation will substitute

electron operators with fermion operators (γ) that will describe the excitations of the superconductor:

$$c_{k\uparrow} = u_k^{\star}\gamma_{k\uparrow} + v_k\gamma_{-k\downarrow}^{\dagger} \tag{2.23}$$

$$c_{-k\downarrow} = u_k^{\star}\gamma_{-k\downarrow} - v_k\gamma_{k\uparrow}^{\dagger} \tag{2.24}$$

where u_k and v_k are complex numbers. The inverse transformation can be also written:

$$\gamma_{k\uparrow} = u_k c_{k\uparrow} - v_k c_{-k\downarrow}^{\dagger} \tag{2.25}$$

$$\gamma_{-k\downarrow} = u_k c_{-k\downarrow} + v_k c_{k\uparrow}^{\dagger} \tag{2.26}$$

The canonical transformation will preserve the properties of the operators, meaning that the γ-operators are fermionic operators and they obey the following anti-commutation relations:

$$\{\gamma_{q\sigma}, \gamma_{q'\sigma'}^{\dagger}\} = \delta_{kk'}\delta_{\sigma\sigma'}, \tag{2.27}$$

$$\{\gamma_{q\sigma}, \gamma_{q'\sigma'}\} = 0, \tag{2.28}$$

$$\{\gamma_{q\sigma}^{\dagger}, \gamma_{q'\sigma'}^{\dagger}\} = 0, \tag{2.29}$$

A condition for u_k and v_k can be obtained if we calculate the anti-commutator $\{\gamma_{k\uparrow}, \gamma_{k\uparrow}^{\dagger}\} = 1$. Inserting Eq. (2.25) into Eq. (2.27) we obtain:

$$|u_k|^2\{c_{k\uparrow}, c_{k\uparrow}^{\dagger}\} + |v_k|^2\{c_{-k\downarrow}, c_{-k\downarrow}^{\dagger}\} = 1, \tag{2.30}$$

and using once-again the fermionic anti-commutation relations the relation between u_k and v_k is:

$$|u_k|^2 + |v_k|^2 = 1. \tag{2.31}$$

It is interesting to see how the γ operators act on the BCS wave-function (2.2):

$$\begin{aligned}
\gamma_{k\uparrow}|\Phi_{BCS}\rangle &= (u_k c_{k\uparrow} - v_k c_{-k\downarrow}^{\dagger})\prod_{k'}(u_{k'} + v_{k'}c_{k'\uparrow}^{\dagger}c_{-k'\downarrow}^{\dagger})|0\rangle \\
&= (u_k c_{k\uparrow} - v_k c_{-k\downarrow}^{\dagger})(u_k + v_k c_{k\uparrow}^{\dagger}c_{-k\downarrow}^{\dagger})\prod_{k'\neq k}(u_{k'} + v_{k'}c_{k'\uparrow}^{\dagger}c_{-k'\downarrow}^{\dagger})|0\rangle \\
&= 0
\end{aligned} \tag{2.32}$$

and similarly

$$\begin{aligned}
\gamma_{-k\downarrow}|\Phi_{BCS}\rangle &= (u_k c_{-k\downarrow} + v_k c_{k\uparrow}^{\dagger})\prod_{k'}(u_{k'} + v_{k'}c_{k'\uparrow}^{\dagger}c_{-k'\downarrow}^{\dagger})|0\rangle \\
&= (u_k c_{-k\downarrow} + v_k c_{k\uparrow}^{\dagger})(u_k + v_k c_{k\uparrow}^{\dagger}c_{-k\downarrow}^{\dagger})\prod_{k'\neq k}(u_{k'} + v_{k'}c_{k'\uparrow}^{\dagger}c_{-k'\downarrow}^{\dagger})|0\rangle \\
&= 0.
\end{aligned} \tag{2.33}$$

Because there are no excitations in the BCS ground state of the superconductor, meaning that all the electrons are paired, the γ destruction operators acting on the ground state will give zero.

If we calculate the $\gamma^\dagger$ creation operators we get:

$$\begin{aligned}
\gamma^\dagger_{k\uparrow}|\Phi_{BCS}\rangle &= (u^\star_k c^\dagger_{k\uparrow} - v^\star_k c_{-k\downarrow}) \prod_{k'} (u_{k'} + v_{k'} c^\dagger_{k'\uparrow} c^\dagger_{-k'\downarrow})|0\rangle \\
&= (u^\star_k c^\dagger_{k\uparrow} - v^\star_k c_{-k\downarrow})(u_k + v_k c^\dagger_{k\uparrow} c^\dagger_{-k\downarrow}) \prod_{k'\neq k} (u_{k'} + v^\star_{k'} c^\dagger_{k'\uparrow} c^\dagger_{-k'\downarrow})|0\rangle \\
&= c^\dagger_{k\uparrow} \prod_{k'\neq k} (u_{k'} + v_{k'} c^\dagger_{k'\uparrow} c^\dagger_{-k'\downarrow})|0\rangle \qquad (2.34)
\end{aligned}$$

and

$$\begin{aligned}
\gamma^\dagger_{-k\downarrow}|\Phi_{BCS}\rangle &= (u^\star_k c^\dagger_{-k\downarrow} + v^\star_k c_{k\uparrow}) \prod_{k'} (u_{k'} + v_{k'} c^\dagger_{k'\uparrow} c^\dagger_{-k'\downarrow})|0\rangle \\
&= (u^\star_k c^\dagger_{-k\downarrow} + v^\star_k c_{k\uparrow})(u_k + v_k c^\dagger_{k\uparrow} c^\dagger_{-k\downarrow}) \prod_{k'\neq k} (u_{k'} + v_{k'} c^\dagger_{k'\uparrow} c^\dagger_{-k'\downarrow})|0\rangle \\
&= c^\dagger_{-k\downarrow} \prod_{k'\neq k} (u_{k'} + v_{k'} c^\dagger_{k'\uparrow} c^\dagger_{-k'\downarrow})|0\rangle. \qquad (2.35)
\end{aligned}$$

There will be two types of excitations, one given by $\gamma^\dagger_{k\uparrow}$ which destroys a pair from the condensate and creates an electron with momentum k and spin $\uparrow$. The second type of excitations, given by $\gamma^\dagger_{-k\downarrow}$, will also destroy a pair and create an electron with momentum $-k$ and spin $\downarrow$. In the superconducting state, the quasiparticles defined by Eq. (2.25) and Eq. (2.26) will be mixture of electron-like operators ($c_{k\uparrow\dagger}$) and hole-like creation operators ($c_{-k\downarrow}$).

Using the Bogoliubov-Valatin transformation (2.23)-(2.24) , we can rewrite the Hamiltonian (2.19) in terms of quasiparticle operators and find a set of u_k's and v_k's for which the Hamiltonian is diagonal,

$$\begin{aligned}
\mathcal{H} &= \frac{1}{N}\sum_k (\epsilon_k - \mu)(|u_k|^2 - |v_k|^2)(\gamma^\dagger_{k\uparrow}\gamma_{k\uparrow} + \gamma^\dagger_{-k\downarrow}\gamma_{-k\downarrow}) \\
&+ (\Delta_k u_k v^\star_k + \Delta^\star_k u^\star_k v_k)(\gamma^\dagger_{k\uparrow}\gamma_{k\uparrow} + \gamma^\dagger_{-k\downarrow}\gamma_{-k\downarrow}) \\
&+ [2(\epsilon_k - \mu)u^\star_k v^\star_k - v^{\star 2}_k \Delta_k + u^{\star 2}_k \Delta^\star_k]\gamma_{k\uparrow}\gamma_{-k\downarrow} \\
&+ [2(\epsilon_k - \mu)u_k v_k - v^2_k \Delta^\star_k + u^2_k \Delta_k]\gamma^\dagger_{-k\downarrow}\gamma^\dagger_{k\uparrow}. \qquad (2.36)
\end{aligned}$$

The Hamiltonian will become diagonal if the coefficients of $\gamma_{k\uparrow}\gamma_{-k\downarrow}$ and $\gamma^\dagger_{-k\downarrow}\gamma^\dagger_{k\uparrow}$ are set to zero:

$$2(\epsilon_k - \mu)u_k v_k - v^2_k \Delta^\star_k + u^2_k \Delta_k = 0. \qquad (2.37)$$

Dividing Eq. (2.37) by u_k^2 we obtain an equation of order 2 in v_k/u_k:

$$-\left(\frac{v_k}{u_k}\right)^2 \Delta_k^\star + 2(\epsilon_k - \mu)\left(\frac{v_k}{u_k}\right) + \Delta_k = 0. \tag{2.38}$$

The solution of this quadratic equation is given by:

$$\left(\frac{v_k}{u_k}\right) = \frac{E_k - (\epsilon_k - \mu)}{\Delta_k^\star}, \tag{2.39}$$

where we have defined $E_k = \sqrt{(\epsilon_k - \mu)^2 + |\Delta_k|^2}$. Using the previous condition for u_k and v_k, $|u_k|^2 + |v_k|^2 = 1$, we can write down the solution:

$$|u_k|^2 = \frac{1}{2}\left(1 + \frac{\epsilon_k - \mu}{E_k}\right) \tag{2.40}$$

$$|v_k|^2 = \frac{1}{2}\left(1 - \frac{\epsilon_k - \mu}{E_k}\right). \tag{2.41}$$

Using these solutions, we can rewrite the k-space Hamiltonian (2.36):

$$\mathcal{H} = E_0 + \frac{1}{N}\sum_k E_k(\gamma_{k\uparrow}^\dagger \gamma_{k\uparrow} + \gamma_{-k\downarrow}^\dagger \gamma_{-k\downarrow}), \tag{2.42}$$

where E_0 is the ground state energy. The Hamiltonian is now diagonal and describes quasiparticle excitations of superconductor. In the superconducting state, for which $\Delta_k \neq 0$, the energies of the excitations are gapped. For a quasiparticle with momentum k, the lowest excitation energy will be $|\Delta_k|$. This will show up directly in the local density of states, which for s-wave superconductors has a momentum independent gap of size $2|\Delta_0|$ and which for d-wave superconductors is gapless.

The order parameter can also be written as a function of the quasiparticle operators. The Bogoliubov-Valatin transformations are to be inserted in Eq. (2.20) to give the k-dependent order parameter:

$$\Delta_k = \frac{1}{N}\sum_{k'} V_{kk'} u_{k'}^\star v_{k'}(1 - \langle\gamma_{k'\uparrow}^\dagger \gamma_{k'\uparrow}\rangle - \langle\gamma_{-k'\downarrow}^\dagger \gamma_{-k'\downarrow}\rangle) \tag{2.43}$$

where $\langle..\rangle$ are quantum mechanical averages at zero temperature or both quantum mechanical and thermal averages at finite temperature. The averages $\langle\gamma_{k'\uparrow}\gamma_{-k'\downarrow}\rangle$ and $\langle\gamma_{k'\uparrow}\gamma_{-k'\downarrow}\rangle$ vanish because of the fermionic nature of the quasiparticles.

At $T = 0$ the superconductor is in the ground state and there are no excited quasiparticles. The two averages from Eq. (2.43) are zero, as the quasiparticle destruction

operators are acting directly on the ground state. In this case, the order parameter attains the following form:

$$\begin{aligned}\Delta_k &= \frac{1}{N}\sum_{k'} V_{kk'} u^{\star}_{k'} v_{k'} \\ &= \frac{1}{N}\sum_{k'} V_{kk'} \frac{\Delta_{k'}}{2E_{k'}}.\end{aligned} \tag{2.44}$$

At finite temperature, quasiparticles will be excited and because they are fermionic particles, the average of the quasiparticle number operator $\langle \gamma^{\dagger}_{k'\uparrow}\gamma_{k'\uparrow}\rangle$ will obey the Fermi statistics:

$$\begin{aligned}\langle \gamma^{\dagger}_{k\uparrow}\gamma_{k\uparrow}\rangle &= f(E_k) \\ &= \frac{1}{e^{\beta E_k}+1}\end{aligned} \tag{2.45}$$

where $\beta = 1/kT$. From Eq. (2.43), the order parameter at finite temperature has the form:

$$\begin{aligned}\Delta_k &= \frac{1}{N}\sum_{k'} V_{kk'} u^{\star}_{k'} v_{k'} (1-2f(E_{k'})) \\ &= \frac{1}{N}\sum_{k'} V_{kk'} \Delta_{k'} \frac{(1-2f(E_{k'}))}{2E_{k'}}.\end{aligned} \tag{2.46}$$

The "gap equation" (2.46) , is a complex transcendental equation, as the order parameter appears in both sides of the equality and is also contained in E_k. A solution to the gap equation can only be obtained numerically.

For the system considered here, a square lattice with nearest neighbor interactions, the order parameter can be decomposed into separable components. Similar to Eq. (2.22), the gap equation can be solved by using the following ansatz:

$$\Delta_q = \Delta_0 + \Delta_s \gamma_q + \Delta_d \eta_q, \tag{2.47}$$

where Δ_0 is the on-site s-wave component, Δ_s is the extended s-wave component and Δ_d is the d-wave component; γ_q and η_q are defined below Eq. (2.22). Using the following equalities:

$$\begin{aligned}\sum_k \sin ka &= 0, \\ \sum_k \sin ka \cos ka &= 0,\end{aligned}$$

the gap equation can be decomposed into three parts:

$$\Delta_0 = \frac{1}{N}\sum_{k'} U\Delta_{k'}\frac{1-2f(E_{k'})}{2E_{k'}}, \tag{2.48}$$

$$\Delta_s = \frac{1}{N}\sum_{k'} \frac{V}{4}\gamma_{k'}\Delta_{k'}\frac{1-2f(E_{k'})}{2E_{k'}}, \tag{2.49}$$

$$\Delta_d = \frac{1}{N}\sum_{k'} \frac{V}{4}\eta_{k'}\Delta_{k'}\frac{1-2f(E_{k'})}{2E_{k'}}. \tag{2.50}$$

Progress can be achieved further if the following relations are considered:

$$\sum_k \eta_k = 0, \tag{2.51}$$

$$\sum_k \gamma_k\eta_k = 0. \tag{2.52}$$

The gap equation now becomes:

$$\Delta_0 = \frac{1}{N}\sum_{k'} U\left(\Delta_0 + \Delta_s\gamma_{k'}\right)\frac{1-2f(E_{k'})}{2E_{k'}}, \tag{2.53}$$

$$\Delta_s = \frac{1}{N}\sum_{k'} \frac{V}{4}\left(\Delta_0\gamma_{k'} + \Delta_s\gamma_{k'}^2\right)\frac{(1-2f(E_{k'})}{2E_{k'}}, \tag{2.54}$$

and

$$\Delta_d = \frac{1}{N}\sum_{k'} \frac{V}{4}\Delta_d\eta_{k'}^2\frac{(1-2f(E_{k'})}{2E_{k'}}. \tag{2.55}$$

The two different symmetries are now decoupled, the s-wave and d-wave components of the order parameter do not mix in the uniform treatment of the problem.

As shown in Figure 2.2, the momentum dependence of the order parameter differs for the s-wave as compared to the d-wave components. The on-site s-wave component is isotropic in momentum space while the extended s-wave component alternates sign as a function of the magnitude of the momentum. In contrast to the extended s-wave, the d-wave component alternates sign as a function of orientation in k-space. It has two node lines at $|k_x| = |k_y|$ with the lobes pointing in the k_x direction having negative values and the lobes in the k_y direction having positive values.

The critical temperature of the superconducting transition, for which the order parameter vanishes, can be calculated using the gap equation. There will be different critical temperatures for the s-wave and the d-wave part of the order parameter. For the s-wave components the critical temperature can be found from a system of two equations:

$$\begin{pmatrix} UC_1 - 1 & UC_2 \\ \frac{V}{4}C_2 & \frac{V}{4}C_3 - 1 \end{pmatrix}\begin{pmatrix} \Delta_0 \\ \Delta_s \end{pmatrix} = 0, \tag{2.56}$$

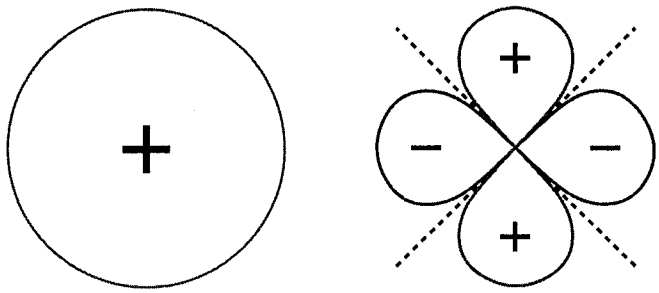

Figure 2.2: k-dependence of the on-site s-wave and d-wave components of the order parameter

where

$$C_i = \frac{1}{N}\sum_{k'} \gamma_{k'}^{i-1} \frac{1-2f_{Tc}(\epsilon_{k'}-\mu)}{2(\epsilon_{k'}-\mu)}$$

with $f_{T_c}(x) = 1/(e^{x/kT_c}+1)$.

For the d-wave component the equation that gives the critical temperature is the following:

$$\frac{1}{N}\sum_{k'} \frac{V}{4}\eta_{k'}^2 \frac{1-2f_{Tc}(\epsilon_{k'}-\mu)}{2(\epsilon_{k'}-\mu)} = 1. \tag{2.57}$$

The temperature dependence of the order parameter (Figure 2.3) can be obtained by solving numerically the gap equation. For the mean-field BCS model the temperature dependence of the order parameter is universal in the weak coupling limit for each component. The ratio $2\Delta_0/kT_c$, where Δ_0 is the order parameter at $T = 0$K, is a constant in the weak coupling limit of the BCS theory. For s-wave superconductivity $2\Delta_0/kT_c = 3.52$ while for d-wave superconductivity the ratio is $2\Delta_0/kT_c = 4.27$ [70]. Experimentally, for most of the conventional superconductors the ratio $2\Delta_0/kT_c$ is clustered between 3.5 and 4.5 while the high-T_c superconductors have a ratio $2\Delta_0/kT_c \gg 5$. This may be an indicative that most of the conventional superconductors are close to the weak-coupling regime, while the high-T_c superconductors may well be in the intermediate or strong-coupling regime.

Depending on the choice of pairing potentials, U and V, different symmetries can be more favorable energetically [67, 71]. For example if $U < 0$ and $V = 0$, the dominant component is the on-site s-wave component, while if $U \geq 0$ and $V < 0$, the d-wave component is dominant. The different symmetries of the superconducting order parameters can be observed directly from the density of states.

Turning back to the momentum dependence of the order parameter we will calculate the density of states for both s-wave and d-wave type superconductors. The density of

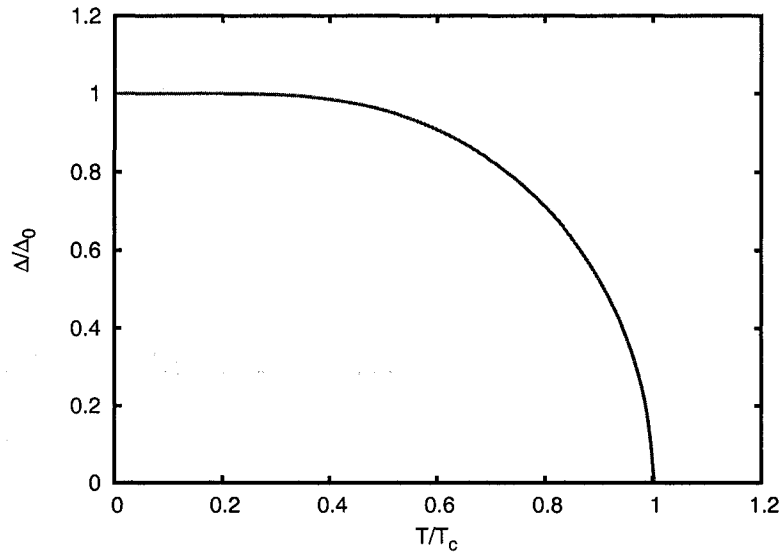

Figure 2.3: Temperature dependence of the d-wave order parameter

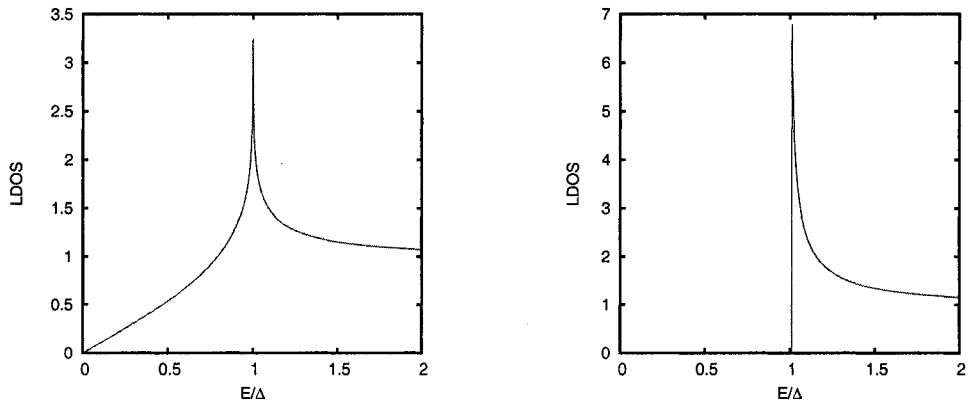

Figure 2.4: The density of states for a superconductor with s-wave (right) and d-wave (left) symmetry

states is defined as:

$$N(E) = \frac{1}{N}\sum_{k}\delta(E - E_k). \tag{2.58}$$

If we consider a large number of k-points, and assume a constant density of states in the normal state $N(0)$, we can transform the summation over k into an integral over the

energy:

$$N(E) = N(0) \int \frac{d\epsilon_k}{4\pi^2} \langle \delta(E - \sqrt{\epsilon_k^2 + \Delta_k^2}) \rangle_{E_F}, \tag{2.59}$$

where $< .. >_{E_F}$ is an average over the Fermi sphere. Using the property of the delta-Dirac function, $\delta(f(x)) = \sum_i \delta(x - x_i)/f'(x_i)$, where x_i are the roots of $f(x)$, the density of states becomes:

$$N(E) \sim \left\langle \frac{E\Theta(E^2 - \Delta_k^2)}{\sqrt{(E^2 - \Delta_k^2)}} \right\rangle_{E_F}. \tag{2.60}$$

An on-site s-wave order parameter is isotropic and does not have nodes, $\Delta_k = \Delta$. This is reflected in the fact that excitations in an s-wave superconductor are gapped. The density of states will exhibit a gap of size 2Δ around $E = 0$. In contrast, the extended s-wave and the d-wave order parameters have lines of nodes ($\pm k_x = \pm k_y$). The nodal quasiparticles are not gapped, the d-wave density of states has a V-shape. Figure 2.4 shows the density of states for both d-wave (left) and s-wave (right), obtained from Eq. (2.60). One can see that for low energies, only the nodal quasiparticles contribute, and the density of states is linear with energy.

The main differences between physical properties of s-wave (mainly conventional type) and d-wave (mainly high-T_c) superconductors arise from two disparate sets of properties. First because of the low temperature quasiparticle behavior; s-wave superconductors have gapped excitations while d-wave excitations are gapless. Secondly because of the phase dependence of the order parameter; s-wave superconductors have an isotropic order parameter, while d-wave superconductors have lines of nodes and regions in momentum space with both negative and positive amplitudes.

2.4 The Bogoliubov de Gennes Equations

The presence of inhomogeneities, in the form of disorder, impurities, surfaces or interfaces, does not allow the use of k-space methods. The absence of translational symmetry requires a real-space method, with a real-space Hamiltonian. A generalization of the BCS methods which considers spatial variations of the pairing potentials is needed in order to describe inhomogeneous systems. Two such methods have been developed. First we have Gorkov's method that uses the equation of motion for Green's functions [58] and secondly we have the self-consistent method developed by P.G. de Gennes [63]. Throughout this work we will use the second method, as it is well suited for numerical calculations on lattices.

Our starting point is the mean-field extended Hubbard Hamiltonian, Eq. (2.18), which is a tight binding Hamiltonian, written in the second quantization language. It

models interacting electrons on a lattice, and it incorporates superconducting correlations between electrons of opposite spins which reside either on the same site of the lattice or on nearest neighboring sites.

We are seeking to diagonalize the Hamiltonian by using a generalized Bogoliubov-Valatin canonical transformation:

$$c_{i\uparrow} = \sum_n (u_n^i \gamma_{n\uparrow} - v_n^{i*} \gamma_{n\downarrow}^\dagger), \tag{2.61}$$

$$c_{i\downarrow} = \sum_n (u_n^i \gamma_{n\downarrow} + v_n^{i*} \gamma_{n\uparrow}^\dagger), \tag{2.62}$$

where $\gamma_{n\uparrow}$ and $\gamma_{n\downarrow}$ are fermionic operators and u_n^i and v_n^i are complex numbers. Similar to the homogeneous case, the γ operators are quasiparticle excitations of the system. The anti-commutation relations of the electron operators will give normalization the orthogonalization conditions for u_n^i and v_n^i.

For example, from $\{c_{i\uparrow}, c_{i\downarrow}\} = 0$ we get:

$$\sum_n u_n^i v_n^{i*} - u_n^i v_n^{i*} = 0. \tag{2.63}$$

Similarly from $\{c_{i\uparrow}, c_{i\uparrow}^\dagger\} = 1$ we obtain:

$$\sum_n (|u_n^i|^2 + |v_n^i|^2) = 1. \tag{2.64}$$

Operators on different sites of the lattice will anti-commute, giving rise to the following conditions for u_n and v_n:

$$\sum_n (u_n^i v_n^{j*} - u_n^j v_n^{i*}) = 0 \tag{2.65}$$

$$\sum_n (u_n^i u_n^{j*} + v_n^j v_n^{i*}) = 0. \tag{2.66}$$

The diagonalized Hamiltonian will now take the form:

$$\mathcal{H} = E_0 + \sum_{n,\sigma} \epsilon_n \gamma_{n\sigma}^\dagger \gamma_{n\sigma}, \tag{2.67}$$

where E_0 is the ground state energy and ϵ_n is the energy of the excitation of the superconductor.

Following the procedure presented in Appendix B the Bogoliubov-de Gennes equations(BdG) are obtained:

$$\epsilon_n u_n^l = -\sum_\delta t_{ll+\delta} u_n^{l+\delta} - (\mu + \xi_l) u_n^l + \Delta_l v_n^l + \sum_\delta (\Delta_{ll+\delta}^{\downarrow\uparrow} - \Delta_{ll+\delta}^{\uparrow\downarrow}) v_n^{l+\delta} \tag{2.68}$$

$$\epsilon_n v_n^l = \sum_\delta t_{ll+\delta} v_n^{l+\delta} + (\mu + \xi_l) v_n^l + \Delta_l^* u_n^l + \sum_\delta (\Delta_{ll+\delta}^{\downarrow\uparrow *} - \Delta_{ll+\delta}^{\uparrow\downarrow *}) u_n^{l+\delta} \tag{2.69}$$

The previous equations can be written in a more compact way for all the lattice sites by using the matrix form of the BdG equations:

$$\begin{pmatrix} \mathcal{H}_0 & \Delta \\ \Delta^* & -\mathcal{H}_0 \end{pmatrix} \begin{pmatrix} U_n \\ V_n \end{pmatrix} = \epsilon_n \begin{pmatrix} U_n \\ V_n \end{pmatrix}, \tag{2.70}$$

where

$$\begin{pmatrix} U_n \\ V_n \end{pmatrix} = \begin{pmatrix} u_n^1 \\ u_n^2 \\ \vdots \\ u_n^N \\ v_n^1 \\ v_n^2 \\ \vdots \\ v_n^N \end{pmatrix} \tag{2.71}$$

and the matrix components are the $N \times N$ matrices

$$\mathcal{H}_0 = \begin{pmatrix} -\mu-\xi_1 & -t & 0 & \cdots & 0 & -t & 0 & 0 \\ -t & -\mu-\xi_2 & -t & 0 & \cdots & 0 & \ddots & 0 \\ 0 & -t & \ddots & \ddots & 0 & \cdots & 0 & -t \\ \vdots & 0 & \ddots & \ddots & \ddots & 0 & \cdots & 0 \\ 0 & \cdots & 0 & -t & -\mu-\xi_i & -t & 0 & \vdots \\ -t & 0 & \cdots & 0 & \ddots & \ddots & \ddots & 0 \\ 0 & \ddots & 0 & \cdots & 0 & -t & -\mu-\xi_{N-1} & -t \\ 0 & 0 & -t & 0 & \cdots & 0 & -t & -\mu-\xi_N \end{pmatrix} \tag{2.72}$$

and

$$\Delta = \begin{pmatrix} \Delta_1 & \Delta_{1\,2} & 0 & \cdots & 0 & \Delta_{1\,N_x+1} & 0 & 0 \\ \Delta_{2\,1} & \Delta_2 & \Delta_{2\,3} & 0 & \cdots & 0 & \ddots & 0 \\ 0 & \Delta_{3\,2} & \Delta_3 & \ddots & 0 & \cdots & 0 & \Delta_{N-Nx\,N} \\ \vdots & 0 & \ddots & \ddots & \ddots & 0 & \cdots & 0 \\ 0 & \cdots & 0 & \Delta_{i\,i-1} & \Delta_i & \Delta_{i\,i+1} & 0 & \vdots \\ \Delta_{N_x+1\,1} & 0 & \cdots & 0 & \ddots & \ddots & \ddots & 0 \\ 0 & \ddots & 0 & \cdots & 0 & \Delta_{N-1\,N-2} & \Delta_{N-1} & \Delta_{N-1\,N} \\ 0 & 0 & \Delta_{N\,N-N_x} & 0 & \cdots & 0 & \Delta_{N\,N-1} & \Delta_N \end{pmatrix} \tag{2.73}$$

The matrix (2.72) has on the diagonal the chemical potential μ and the impurity potentials ξ_i. The off-diagonal lines correspond to the nearest neighbors of each lattice site. Similarly in Eq. (2.73), on the diagonal we have the on-site component of the order parameter and on the off-diagonals we have the nearest neighbors components of the order parameter.

The BdG equations, in the matrix form presented here, can be viewed as an eigenvalue problem. The eigenvalues of the matrix formed by $\mathcal{H}_0$ and Δ will be the energies of the quasiparticle excitations of the system, ϵ_n, while the eigenvectors will be the coherence coefficients $\begin{pmatrix} U_n \\ V_n \end{pmatrix}$. Together, the eigenvalues ϵ_n and the eigenvectors $\begin{pmatrix} U_n \\ V_n \end{pmatrix}$ will fully describe the system. Any physical observable can be calculated in terms of the eigenvalues and eigenvectors of the BdG matrix, as they are averages of the electron operators which can be written in terms of quasiparticle operators.

One important simplification is due to the existence of a particular symmetry of the BdG equations. If we multiply with -1 both Eq. (2.68) and Eq. (2.69), take the complex conjugate of them and switch their order we obtain a new set of equations:

$$\begin{pmatrix} \mathcal{H}_0 & \Delta \\ \Delta^* & -\mathcal{H}_0 \end{pmatrix} \begin{pmatrix} -V_n^* \\ U_n^* \end{pmatrix} = (-\epsilon_n) \begin{pmatrix} -V_n^* \\ U_n \end{pmatrix}. \tag{2.74}$$

The symmetry will allow us to calculate only half of the energy spectrum, because we can interchange ϵ_n with $-\epsilon_n$ and $\begin{pmatrix} U_n \\ V_n \end{pmatrix}$ with $\begin{pmatrix} -V_n^* \\ U_n^* \end{pmatrix}$ for the other half of the spectrum.

In addition to the completness conditions Eq. (2.63)-(2.66), other relations for the coherence factors can be obtained from the BdG equations. If the result of the following operation $[(2.68 \text{ for } u_n^i)u_m^{i*} - (2.68 \text{ for } u_m^i)^* u_n^i] + [(2.69 \text{ for } v_n^i)v_m^{i*} - (2.69 \text{ for } v_m^i)^* v_n^i]$ is summed over all the lattice sites, we obtain:

$$(\epsilon_n - \epsilon_m) \sum_i (u_m^{i*} u_n^i + v_m^{i*} v_n^i) = 0. \tag{2.75}$$

The energies ϵ_n and ϵ_m are eigenvalues of the BdG matrix, if they are non-degenerate , the previous equation becomes the orthogonalization condition:

$$\sum_i (u_m^{i*} u_n^i + v_m^{i*} v_n^i) = \delta_{mn}. \tag{2.76}$$

A different condition can be obtained if we sum the result of $[(2.68 \text{ for } u_n^i)v_m^i - (2.69 \text{ for } v_n^i)u_m^i] - [(2.68 \text{ for } u_m^i)v_n^i - (2.69 \text{ for } v_m^i)u_n^i]$ over all lattice sites. The new orthogonalization condition is:

$$\sum_i (v_m^i u_n^i - u_m^i v_n^i) = 0. \tag{2.77}$$

For a superconductor at finite temperature, the quasiparticle operators γ being fermionic operators will obey the Fermi statistics:

$$\langle \gamma^{\dagger}_{n\alpha}\gamma_{m\beta}\rangle = \delta_{nm}\delta_{\alpha\beta}f_n, \tag{2.78}$$

$$\langle \gamma_{n\alpha}\gamma_{n\beta}\rangle = 0, \tag{2.79}$$

where $f_n = 1/(1+\exp(\epsilon_n/kT))$.

Once the eigenvalues and eigenvectors of the system are known we can calculate the self-consistent order parameters in terms of quasiparticle averages:

$$\begin{aligned}\Delta_i &= U_i\langle c_{i\downarrow}c_{i\uparrow}\rangle \\ &= U_i\langle\sum_{n\,n'}(u^i_n\gamma_{n\downarrow}+v^{i*}_n\gamma^{\dagger}_{n\uparrow})(u^i_n\gamma_{n\uparrow}-v^{i*}_n\gamma^{\dagger}_{n\downarrow})\rangle \\ &= -U_i\sum_n u^i_n v^{i*}_n(1-2f_n).\end{aligned} \tag{2.80}$$

The nearest-neighbor superconducting order parameter can be rewritten as:

$$\begin{aligned}\Delta_{ij} &= \Delta^{\downarrow\uparrow}_{ij} - \Delta^{\uparrow\downarrow}_{ij} \\ &= \Delta^{\downarrow\uparrow}_{ij} + \Delta^{\downarrow\uparrow}_{ji}\end{aligned} \tag{2.81}$$

Substituting Eq. (2.61) and Eq. (2.62) into Eq. (2.81) the order parameter becomes:

$$\begin{aligned}\Delta_{ij} &= \frac{V_{ij}}{2}(\langle c_{i\downarrow}c_{j\uparrow}\rangle + \langle c_{j\downarrow}c_{i\uparrow}\rangle) \\ &= -\frac{V_{ij}}{2}\sum_n(u^i_n v^{j*}_n + u^j_n v^{i*}_n)(1-2f_n)\end{aligned} \tag{2.82}$$

It is also possible to calculate the electron density for each site i, $\langle n_i\rangle = \sum_\sigma\langle c^{\dagger}_{i\sigma}c_{i\sigma}\rangle$:

$$\langle n_i\rangle = 2\sum_n[|u^i_n|^2 f_n + |v^i_n|^2(1-f_n)], \tag{2.83}$$

the factor of 2 comes from the summation over the electron spins. The average electron density for the system will be:

$$\langle n\rangle = \frac{2}{N}\sum_i\sum_n |u^i_n|^2 f_n + |v^i_n|^2(1-f_n), \tag{2.84}$$

Any solution of the BdG equation has to be obtained self-consistently by repeatedly finding the order parameter from the BdG matrix, which itself is to be formed from the calculated order parameters. Major simplifications are achieved if we reintroduce translational symmetry along various directions. This will allow the description of surfaces while solving effective one-dimensional inhomogeneous problems.

Chapter 3

Numerical Methods

In the presence of inhomogeneities, the absence of translational symmetry requires the theory to be a real-space one. The solutions of the BdG equations are usually self-consistent solutions, leading to the impossibility of finding an analytical solution. In this chapter we will present three methods of solving the BdG equations. First we present the direct diagonalization method which is suitable for finite size systems, then we consider the easier case of planar surfaces and in the end describe a powerful recursion method.

3.1 Direct diagonalization of finite size systems

The most general case, for which there are no translational symmetries is the most difficult to solve. We need to consider the whole system when solving the BdG equations. The BdG matrix containing Eq. (2.72) and Eq. (2.73) is a hermitian matrix but the hopping amplitudes and the order parameters depend on position. Depending on the boundary conditions and on the shape of the system, the location of the non-zero elements changes.

We choose to number the sites following the $\hat{x}$ direction. For a square lattice of size $N_x \times N_y$, the total size of the system is $N = N_x N_y$. The index of a site i in the lattice will be $i = i_x + i_y N_x$. For a square lattice (Figure 3.1) with the nearest neighbors of site i being at $\delta_i^1 = i-1$, $\delta_i^2 = i+1$, $\delta_i^3 = i-N_x$ and $\delta_i^4 = i+N_x$, where N_x is the dimension of the lattice in the $\hat{x}$ direction, the non-zero elements are on the off-diagonals, 1 and N_x elements away from the diagonal (see Eq. (2.72) and Eq. (2.73)). Open boundary conditions will require some of the sites to have less than four nearest neighbors. The sites on the corners will have two while the sites on the sides of the square will have three nearest neighbors.

Using the same notation we can also model a square lattice with 110-oriented open surfaces. This can be achieved if for even sites i the nearest neighbors are $\delta_i^1 = i-N_x-1$, $\delta_i^2 = i - N_x$, $\delta_i^3 = i + N_x - 1$ and $\delta_i^4 = i + N_x$ and for odd sites i' the nearest neighbors

are $\delta^1_{i'} = i' - N_x$, $\delta^2_{i'} = i' - N_x + 1$, $\delta^3_{i'} = i' + N_x + 1$ and $\delta^4_{i'} = i' + N_x$. If we add the boundary conditions we can construct a square with 110-oriented sides.

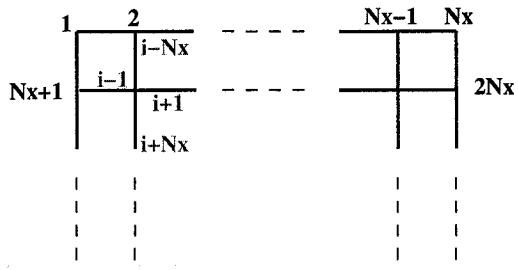

Figure 3.1: Numbering and nearest neighbors for a square lattice

Similar to any mean-field theory, the solutions of the BdG equations are to be found self-consistently. The self-consistent procedure is the following:

(1) choose an initial configuration of order parameters in the lattice

(2) diagonalize the BdG matrix (which is a matrix of size $2N_xN_y \times 2N_xN_y$), and find its eigenvalues and eigenvectors

(3) calculate the order parameters Δ_i using Eq. (2.80) and Δ_{ij} using Eq. (2.82)

(4) input the new order parameters in the BdG matrix

(5) repeat steps (2)-(4) until the relative difference between order parameters obtained for consecutive iterations is less than a desired convergence criterion:

$$\left| \frac{|\Delta_i^n| - |\Delta_i^{n-1}|}{|\Delta_i^n|} \right| < \epsilon \tag{3.1}$$

where n is the iteration number and ϵ is a small number; typically $\epsilon = 10^{-5}$. A separate convergence check is to be calculated also for the phase of the order parameters.

The numerical diagonalization is done using the LAPACK [72] expert driver ZHPEVX. The ZHPEVX subroutine diagonalizes complex hermitian matrices which are input in a packed format (only the upper or lower triangles are needed) and returns selected eigenvectors and eigenvalues. Because of a symmetric spectrum we find only half of the spectrum (negative eigenvalues).

Once we have the on-site, Δ_i, and the link , Δ_{ij}, order parameters we can calculate the s-wave, d-wave and extended s-wave components. For the homogeneous case $\Delta^d_k = 2\Delta_d(\cos k_x a - \cos k_y a)$ and $\Delta^{ext-s}_k = 2\Delta_s(\cos k_x a + \cos k_y a)$. Fourier transforming to

real-space we observe that for the d-wave case, the link order parameters have opposite sign on the $\hat{x}$ and $\hat{y}$ directions, $\Delta_{\pm x} = -\Delta_{\pm y}$. The link order parameters in the extended s-wave scenario are the same in all directions, $\Delta_{\pm x} = \Delta_{\pm y}$. Using these conditions we can define the d-wave order parameter for the real-space superconductor as:

$$\Delta_d = \frac{1}{4}(\Delta_x + \Delta_{-x} - \Delta_y - \Delta_{-y}) \tag{3.2}$$

and the extended s-wave order parameter as:

$$\Delta_s = \frac{1}{4}(\Delta_x + \Delta_{-x} + \Delta_y + \Delta_{-y}). \tag{3.3}$$

In the present formulation one can define surfaces and interfaces by modifying the hopping amplitudes t_{ij} and the pairing potentials U_i and V_{ij}. The behavior of the order parameter at corners and near impurities can be easily investigated with a finite-size 2D lattice. Rough surfaces can be also modeled if we randomly place strong impurities near the surface. The presence of strong repulsive impurities is equivalent to vanishing hopping amplitudes to the sites where the impurities are located. In Figure 3.2 a particular configuration of impurities defines a rough surface which has a mixture of (110) and (210) surfaces. The presence of (110) surfaces in d-wave superconductors has a drastic effect on the properties of the surface states. The so called "zero energy states" will appear for surfaces with such orientation.

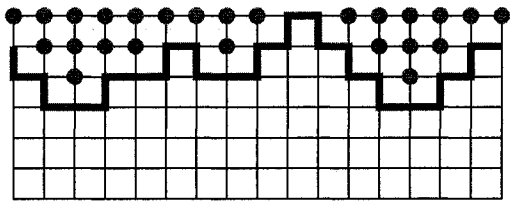

Figure 3.2: Rough surface defined by strong impurities

The direct diagonalization, although useful when we consider finite size samples and rough surfaces without any translational symmetry, is limited by the huge memory and CPU requirements. The diagonalization becomes very intense computationally because we are seeking half of the spectrum. The number of eigenvectors needed is equal to the size of the system ($N = N_x \times N_y$), half the size of the BdG matrix. Typical system sizes are on the order of 60×60 lattice sites. The information about the system is obtained by brute force, all at once. We will see later that the way around this problem is the use of a method which considers only the environment of a site, and which allows for independent calculations for each site.

3.2 Planar Surfaces

The presence of surfaces in the system recovers the translational symmetries in directions parallel to the surfaces. We can Fourier transform the Hamiltonian in the directions parallel to the surface and the inhomogeneous problem becomes a 1-dimensional one.

3.2.1 The (100) surface

The (100) surface is formed when one of the symmetry axes of the square lattice is perpendicular to the surface and the other is parallel. Translational symmetry is recovered for the direction parallel to the surface. As shown in Figure 3.3 the order parameters and the hopping amplitude will depend only on the distance from the surface. We will have now two types of link order parameters, $\Delta_i^{||}$ for nearest neighbors in the direction parallel to the surface and $\Delta_{i\,i\pm1}^{\perp}$ in the direction perpendicular to the surface; the same can be said about the hopping amplitudes $t_i^{||}$ and $t_{ij}^{\perp}$.

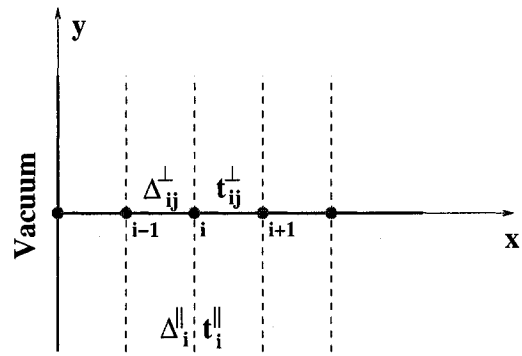

Figure 3.3: The (100) surface, effective 1D problem

Because of the recovered translational symmetry, we can Fourier transform operators in the parallel spatial direction to k-space:

$$c_{i_x i_y \sigma} = \frac{1}{N_y} \sum_{k_y} c_{i_x \sigma}(\pm k_y) e^{\mp i k_y r_y} \tag{3.4}$$

Plugging the transformation (3.4) into the mean-field Hamiltonian (2.18) we obtain:

$$\begin{aligned}
\mathcal{H}_{10} &= \sum_{k_y} \sum_{<ij>\sigma} -(1-\delta_{ij}) t_{ij}^{\perp} - \delta_{ij}[\mu + \xi_i + 2t_i^{||} cos(k_y a))] c_{i\sigma}^{\dagger}(k_y) c_{j\sigma}(k_y) \\
&+ \sum_{k_y} \sum_{i} [\Delta_i + 2\Delta_i^{||} cos(k_y a)] c_{i\uparrow}^{\dagger}(k_y) c_{i\downarrow}^{\dagger}(-k_y) + h.c. \\
&+ \sum_{k_y} \sum_{<ij>} [\Delta_{ij}^{\downarrow\uparrow\perp} c_{j\uparrow}^{\dagger}(k_y) c_{i\downarrow}^{\dagger}(-k_y) + \Delta_{ij}^{\uparrow\downarrow\perp} c_{j\downarrow}^{\dagger}(-k_y) c_{i\uparrow}^{\dagger}(k_y)] + h.c.,
\end{aligned} \tag{3.5}$$

where i and j are now in the direction perpendicular to the surface.

The mean-field order parameters are to be calculated self-consistently, by using the Fourier transform in the parallel direction:

$$\Delta_i = \frac{1}{N_y}\sum_{k_y} U_i < c_{i\downarrow}(-k_y)c_{i\uparrow}(k_y) >, \tag{3.6}$$

$$\Delta_i^{||} = \frac{1}{N_y}\sum_{k_y} V_i^{||} < c_{i\downarrow}(-k_y)c_{i\uparrow}(k_y) > cos(k_y a), \tag{3.7}$$

$$\Delta_{ij}^{\downarrow\uparrow\perp} = \frac{1}{N_y}\sum_{k_y} \frac{V_{ij}^{\perp}}{2} < c_{i\downarrow}(-k_y)c_{j\uparrow}(k_y) >, \tag{3.8}$$

$$\Delta_{ij}^{\uparrow\downarrow\perp} = \frac{1}{N_y}\sum_{k_y} \frac{V_{ij}^{\perp}}{2} < c_{i\uparrow}(k_y)c_{j\downarrow}(-k_y) >, \tag{3.9}$$

where Δ_i is the s-wave order parameter, $\Delta_i^{||}$ is the d-wave order parameter of a link in the direction parallel to the surface and $\Delta_{ij}^{\alpha\beta\perp}$ is the d-wave order parameter of a link in the direction perpendicular to the surface.

Using the procedure presented in Chapter 2 the Hamiltonian is diagonalized by the canonical Bogoliubov-Valatin transformation:

$$c_{i\uparrow}(k_y) = \sum_n [u_n^i(k_y)\gamma_{n\uparrow}(k_y) - v_n^{i*}(k_y)\gamma_{n\downarrow}^{\dagger}(-k_y)] \tag{3.10}$$

$$c_{i\downarrow}(-k_y) = \sum_n [u_n^i(k_y)\gamma_{n\downarrow}(-k_y) + v_n^{i*}(k_y)\gamma_{n\uparrow}^{\dagger}(k_y)]. \tag{3.11}$$

where $\gamma_{n\uparrow}(k_y)$ and $\gamma_{n\downarrow}(-k_y)$ are quasiparticle operators corresponding to the quantum number n in the direction perpendicular to the surface and momentum k_y in the direction parallel to the surface. These operators obey the fermionic anti-commutation rules and the Fermi statistics. The BdG equations can be rewritten in the following form:

$$\begin{pmatrix} H^0(k_y) & \Delta(k_y) \\ \Delta^*(k_y) & -H^0(k_y) \end{pmatrix} \begin{pmatrix} U_n(k_y) \\ V_n(k_y) \end{pmatrix} = \epsilon_n(k_y) \begin{pmatrix} U_n(k_y) \\ V_n(k_y) \end{pmatrix}, \; n = 1..N_x, \tag{3.12}$$

where the BdG matrix is composed of

$$\mathcal{H}^0(k_y) = \begin{pmatrix} -\mu_i & -t & 0 & \cdots & \cdots & 0 \\ -t & -\mu_i & -t & 0 & \cdots & 0 \\ 0 & -t & -\mu_i & -t & 0 & \vdots \\ \vdots & \vdots & \ddots & \ddots & \ddots & \vdots \end{pmatrix}, \tag{3.13}$$

with $\mu_i = \mu + \xi_i + 2t_i^{||} \cos k_y a$, and

$$\Delta(k_y) = \begin{pmatrix} \Delta_i' & \Delta_{ij}^{\perp} & 0 & \cdots & \cdots & 0 \\ \Delta_{ij}^{\perp} & \Delta_i' & \Delta_{ij}^{\perp} & 0 & \cdots & 0 \\ 0 & \Delta_{ij}^{\perp} & \Delta_i' & \Delta_{ij}^{\perp} & 0 & \vdots \\ \vdots & \vdots & \ddots & \ddots & \ddots & \vdots \end{pmatrix} \tag{3.14}$$

with $\Delta_i' = \Delta_i + 2\Delta_i^{||} \cos k_y a$. The eigenvectors $U(k_y)$ and $V(k_y)$ have in this case N_x elements:

$$U_n(k_y) = \begin{pmatrix} u_n^1(k_y) \\ u_n^2(k_y) \\ \vdots \\ u_n^{N_x}(k_y) \end{pmatrix} \text{ and } V_n(k_y) = \begin{pmatrix} v_n^1(k_y) \\ v_n^2(k_y) \\ \vdots \\ v_n^{N_x}(k_y) \end{pmatrix}. \tag{3.15}$$

The eigenvalue problem is decoupled for every momentum k_y. The BdG inhomogeneous problem is now a one-dimensional one, but which has to be solved N_y times.

The order parameters contained in the BdG matrix components (3.13) and (3.14), can now be written in terms of the coherence factors. They are obtained from Eqs. (3.6) - (3.9) with the use of the transformations (3.10) - (3.11):

$$\Delta_i = -\frac{1}{N_y} \sum_{k_y} \sum_{n} U_i u_n^i(k_y) v_n^{i*}(k_y)(1 - 2f_n(k_y)), \tag{3.16}$$

$$\Delta_i^{||} = -\frac{1}{N_y} \sum_{k_y} \sum_{n} V_i^{||} cos(k_y a)[u_n^i(k_y) v_n^{i*}(k_y)(1 - 2f_n(k_y))], \tag{3.17}$$

$$\Delta_{ij}^{\perp} = -\frac{1}{N_y} \sum_{k_y} \sum_{n} \frac{V_{ij}}{2}[u_n^i(k_y) v_n^{j*}(k_y) + u_n^j(k_y) v_n^{i*}(k_y))](1 - 2f_n(k_y)). \tag{3.18}$$

Once again the BdG equations have to be solved self-consistently. The algorithm followed for obtaining the self-consistent order parameters for a planar (100) surface is similar to the direct diagonalization case:

(1) propose initial values for Δ_i, $\Delta_{ij}^{\perp}$ and $\Delta_i^{||}$

(2) for every point k_y in the momentum space, diagonalize the BdG matrix (3.12) and obtain the eigenvalues $\epsilon_n(k_y)$ and eigenvalues $\begin{pmatrix} U_n(k_y) \\ V_n(k_y) \end{pmatrix}$

(3) recalculate the order parameters using Eqs. (3.16) - (3.18)

(4) input the new order parameters in the BdG matrix

(5) repeat steps (2) - (4) until the relative difference between the order parameters (Δ_i, $\Delta_i^{\parallel}$, $\Delta_{ij}^{\perp}$) obtained for consecutive iterations is less than a desired convergence criterion, typically 10^{-5}.

It is interesting to see for the non-interacting case ($U_i = V_{ij} = 0$), how the local density of states differs for sites located near the surface as opposed to sites that are in the bulk. Figure 3.4 shows the local density of states for five locations in the lattice. Close to the surface, the Van Hove singularities disappear from the local density of states. We can also observe an oscillatory behavior. This will show up in Friedel-like oscillations in the electron density. In the bulk the local density of states recovers the homogeneous form for a square lattice.

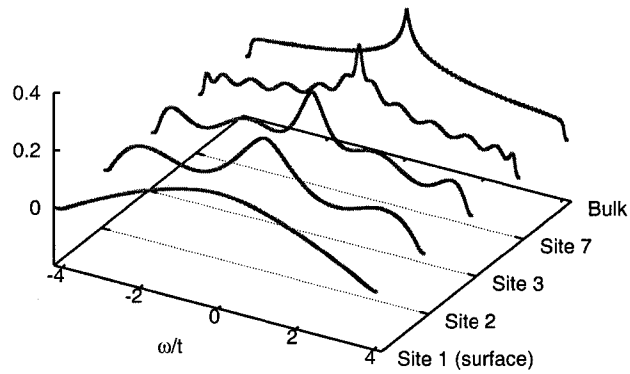

Figure 3.4: Local density of states in the non-interacting case, calculated at different distances from a 100 surface

The memory requirements of this method compared to the direct diagonalization are much smaller. We have to diagonalize only matrices of size $2N_x \times 2N_x$, but we have to diagonalize them N_y times. This is still less computationally intense than diagonalizing once a matrix of size $2N_xN_y \times 2N_xN_y$. Using this method we can model not only the (100) surface but also (100) interfaces between a normal metal and a superconductor, or between a s-wave superconductor and a d-wave superconductor. For these scenarios, as shown in the next chapter, we can look at the Andreev bound states, the proximity effect and the Josephson effect.

3.2.2 The (110) surface

The (110) oriented surface is of particular interest for d-wave superconductors. A distinct signature of d-wave superconductivity is the Zero Bias Conductance Peak (ZBCP) observed at (110) interfaces. The mixture of d-wave and s-wave order parameters near the surface leads to interesting effect observed directly in STM experiments.

As shown in Figure 3.5, the (110) surface can be obtained from a regular square lattice rotated by $\pi/4$. We need to consider cells which contain 2 type of sites. Type A has only two nearest neighbors at the surface while site B has four. The position of these sites can be written in terms of the lattice constant, $R^A_{xy} = xa\sqrt{2}\hat{x} + ya\sqrt{2}\hat{y}$ and $R^B_{xy} = (x + 1/2)a\sqrt{2}\hat{x} + (y + 1/2)a\sqrt{2}\hat{y}$, where x and y are the cell coordinates, i.e. integers.

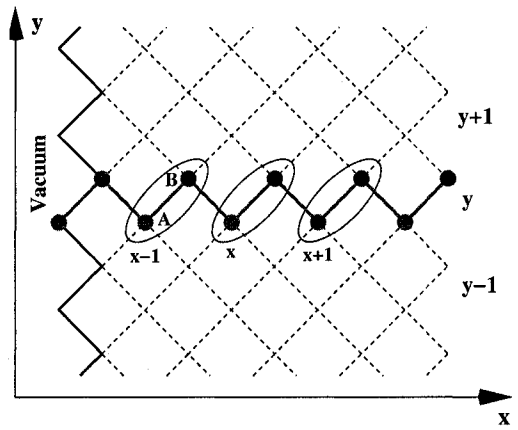

Figure 3.5: The 110 surface, effective 1D problem

If the boundary conditions in the $\hat{y}$ direction are periodic, the setup will describe a planar (110) surface. Translational symmetry is recovered along the surface. This will allow the use of the Fourier transform in the direction parallel to the surface. The transformation to k-space is presented in Appendix C. The Hamiltonian is written in terms of two types of electron operators, corresponding to sites A and B, c^A_{xy} and c^B_{xy}. The planar problem is one dimensional in the perpendicular direction. For each momentum vector in the $\hat{y}$ direction, we have to solve a one dimensional inhomogeneous problem with the use of the BdG equations. Using from Appendix C the transformed Hamiltonian (Eqs. (C.4), (C.6), (C.7) and (C.13) added together), we follow the procedure presented

in Appendix B and obtain the BdG equations for planar (110) surfaces:

$$\begin{pmatrix} \mathcal{H}_0^1(k) & \mathcal{H}_0^2(k) & \Delta^1(k) & \Delta^2(k) \\ \mathcal{H}_0^3(k) & \mathcal{H}_0^4(k) & \Delta^3(k) & \Delta^4(k) \\ \Delta_1^*(k) & \Delta_2^*(k) & -\mathcal{H}_0^1(k) & -\mathcal{H}_0^2(k) \\ \Delta_3^*(k) & \Delta_4^*(k) & -\mathcal{H}_0^3(k) & -\mathcal{H}_0^4(k) \end{pmatrix} \begin{pmatrix} U_n^A(k) \\ U_n^B(k) \\ V_n^A(k) \\ V_n^B(k) \end{pmatrix} = \epsilon_n(k) \begin{pmatrix} U_n^A(k) \\ U_n^B(k) \\ V_n^A(k) \\ V_n^B(k) \end{pmatrix} \tag{3.19}$$

where the component matrices are

$$\mathcal{H}_0^1(k) = \mathcal{H}_0^4(k) = \begin{pmatrix} -\mu - \xi_0 & 0 & \cdots & 0 \\ 0 & -\mu - \xi_1 & 0 & \vdots \\ \vdots & 0 & \ddots & 0 \\ 0 & \cdots & 0 & \ddots \end{pmatrix},$$

$$\mathcal{H}_0^2 = \begin{pmatrix} -2t\cos(ka\sqrt{2}/2) & 0 & \cdots & 0 \\ -2t\cos(ka\sqrt{2}/2) & -2t\cos(ka\sqrt{2}/2) & 0 & \vdots \\ 0 & -2t\cos(ka\sqrt{2}/2) & \ddots & 0 \\ \vdots & 0 & \ddots & \ddots \end{pmatrix},$$

$$\mathcal{H}_0^3 = \begin{pmatrix} -2t\cos(ka\sqrt{2}/2) & -2t\cos(ka\sqrt{2}/2) & 0 & \vdots \\ 0 & -2t\cos(ka\sqrt{2}/2) & -2t\cos(ka\sqrt{2}/2) & 0 \\ \vdots & 0 & \ddots & \ddots \\ 0 & \cdots & 0 & \ddots \end{pmatrix}$$

and the off-diagonal matrices that hold the order parameters are

$$\mathcal{H}_0^1(k) = \begin{pmatrix} \Delta_0^A & 0 & \cdots & 0 \\ 0 & \Delta_1^A & 0 & \vdots \\ \vdots & 0 & \ddots & 0 \\ 0 & \cdots & 0 & \ddots \end{pmatrix}, \mathcal{H}_0^4 = \begin{pmatrix} \Delta_0^B & 0 & \cdots & 0 \\ 0 & \Delta_1^B & 0 & \vdots \\ \vdots & 0 & \ddots & 0 \\ 0 & \cdots & 0 & \ddots \end{pmatrix},$$

$$\mathcal{H}_0^2 = \begin{pmatrix} \Delta_{xx} & 0 & \cdots & 0 \\ \Delta_{xx-1} & \Delta_{xx} & 0 & \vdots \\ 0 & \Delta_{xx-1} & \ddots & 0 \\ \vdots & 0 & \ddots & \ddots \end{pmatrix}, \mathcal{H}_0^3 = \begin{pmatrix} \Delta'_{xx} & \Delta_{x+1x} & 0 & \vdots \\ 0 & \Delta'_{xx} & \Delta_{x+1x} & 0 \\ \vdots & 0 & \ddots & \ddots \\ 0 & \cdots & 0 & \ddots \end{pmatrix},$$

where $\Delta_{xx} = e^{ika\sqrt{2}/2}(\Delta_{xx}^{-A\uparrow B\downarrow} + \Delta_{xx}^{-B\downarrow A\uparrow})$, $\Delta_{xx-1} = e^{-ika\sqrt{2}/2}\Delta_{xx-1}^{+B\uparrow A\downarrow} + e^{ika\sqrt{2}/2}\Delta_{xx-1}^{-B\downarrow A\uparrow}$, $\Delta'_{xx} = e^{-ika\sqrt{2}/2}(\Delta_{xx}^{+B\uparrow A\downarrow} + \Delta_{xx}^{+A\downarrow B\uparrow})$ and $\Delta_{x+1x} = e^{ika\sqrt{2}/2}\Delta_{xx+1}^{-A\uparrow B\downarrow} + e^{-ika\sqrt{2}/2}\Delta_{xx+1}^{+A\downarrow B\uparrow}$ (see Appendix C).

Following the procedure introduced for the (100) surface, we have to solve self-consistently the BdG equations for each momentum vector k:

(1) guess an initial configuration for the order parameters, alternating signs for nearest neighbor order parameters will insure a d-wave solution to the BdG equation

(2) for each k diagonalize the BdG matrix (3.19) to find its eigenvalues and its eigenvectors

(3) recalculate the order parameters (see Appendix C) using the previously found eigenvalues and eigenvectors

(4) input the order parameters in the BdG matrix

(5) repeat steps (2) - (4) until the relative difference between the order parameters calculated at consecutive iteration steps is less than a desired accuracy

Once the converged values for the nearest neighbor link order parameters are obtained, we are able to calculate the d-wave and extended s-wave components of the order parameter. Rotating by $\pi/4$ the square lattice, the order parameters can be written as:

$$\Delta_d = \frac{1}{4}(\Delta_{\hat{x}+\hat{y}} + \Delta_{-\hat{x}-\hat{y}} - \Delta_{-\hat{x}+\hat{y}} - \Delta_{\hat{x}-\hat{y}}) \tag{3.20}$$

$$\Delta_s = \frac{1}{4}(\Delta_{\hat{x}+\hat{y}} + \Delta_{-\hat{x}-\hat{y}} + \Delta_{-\hat{x}+\hat{y}} + \Delta_{\hat{x}-\hat{y}}) \tag{3.21}$$

For sites at the surface that do not have four nearest neighbors, for example site A at the surface which has two nearest neighbors, the order parameter takes in account only the existing nearest neighbors; $\Delta_d = 1/2(\Delta_{\hat{x}+\hat{y}} - \Delta_{\hat{x}-\hat{y}})$.

The different properties of site types A and B come about because of the different number of nearest neighbors at the surface. This can be seen in the local density of states, calculated for the non-interacting case. In Figure 3.6 and Figure 3.7 we plot the local density of states sites of type A and B, for different distances away from the surface for all submatrices Δ in (3.19) set to zero (non-interacting case). At the surface, the local density of states is very different for the two types, while for sites away from the surface, we recovers the local density of states for the homogeneous square lattice. This difference is observed also for the superconducting state. At half-filling, the appearance of the zero energy states is observed only for sites of type A. The planar (110) surface setup, allows us to calculate the order parameters and the LDOS at the surface, observe the formation of the zero energy states and of the zero bias conductance peak. We can also define interfaces between normal-metal and d-wave superconductors or s-wave and d-wave superconductors by setting the pairing potentials to different values throughout the lattice. This will allow us to calculate self-consistently the proximity effect.

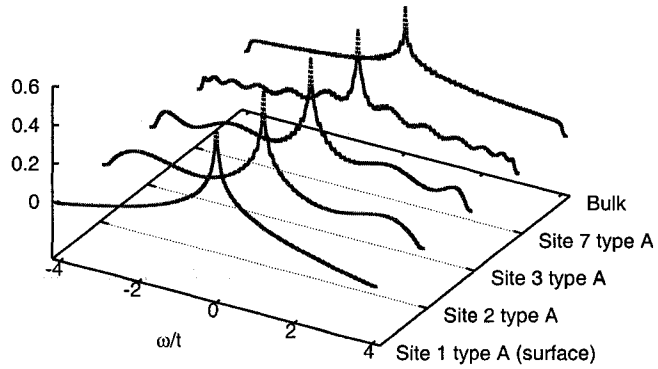

Figure 3.6: Local density of states in the non-interacting case for sites of type A, calculated at different distances from a (110) surface

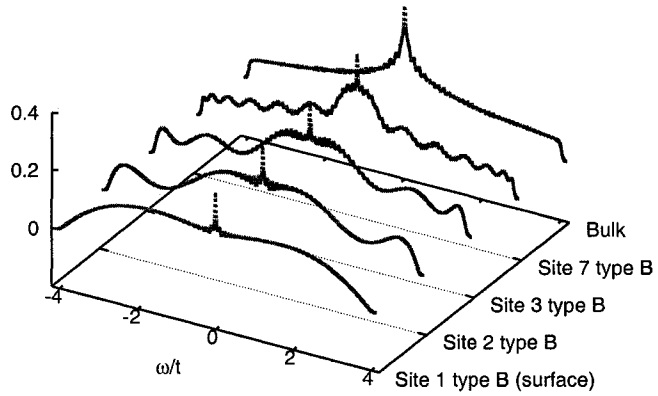

Figure 3.7: Local density of states in the non-interacting case for sites of type B, calculated at different distances from a (110) surface

3.2.3 C-axis surface

The c-axis geometry is of interest in the case of high-T_c superconductors, as they are highly anisotropic in the direction perpendicular to the CuO planes. It is widely accepted that superconductivity resides in the CuO, and that tunneling between planes

occurs. If we consider coherent tunneling of electrons between planes, this will show up as a hopping term in the Hamiltonian. A mean field 3D Hamiltonian describing coupling between planes will have the same form as the previously defined mean-field Hamiltonian in Eq. (2.18) but the nearest neighbor order parameters are:

$$\Delta_{ij} = \begin{cases} \Delta_{ij}^{\parallel}, & \text{if } i \text{ and } j \text{ are in the same } CuO \text{ plane} \\ 0, & \text{if } i \text{ and } j \text{ are in different } CuO \text{ planes} \end{cases} \tag{3.22}$$

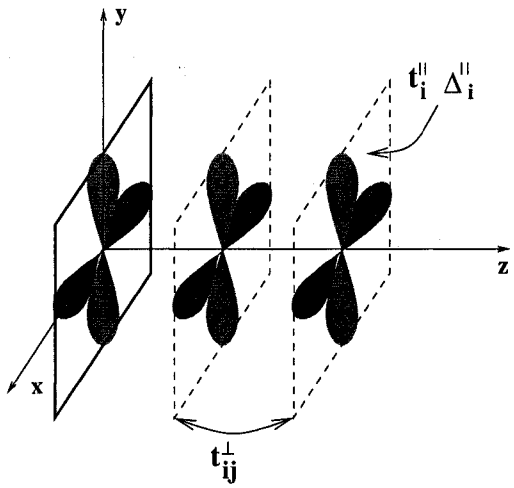

Figure 3.8: The c-axis surface, effective 1D problem

The c-axis planar surface allows us to Fourier transform along the $\hat{x}$ and $\hat{y}$ directions (see Figure 3.8). The magnitude of the d-wave order parameter will depend on the distance from the surface, but the symmetry is the same throughout the lattice. The Fourier transformed Hamiltonian is:

$$\begin{aligned} \mathcal{H} &= \frac{1}{N_x N_y} \sum_{k_x k_y} \sum_{<ij>\sigma} -t_{ij}^{\perp} c_{i\sigma}^{\dagger}(k_x, k_y) c_{j\sigma}(k_x, k_y) \\ &- \frac{1}{N_x N_y} \sum_{k_x k_y} \sum_{i\sigma} [\mu + \xi_i + 2t_i^{\parallel}(\cos k_x a + \cos k_y a)] c_{i\sigma}^{\dagger}(k_x, k_y) c_{i\sigma}(k_x, k_y) \\ &+ \frac{1}{N_x N_y} \sum_{k_x k_y} \sum_{i} \{\Delta_i + 2\Delta_i^{\parallel}[cos(k_x a) - cos(k_y a)]\} c_{i\uparrow}^{\dagger}(k_x, k_y) c_{i\downarrow}^{\dagger}(k_x, k_y) + h.c., \end{aligned}$$

where i and j are now in the $\hat{z}$ direction. We assume the d-wave symmetry in the CuO planes. This is achieved by considering the initial order parameters to have alternating sign in the $\hat{x}$ direction compared to the $\hat{y}$ direction. The self-consistency in the order

parameters is now given by the following equations:

$$\Delta_i = \frac{1}{N_x N_y} \sum_{k_x,k_y} U_i \langle c_{i\downarrow}(k_x,k_y) c_{i\uparrow}(k_x,k_y)\rangle, \tag{3.23}$$

$$\Delta_i^{||} = \frac{1}{N_x N_y} \sum_{k_x,k_y} V_i^{||} \langle c_{i\downarrow}(k_x,k_y) c_{i\uparrow}(k_x,k_y)\rangle [cos(k_x a) - cos(k_y a)], \tag{3.24}$$

where i is now taken to be the site index in the $\hat{z}$ direction. Δ_i is the on-site s-wave order parameter while $\Delta_i^{||}$ is the d-wave order parameter which has components only in the $\hat{x}$ and $\hat{y}$ directions.

Following the methodology introduced for the (100) surface, we introduce the Bogoliubov - Valatin canonical transformation (Eq. (2.61) and Eq. (2.62)) of the electron operators for each point (k_x, k_y) in the momentum space. This transformation will diagonalize the Hamiltonian and one obtains the BdG equations for each pair of momentum vectors k_x, k_y:

$$\begin{pmatrix} \mathcal{H}_0(k_x,k_y) & \Delta(k_x,k_y) \\ \Delta^*(k_x,k_y) & -\mathcal{H}_0(k_x,k_y) \end{pmatrix} \begin{pmatrix} U(k_x,k_y) \\ V(k_x,k_y) \end{pmatrix} = \epsilon(k_x,k_y) \begin{pmatrix} U(k_x,k_y) \\ V(k_x,k_y) \end{pmatrix}, \tag{3.25}$$

where

$$\mathcal{H}_0(k_x,k_y) = \begin{pmatrix} -\mu_1 & -t & 0 & \cdots & \cdots & 0 \\ -t & -\mu_2 & -t & 0 & \cdots & 0 \\ 0 & -t & -\mu_3 & -t & 0 & \vdots \\ \vdots & \vdots & \ddots & \ddots & \ddots & \vdots \end{pmatrix}, \tag{3.26}$$

with $\mu_i = \mu + \xi_i + 2t_i^{||}(\cos k_x a + \cos k_y a)$, and

$$\Delta(k_x,k_y) = \begin{pmatrix} \Delta_1' & 0 & \cdots & 0 \\ 0 & \Delta_2' & 0 & \vdots \\ \vdots & 0 & \Delta_3' & 0 \\ 0 & \cdots & 0 & \ddots \end{pmatrix} \tag{3.27}$$

with $\Delta_i' = \Delta_i + 2\Delta_i^{||}(\cos k_x a - \cos k_y a)$.

After we diagonalize the BdG matrix, and find the eigenvalues and eigenvectors we can calculate the self-consistent order parameters. At finite temperature, the quasiparticle averages are given by the Fermi distribution. This leads to the following form for the order parameters:

$$\Delta_i = -\frac{1}{N_x N_y} \sum_{k_x,k_y} \sum_n U_i u_n^i(k_x,k_y) v_n^{i*}(k_x,k_y)(1 - 2f_n(k_x,k_y)), \tag{3.28}$$

$$\Delta_i^{||} = -\frac{1}{N_x N_y} \sum_{k_x,k_y} \sum_n V_i^{||}(\cos k_x a - \cos k_y a) u_n^i(k_x,k_y) v_n^{i*}(k_x,k_y)(1 - 2f_n(k_x,k_y)), \tag{3.29}$$

The numerical procedure is identical to the one used for the other surface types. We guess an initial configuration for the order parameters (Δ_i and $\Delta_i^{||}$), with which we form the BdG matrix. The diagonalization of this matrix is performed for each pair of momentum vectors (k_x,k_y). With the use of the self-consistent relations (3.28) - (3.29) we calculate the new order parameters with which a new BdG matrix is constructed. This iteration is repeated until the relative difference of the order parameters calculated for two consecutive iterations is less than a desired accuracy. The converged solution consists in a configuration of order parameters, given the pairing potentials and the c-axis surface.

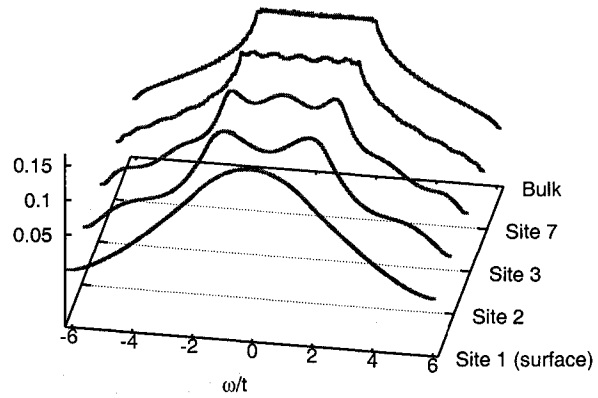

Figure 3.9: Local density of states in the non-interacting case, calculated at different distances from the c-axis surface

For the non-interacting case, $U_i = 0$ and $V_i = 0$, the surface will represent the 100 surface of a 3D cubic lattice. Only one numerical diagonalization is required for obtaining the eigenvalues and eigenvectors. Figure 3.9 shows the local density of states for sites at different distances from the surface. The oscillatory behavior is observed again, leading to Friedel like oscillations in the electron density. The known bulk density of states for cubic lattices is recovered for sites away from the surface.

3.3 The Recursive Method

Although easy to setup and implement, the direct diagonalization of the BdG matrix is very computationally intense. The memory requirements needed to store a complex matrix of size $2M \times 2M$, where M is the number of sites in the lattice, increases drastically with size of the system. The main difficulty in the diagonalization process is that

we need half of the eigenvalue spectrum and half of the eigenvector space. The number of operations for such a diagonalization is on the order of M^3. The time required to diagonalize the BdG matrix will increase dramatically as we increase the systems size.

An alternative powerful method, well suited for real-space calculations was developed by R. Haydock [73–77]. The recursion method leads to the computation of the Green's functions for each site in the lattice independently. The general definition of the Green function [78] is given by:

$$G_{ij}^{\alpha\beta}(t-t') = \begin{cases} -\frac{i}{\hbar}\langle c_{i\alpha}(t)c_{j\beta}^{\dagger}(t')\rangle, & t > t' \\ \frac{i}{\hbar}\langle c_{j\beta}^{\dagger}(t')c_{i\alpha}(t)\rangle, & t' > t \end{cases} \tag{3.30}$$

where i and j represent the spatial coordinates. From the equation of motion for the Green function it follows that in frequency space it satisfies the following equation:

$$(E - \mathcal{H})G_{ij}(E) = \delta_{ij} \tag{3.31}$$

there $\mathcal{H}$ is the Hamiltonian of the system. Written in a matrix form Eq. (3.31) becomes:

$$(EI - \mathcal{H})G(E) = I, \tag{3.32}$$

where I is the unit matrix. Eq. (3.32) shows that the matrix $G(E)$ can be viewed as the inverse of $(EI - \mathcal{H})$. Any components of the Green function can be calculated as:

$$G_{ij}(E) = \langle i|(EI - \mathcal{H})^{-1}|j\rangle \tag{3.33}$$

where $|i\rangle$ represents an electron located at site i.

The Green function matrix contains a huge amount of information. It contains not only information about all the locations in the system but also information about how the system will behave at any energy. Our goal is to extract only information about a specific location in the lattice. This is done within the recursion method by using the fact that any matrix can be transformed into a tridiagonal matrix. The procedure is known as the Lanczos method [79].

The Lanczos tridiagonalization method consists in finding an orthonormal basis $\{|u_n\rangle\}$ in which the matrix is tridiagonal. The recursive formula that gives this basis is the following:

$$\mathcal{H}|u_n\rangle = a_n|u_n\rangle + b_{n+1}|u_{n+1}\rangle + b_n|u_{n-1}\rangle, \tag{3.34}$$

where the coefficients a_n and b_n are the elements of the tridiagonal matrix $\mathcal{H}$:

$$\begin{pmatrix} a_0 & b_1 & 0 & 0 & 0 & 0 & 0 & \cdots \\ b_1 & a_1 & b_2 & 0 & 0 & 0 & 0 & \cdots \\ 0 & b_2 & \ddots & \ddots & 0 & 0 & 0 & \cdots \\ 0 & 0 & \ddots & \ddots & \ddots & 0 & 0 & \cdots \\ 0 & 0 & 0 & b_n & a_n & b_{n+1} & 0 & \cdots \\ \vdots & \vdots & \vdots & \vdots & \ddots & \ddots & \ddots & \ddots \end{pmatrix} \tag{3.35}$$

The coefficients a_n and b_n can be obtained from the orthogonality and orthonormality conditions of the basis vectors $\{|u_n\rangle\}$. Applying $\langle u_n|$ on the left of Eq. (3.34), a_n can be directly obtained:

$$a_n = \langle u_n|\mathcal{H}|u_n\rangle \tag{3.36}$$

Multiplying Eq. (3.34) on the left with $b^*_{n+1}\langle u_{n+1}|$, the following relation is true:

$$\begin{aligned} |b_{n+1}|^2 &= b^*_{n+1}\langle u_{n+1}|\mathcal{H}|u_n\rangle \\ &= \langle u_n|\mathcal{H}^\dagger\mathcal{H}|u_n\rangle - a_n\langle u_n|\mathcal{H}|u_n\rangle - b_n\langle u_{n-1}|\mathcal{H}|u_n\rangle \\ &= |\mathcal{H}|u_n\rangle|^2 - |a_n|^2 - |b_n|^2 \end{aligned} \tag{3.37}$$

The new vector in the iteration is now obtained if we consider the orthonormality of the basis:

$$|u_{n+1}\rangle = \frac{1}{b_{n+1}}(\mathcal{H}|u_n\rangle - a_n|u_n\rangle - b_n|u_{n-1}\rangle) \tag{3.38}$$

The starting vector in the iteration $|u_0\rangle$ will be the location where we want to calculate the Green function:

$$G_{00}(E) = \langle u_0| \begin{pmatrix} E-a_0 & b_1 & 0 & 0 & 0 & 0 & 0 & \cdots \\ b_1 & E-a_1 & b_2 & 0 & 0 & 0 & 0 & \cdots \\ 0 & b_2 & \ddots & \ddots & 0 & 0 & 0 & \cdots \\ 0 & 0 & \ddots & \ddots & \ddots & 0 & 0 & \cdots \\ 0 & 0 & 0 & b_n & E-a_n & b_{n+1} & 0 & \cdots \\ \vdots & \vdots & \vdots & \vdots & \ddots & \ddots & \ddots & \ddots \end{pmatrix}^{-1} |u_0\rangle. \tag{3.39}$$

Calculating the inverse of the tridiagonal matrix is very computationally intense, but because we want only the (0,0) component of the inverse, this can be done analytically. If D is the determinant of the full matrix and D_n is the determinant of the matrix with the first n lines and columns deleted, the element G_{00} can be calculated by using the cofactor formulation of the inverse:

$$G_{00}(E) = \frac{D_0}{D}. \tag{3.40}$$

We can write an iterative relation for calculating D_n:

$$\begin{aligned} D_n &= \begin{vmatrix} E-a_n & b_{n+1} & 0 & 0 & \cdots \\ b_{n+1} & E-a_{n+1} & b_{n+2} & 0 & \cdots \\ 0 & b_{n+2} & \ddots & \ddots & 0 \\ \vdots & \vdots & \vdots & \vdots & \vdots \end{vmatrix} \\ &= (E-a_n)\begin{vmatrix} E-a_{n+1} & b_{n+2} & 0 & \cdots \\ b_{n+2} & \ddots & \ddots & 0 \\ \vdots & \vdots & \vdots & \vdots \end{vmatrix} - b_{n+1}\begin{vmatrix} b_{n+1} & b_{n+2} & 0 & \cdots \\ 0 & E-a_{n+2} & b_{n+3} & 0 \\ \vdots & \vdots & \vdots & \vdots \end{vmatrix} \end{aligned}$$

$$= (E-a_n)\begin{vmatrix} E-a_{n+1} & b_{n+2} & 0 & \cdots \\ b_{n+2} & \ddots & \ddots & 0 \\ \vdots & \vdots & \vdots & \vdots \end{vmatrix} - b_{n+1}^2 \begin{vmatrix} E-a_{n+2} & b_{n+3} & 0 & \cdots \\ b_{n+3} & \ddots & \ddots & 0 \\ \vdots & \vdots & \vdots & \vdots \end{vmatrix},$$

which can be written in a more compact way,

$$D_n = (E-a_n)D_{n+1} - b_{n+1}^2 D_{n+2} \tag{3.41}$$

If we use Eq. (3.41) repeatedly in Eq. (3.40), the Green function can be written as a continued fraction:

$$G_{00}(E) = \cfrac{1}{E-a_0-b_1^2\cfrac{1}{E-a_1-b_2^2\cfrac{1}{E-a_2-b_3^2\cfrac{1}{\ddots}}}} \tag{3.42}$$

Once the Green function is known, physical properties can be calculated. For example, the local density of states can be extracted from the imaginary part of the Green function calculated at $E+i\delta$, where δ is a small number:

$$N_i(E) = -\frac{1}{\pi} ImG_{ii}(E+i\delta) \tag{3.43}$$

The eigenvalues of the system could be extracted from the zeros of the Green function, but this procedure might not be as stable as calculating physical properties, which are averages over all the eigenvalues. The local density of states is the sum of delta functions located at the eigenvalues of the system, but modulated by the eigenvectors relevant to that location. The recursion procedure extracts only information pertaining to a desired location.

The Lanczos iteration generates a chain of vectors $|u_n\rangle$, and can be seen as the diffusion of the initial vector $|u_0\rangle$ through the lattice. Hopping from one vector to the nearest neighbor is given by the recursion relation. In Figure 3.10 we show the evolution of the $|u_n\rangle$ vectors as a function of iteration, for a starting vector near the intersection of two surfaces. The presence of the surfaces is contained within the Hamiltonian, sites at the surface have only three nearest neighbors. As the iteration progresses, the Lanczos vectors reflect at the interface, giving rise to a specific chain of parameters a_n and b_n. In Figure 3.11, the starting vector is in the bulk of the system, and does not interact with any surfaces. The color distribution in the previous two graphs represents the amplitude of the wave function $|u_n(i)|^2$ at that site. The sequence of parameters a_n and b_n will be different from the previous case. It is also important to note that $|u_n\rangle$ at any iteration is orthogonal with all the previous vectors.

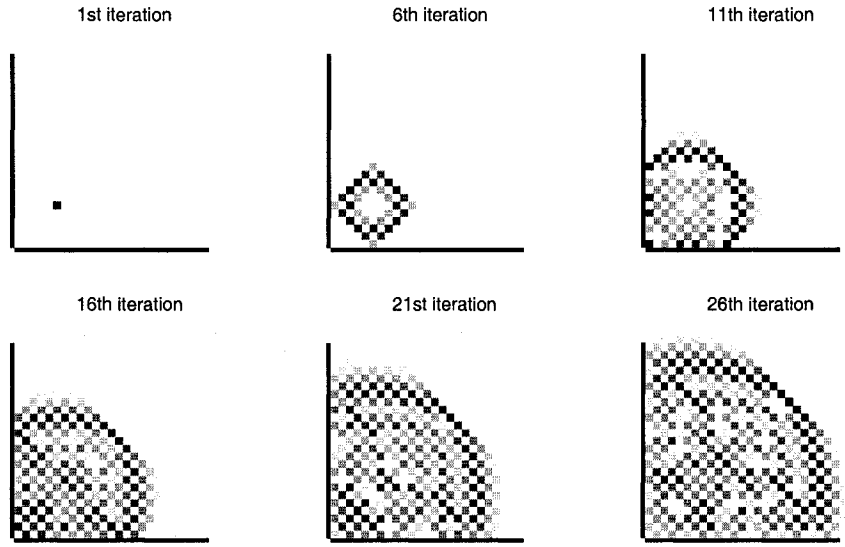

Figure 3.10: $|u_n(i)|^2$ as a function of iteration for a 2D lattice, near a corner

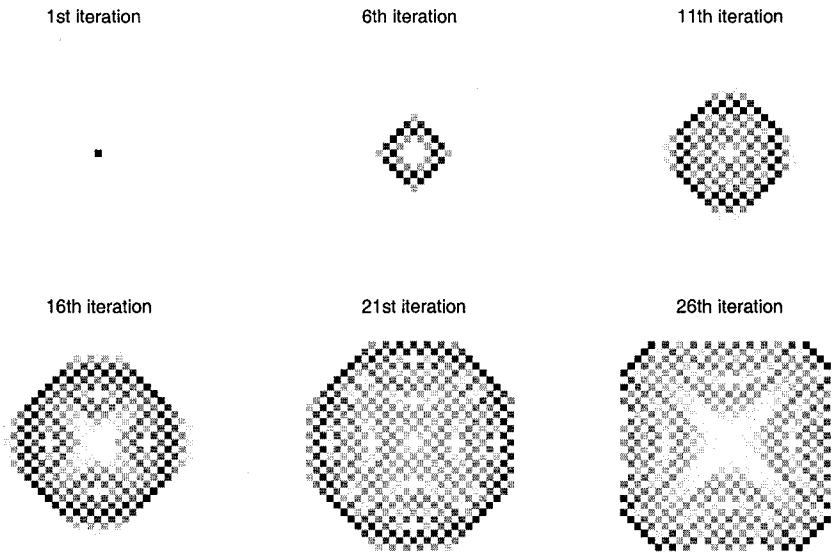

Figure 3.11: $|u_n(i)|^2$ as a function of iteration for a 2D lattice, in the bulk

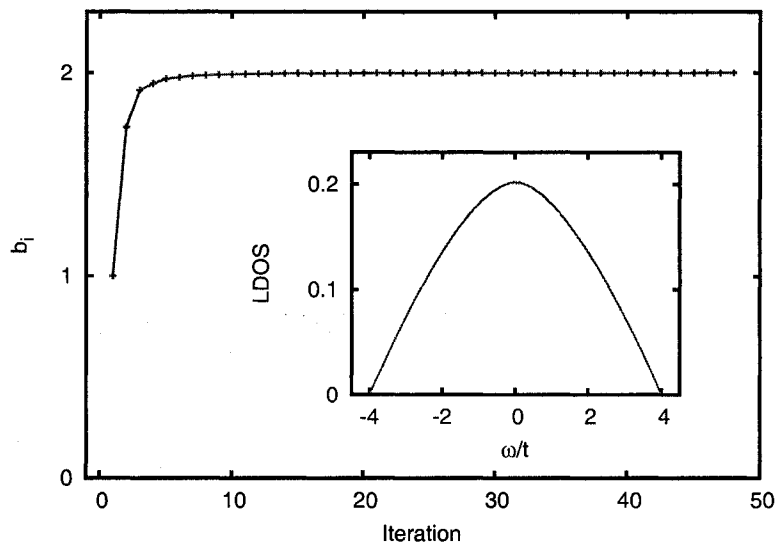

Figure 3.12: b_n coefficients for a site at the surface of a 2D lattice, and the corresponding LDOS

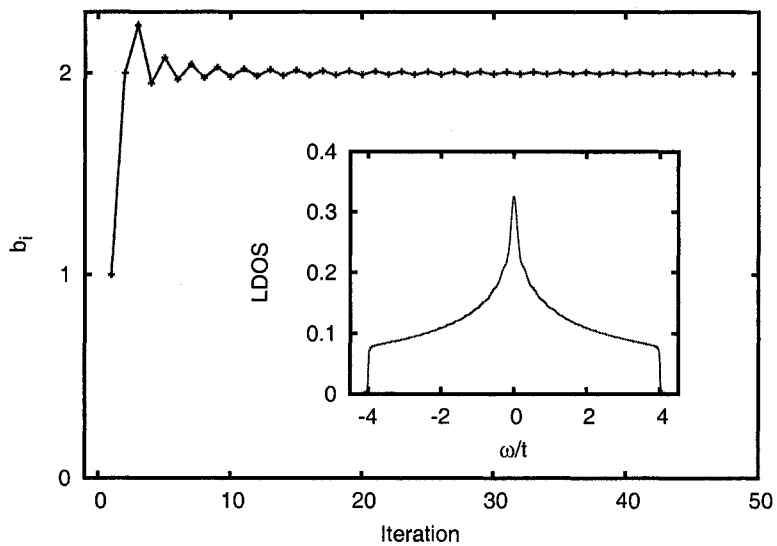

Figure 3.13: b_n coefficients for a site in the bulk of a 2D lattice, and the corresponding LDOS

The sequence of parameters b_n will determine the form of the Green function. Figure 3.12 shows the coefficients b_n as a function of iteration for a site located at the 100 surface of a 2D lattice, and the corresponding local density of states. For a semi-infinite system, the coefficients stabilize to a constant value. A different sequence b_n is obtained if the starting vector in the iteration is located in the bulk of a 2D lattice. We recover the homogeneous density of states for an infinite system. Again the coefficients are observed to stabilize after a number of iterations. This will allow us to model semi-infinite and infinite system only by looking at a few number of iterations at the beginning of the sequence and then extrapolating the rest of the sequence.

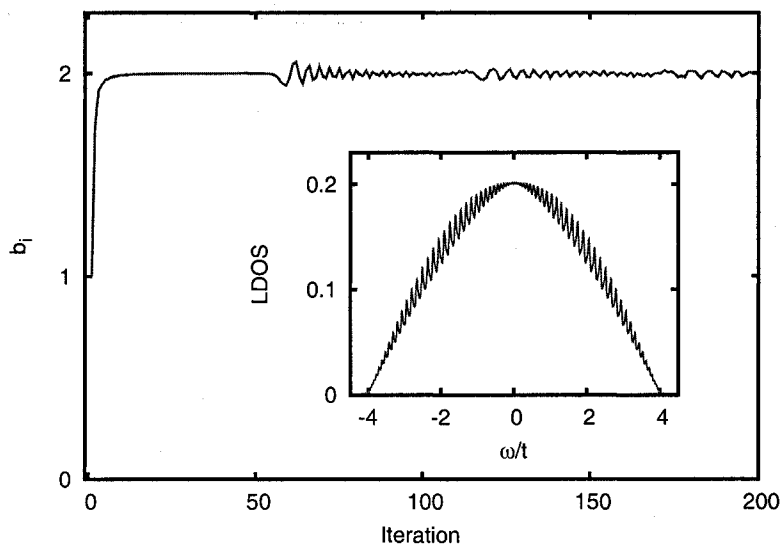

Figure 3.14: b_n coefficients for a site at the surface of a $40a \times 400a$ 2D lattice, and the corresponding LDOS

When calculating the Green function for a finite size system, one needs to consider a much larger number of iterations. The interaction with the surfaces will show up in the local density of states as interference effects from surfaces. This can be observed in Figure 3.14. Deviations from the infinite system appear for iterations larger than the size of the system in a particular direction. The peaks in the local density of states will appear for energies related to the quantized energies obtained for a 1D chain of size 40a.

The recursion method was extended to the description of the superconducting state [80–83]. In the presence of superconducting correlations, a new Green function has to be considered. In addition to the regular Green function, the anomalous Green function is introduced [58]:

$$F_{ij}(t-t') = \begin{cases} -\frac{i}{\hbar}\langle c_{i\uparrow}(t)c_{j\downarrow}(t')\rangle, & t > t' \\ \frac{i}{\hbar}\langle c_{j\downarrow}(t')c_{i\uparrow}(t)\rangle, & t' > t \end{cases} \tag{3.44}$$

At this point it is useful to consider the Nambu formalism [84]. In this formulation the wave function has two components, the electron with spin up and the hole part with spin down:

$$C_i = \begin{pmatrix} c_{i\uparrow} \\ c^\dagger_{i\downarrow} \end{pmatrix}, \qquad C^\dagger_j = (c^\dagger_{j\uparrow} \quad c_{j\downarrow}). \tag{3.45}$$

The Gorkov Green function will be a 2×2 matrix:

$$\begin{aligned} \hat{G}_{ij}(t-t') &= -\frac{i}{\hbar}\langle \mathcal{T} C_i C^\dagger_j \rangle \\ &= \begin{pmatrix} -\frac{i}{\hbar}\langle \mathcal{T} c_{i\uparrow} c^\dagger_{j\uparrow}\rangle & -\frac{i}{\hbar}\langle \mathcal{T} c_{i\uparrow} c_{j\downarrow}\rangle \\ -\frac{i}{\hbar}\langle \mathcal{T} c^\dagger_{i\downarrow} c^\dagger_{j\uparrow}\rangle & -\frac{i}{\hbar}\langle \mathcal{T} c^\dagger_{i\downarrow} c_{j\downarrow}\rangle \end{pmatrix} \end{aligned}$$

The energy dependent Green function will be:

$$\begin{aligned} \hat{G}_{ij}(E) &= \begin{pmatrix} G^{11}_{ij}(E) & G^{12}_{ij}(E) \\ G^{21}_{ij}(E) & G^{22}_{ij}(E) \end{pmatrix} \\ &= \begin{pmatrix} G_{ij}(E) & F_{ij}(E) \\ F^*_{ij}(E) & -G_{ji}(E) \end{pmatrix} \end{aligned} \tag{3.46}$$

The Hamiltonian of the system can also be written in the Nambu formalism as a 2×2 matrix [85]:

$$\widehat{\mathcal{H}} = \sum_i \begin{pmatrix} -\mu - \xi_i & \Delta_i \\ \Delta^*_i & \mu + \xi_i \end{pmatrix} |i><i| + \sum_{<i,j>} \begin{pmatrix} -t_{ij} & \Delta_{ij} \\ \Delta^*_{ij} & t_{ij} \end{pmatrix} |i><j| \tag{3.47}$$

where $\{|i\rangle\}$ represent the site basis. A relation similar to Eq. (3.32) can be written in the superconducting state. The resulting equations are known as the Gorkov's equations:

$$(E\hat{I} - \widehat{\mathcal{H}})\hat{G}(E) = \hat{I}, \tag{3.48}$$

where the Green function matrix is $N \times N$ matrix but each element is a block 2×2 matrix. The solution of Eq. (3.48) can be written formally:

$$\hat{G}(E) = (E\hat{I} - \widehat{\mathcal{H}})^{-1}. \tag{3.49}$$

The same tridiagonalization procedure can be applied, but in this case the matrix $E\hat{I} - \widehat{\mathcal{H}}$ will be block tridiagonal. The basis in which the Hamiltonian is tridiagonal, $\{|\hat{u}_n\rangle\}$, is itself a basis of 2×2 vectors, which in terms of the basis $|i\rangle$ is:

$$|\hat{u}_n\rangle = \begin{pmatrix} u^{11}_{ni} & u^{12}_{ni} \\ u^{21}_{ni} & u^{22}_{ni} \end{pmatrix} |i\rangle. \tag{3.50}$$

The Lanczos iterative procedure of finding the basis $\{|\hat{u}_n\rangle\}$ is the following:

$$\widehat{\mathcal{H}}|\hat{u}_n\rangle = |\hat{u}_{n+1}\rangle\hat{b}_{n+1} + |\hat{u}_n\rangle\hat{a}_n + |\hat{u}_{n-1}\rangle\hat{b}_n \tag{3.51}$$

where the coefficients $\hat{a}_n$ and $\hat{b}_n$ are 2×2 matrices, and they are the elements of the tridiagonal form of the Hamiltonian

$$\begin{pmatrix} \hat{a}_0 & \hat{b}_1 & 0 & 0 & 0 & 0 & 0 & \cdots \\ \hat{b}_1^\dagger & \hat{a}_1 & \hat{b}_2 & 0 & 0 & 0 & 0 & \cdots \\ 0 & \hat{b}_2^\dagger & \ddots & \ddots & 0 & 0 & 0 & \cdots \\ 0 & 0 & \ddots & \ddots & 0 & 0 & 0 & \cdots \\ 0 & 0 & 0 & \hat{b}_n^\dagger & \hat{a}_n & \hat{b}_{n+1} & 0 & \cdots \\ \vdots & \vdots & \vdots & \vdots & \ddots & \ddots & \ddots & \ddots \end{pmatrix}. \tag{3.52}$$

At any iteration step, $\hat{a}_n$ can be found directly by applying $\langle \hat{u}_n|$ to the left of Eq. (3.51) and using the orthonormality between the vectors in the basis ($\langle \hat{u}_n|\hat{u}_m\rangle = \delta_{mn}$):

$$\hat{a}_n = \langle \hat{u}_n|\widehat{\mathcal{H}}|\hat{u}_n\rangle. \tag{3.53}$$

The coefficients $\hat{b}_{n+1}$ are found by applying $\hat{b}_{n+1}^\dagger\langle \hat{u}_{n+1}|$ to the left of Eq. (3.51):

$$\begin{aligned} \hat{b}_{n+1}^\dagger\hat{b}_{n+1} &= \hat{b}_{n+1}^\dagger\langle \hat{u}_{n+1}|\mathcal{H}|\hat{u}_n\rangle \\ &= \langle \hat{u}_n|\widehat{\mathcal{H}}^\dagger\widehat{\mathcal{H}}|\hat{u}_n\rangle - \hat{a}_n^\dagger\langle \hat{u}_n|\widehat{\mathcal{H}}|\hat{u}_n\rangle - \hat{b}_n^\dagger\langle \hat{u}_{n-1}|\widehat{\mathcal{H}}|\hat{u}_n\rangle \\ &= \langle \hat{u}_n|\widehat{\mathcal{H}}^\dagger\widehat{\mathcal{H}}\|\hat{u}_n\rangle - \hat{a}_n^\dagger\hat{a}_n - \hat{b}_n^\dagger\hat{b}_n. \end{aligned} \tag{3.54}$$

As shown by Eq. (3.54), only the absolute value squared of $\hat{b}_n$ has a definite value. The sign of $\hat{b}_n$ is not well defined, it can be chosen so that $\hat{b}_n^{11} = -\hat{b}_n^{22}$. Because the initial vector corresponding to a site $|i\rangle$ is

$$|\hat{u}_0\rangle = \begin{pmatrix} 1 & 0 \\ 0 & 1 \end{pmatrix}|i\rangle, \tag{3.55}$$

the coefficient $\hat{b}_n$ will remain diagonal. Once the coefficients of the Lanczos iteration are calculated, we can write down the local Green function at $|\hat{u}_o\rangle$:

$$\hat{G}_{00}(E) = \langle \hat{u}_0|(E\hat{I} - \widehat{\mathcal{H}})^{-1}_{TD}|\hat{u}_0\rangle \tag{3.56}$$

where the subscript TD refers to the tridiagonal form. The local Green function can now be written in a continued fraction form:

$$\hat{G}_{00}(E) = (E - \hat{a}_0 - \hat{b}_1^\dagger(E - \hat{a}_1 - \hat{b}_2^\dagger(E - \hat{a}_3 - \hat{b}_3^\dagger(\cdots)\hat{b}_3)^{-1}\hat{b}_2)^{-1}\hat{b}_1)^{-1} \tag{3.57}$$

As an example Figure 3.15 shows the real and imaginary parts of the regular Green function $G_{ii}(E+i\delta)$ for a site 3 lattice spacings away from a surface. Figure 3.16 shows the real and imaginary parts of the anomalous Green function for the same location. The

size of the whole system considered in these plots is $200a \times 200a$ and the location where we seek the Green functions is $(i_x = 3, i_y = 100)$.

The Green function in the superconducting state contains not only information about the local density of states, but also information about the order parameter. Until now, we were able to calculate only diagonal elements of the Green function, namely $\hat{G}_{00}(E)$. Off-diagonal elements are needed when the nearest neighbor order parameter is desired. These elements can be calculated by doing four Lanczos iterations. If we define the following vectors:

$$
\begin{aligned}
|+r\rangle &= |i\rangle + |j\rangle, \\
|-r\rangle &= |i\rangle - |j\rangle, \\
|+i\rangle &= |i\rangle + i|j\rangle, \\
|-i\rangle &= |i\rangle - i|j\rangle,
\end{aligned}
$$

the real and imaginary parts of the off-diagonal Green function $G_{ij}(E)$ will be

$$\mathrm{Re}G_{ij}(E) = \frac{\langle +r|G(E)|+r\rangle - \langle -r|G(E)|-r\rangle}{2}, \tag{3.58}$$

$$\mathrm{Im}G_{ij}(E) = \frac{\langle +i|G(E)|+i\rangle - \langle -i|G(E)|-i\rangle}{2}. \tag{3.59}$$

The local density of states and the on-site s-wave order parameters will be calculated from the diagonal components of the Green function:

$$N_i(E) = -\frac{1}{\pi}\mathrm{Im}G_{ii}^{11}(E + i\delta), \tag{3.60}$$

$$\Delta_i = -\frac{U_i}{\beta}\sum_n e^{i\omega_n\delta}G_{ii}^{12}(i\omega_n), \tag{3.61}$$

while the nearest neighbor order parameters are calculated from the off-diagonal Green function:

$$\Delta_{ij} = -\frac{V_{ij}}{\beta}\sum_n e^{i\omega_n\delta}G_{ij}^{12}(i\omega_n). \tag{3.62}$$

where $\omega_n = \pi(2n+1)/\beta$ are the Matsubara frequencies. Because the correct order parameter configuration throughout the lattice is usually not known, one has to solve the problem self-consistently. If we input in the Hamiltonian an initial configuration of order parameters, we can start a recursion chain for each site and calculate the new order parameters. With the new order parameters one can form the new Hamiltonian and start new recursion chains. This loop continues until the order parameters are converged, the relative difference of order parameters between two steps is less than a desired accuracy.

The recursion method has several important benefits. First, because the Hamiltonian is a sparse matrix, we only need to store the non-zero elements. The sparse format will

also decrease substantially time required to perform matrix-vector products like $H|u_n\rangle$. Secondly, because each Lanczos recursion is independent, the process is trivially parallelizable. We can start in parallel a Lanczos iteration for each site. At the end we gather the results in the Hamiltonian and new parallel iterations are spawned. In principle only three vectors are stored at any time ($|u_{n+1}\rangle$, $|u_n\rangle$ and $|u_{n-1}\rangle$), reducing drastically the memory requirements of the numerical computations. The numerics are done using the PETSc [86] package which can be easily incorporated into a C++ code. With the use of PETSc it is straightforward to setup sparse matrices on multiple processors to compute matrix-vector multiplications in parallel through the use of MPI.

One of the drawbacks of the recursion method is that it is somewhat unstable. In exact arithmetics, the tridiagonalization procedure is exact, meaning that all the vectors $|u_n\rangle$ are orthogonal to each other. When calculations are done on a computer, due to roundoff errors, after a number of iterations basis vectors start to lose orthogonality. This instability can be resolved either with full re-orthogonalization of all vectors in the basis [87], selective orthogonalization [88] or partial orthogonalization [89].

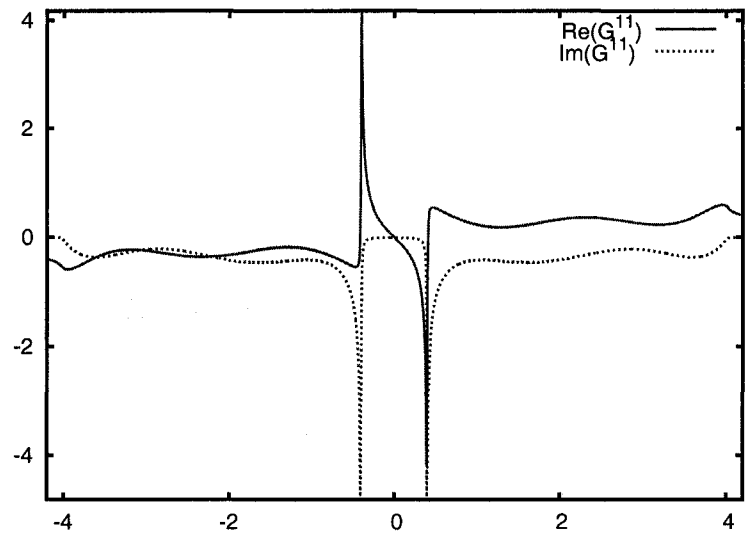

Figure 3.15: Real and imaginary parts of $G_{ii}^{11}(E + i\delta)$, here $\delta = 0.005$ and $\Delta = -0.4$

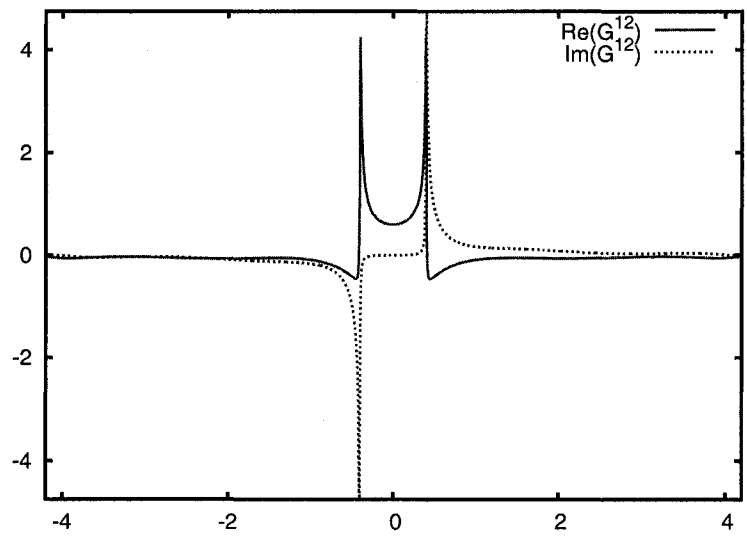

Figure 3.16: Real and imaginary parts of $G_{ii}^{12}(E + i\delta)$, here $\delta = 0.005$ and $\Delta = -0.4$

Chapter 4

Applications

4.1 Superconductivity near surfaces and corners

The characterization of superconductivity near surfaces and corners is considered by using the numerical methods presented in the previous chapter. Surface states can have a significant influence on measurements probing the surface in a direct manner. We first consider planar surfaces in the (100) and (110) orientations, and then a two-dimensional finite system is used for calculating the behavior of the order parameter near corners.

4.1.1 Planar (100) and (110) surfaces

Superconductivity near the (100) surface

In the (100) geometry translational symmetry is broken in the direction perpendicular to the surface. In Chapter 3.2.1 we presented a way of retaining the inhomogeneous problem perpendicular to the surface, by Fourier transforming the electron operators only in the direction parallel to the surface. This will reduce the initial problem to a one dimensional inhomogeneous one, for each momentum vector $k^{||}$. Huge benefits are seen in numerical calculations because we are able to describe large enough systems and obtain a very good energy resolution for the local density of states (LDOS).

Superconductivity near the (100) surface in considered for both s-wave and d-wave symmetries of the order parameter. Boundary conditions are set by assuming that at the interface with vacuum, electrons cannot leave the system and thus the corresponding hopping term is set to zero. Self-consistent calculations involve numerical diagonalizations for the effective one-dimensional problem, but their number is equal to the momentum states considered in the parallel direction.

For an s-wave superconductor at the (100) surface, the order parameter is observed to oscillate near the surface Figure 4.1. The oscillations remind one of Friedel oscillations observed when the electron wave function is perturbed near an impurity [90]. In

a normal metal the impurity is screened and the long-range oscillations in the screening charge arise from the sharp Fermi surface, because it is not possible to construct a smooth function (the electron density) out of a restricted set of wave vectors $k > k_F$. It was shown that around a non-magnetic impurity in a conventional superconductor oscillations in the order parameter and electron density are present [91]. The long-range behavior of these oscillations has the form $x^{-3}cos(2k_Fx)exp(-k_Fx\Delta/E_F)$. When the coherence length is large, the x^{-3} behavior is dominant, while if the coherence length is small the long-range behavior is dominated by the exponential decay. The superconducting coherence length can be seen here as a "healing" distance, the distance within which the order parameter recovers its bulk value. The coherence length is observed to increase with decreasing pairing potential, and also with the decrease of the chemical potential. The electron density also oscillated in the same manner near the surface Figure 4.2. Low chemical potential values will provide larger coherence lengths.

A superconducting gap develops in the LDOS for all locations in the superconductor. Figure 4.3 shows the LDOS for sites situated at various distances from the surface, for $U = -3t$ and $\mu = 0$. Oscillations in the LDOS are observed as we move away from the surface, hinting to the Friedel-like oscillations in the electron density. Figure 4.4 shows the LDOS for $U = -3t$ and $\mu = -t$. Similar behavior is obtained, the superconducting gap is super-imposed on the normal state LDOS. The coherence peaks at $E = \pm\Delta$ are seen throughout the system. In the bulk, the LDOS is also developing the Van Hove singularity near the band edge, specific to a 2D nearest-neighbor tight binding system.

For d-wave superconductivity near the (100) surface, the same methodology is applied. The link order parameter Δ_{ij} in the direction parallel to the surface will now behave like an on-site order parameter, but multiplied with $\cos k^{||}a$, while the order parameter in the direction perpendicular to the surface remains a nearest-neighbor type order parameter.

Following the procedure presented in the previous chapter, we perform self-consistent calculations of the order parameter near a (100) surface for various values of the pairing potential V and of the chemical potential μ. The results are summarized in Figure 4.5. We plot both the d-wave and the extended s-wave components of the order parameter. Again, oscillations are observed, both in the order parameter profile and in the electron density. The d-wave order parameter is observed to be suppressed at the surface, thus inducing an extended s-wave component only near the surface. The rapid oscillations of the order parameter show that quasi-classical methods applied to this problem will fail to give a correct answer.

In Figure 4.6 and Figure 4.7 we plot the LDOS for different locations near the surface for two values of the chemical potential, $\mu = -t$ and $\mu = 0$. The V-shape of the LDOS near the Fermi surface is observed only for sites far away from the surface, situated in the bulk. Near the surface the shape of the LDOS oscillates, and the number of peaks is directly related to the distance from the surface. The site located directly at the surface $i = 1$ does not show any oscillation, and the coherence peaks located at 2Δ disappear. It

is interesting to observe that for the second site located at $i = 2$ the LDOS has a U shape and does not resemble a d-wave LDOS. Away from half-filling ($\mu = 0$), we observe that the LDOS becomes asymmetric, showing the breakdown of the particle-hole symmetry. States with the lowest LDOS are observed at the Fermi surface, thus in the (100) surface no zero bias conductance peak is observed.

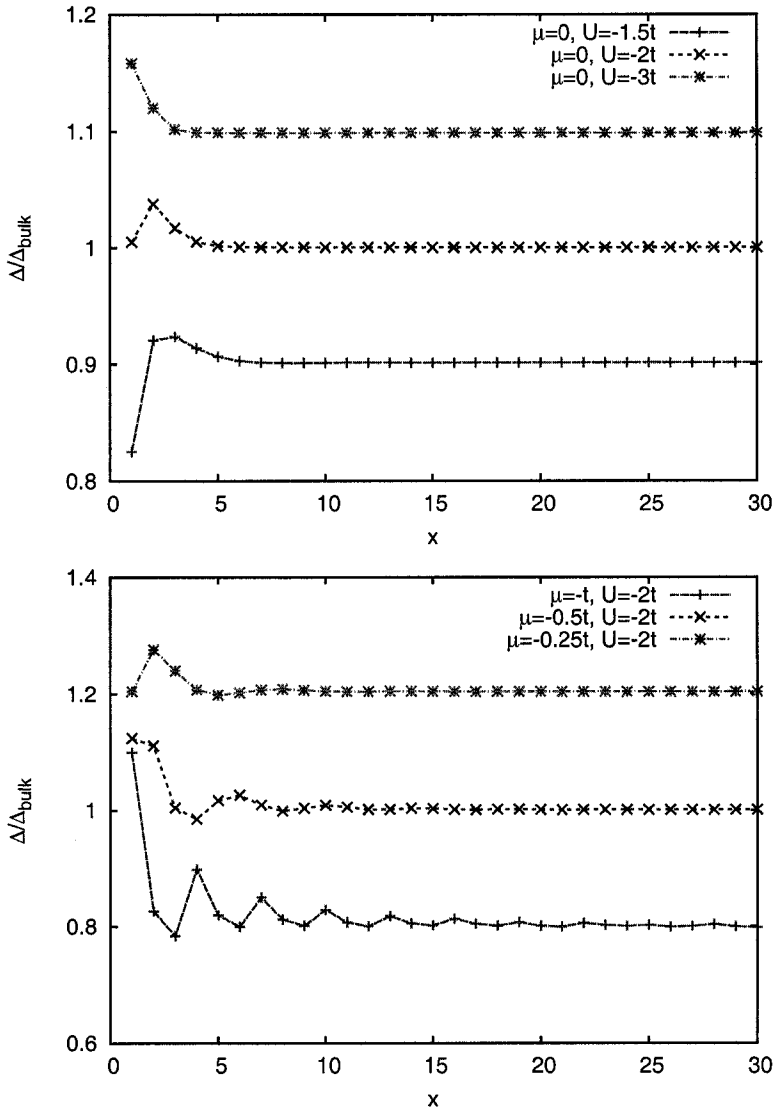

Figure 4.1: On-site s-wave order parameter near the (100) surface; the lines are shifted for clarity

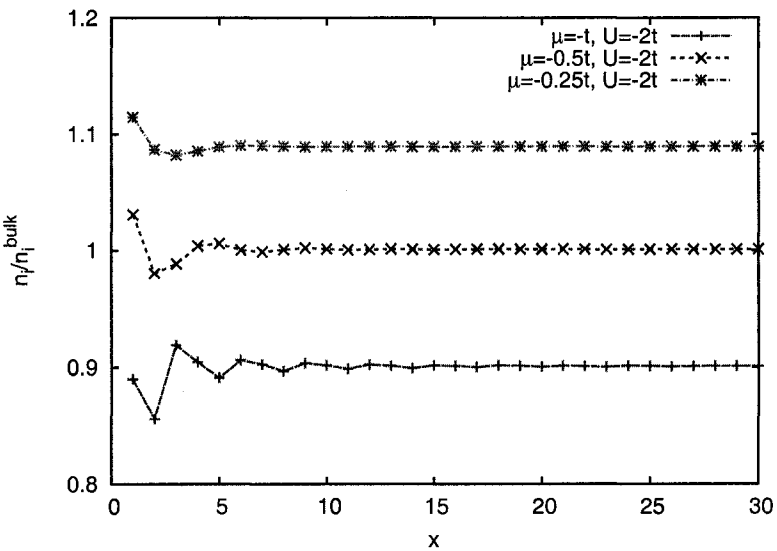

Figure 4.2: Electron density near the (100) surface for s-wave superconductor; the lines are shifted for clarity

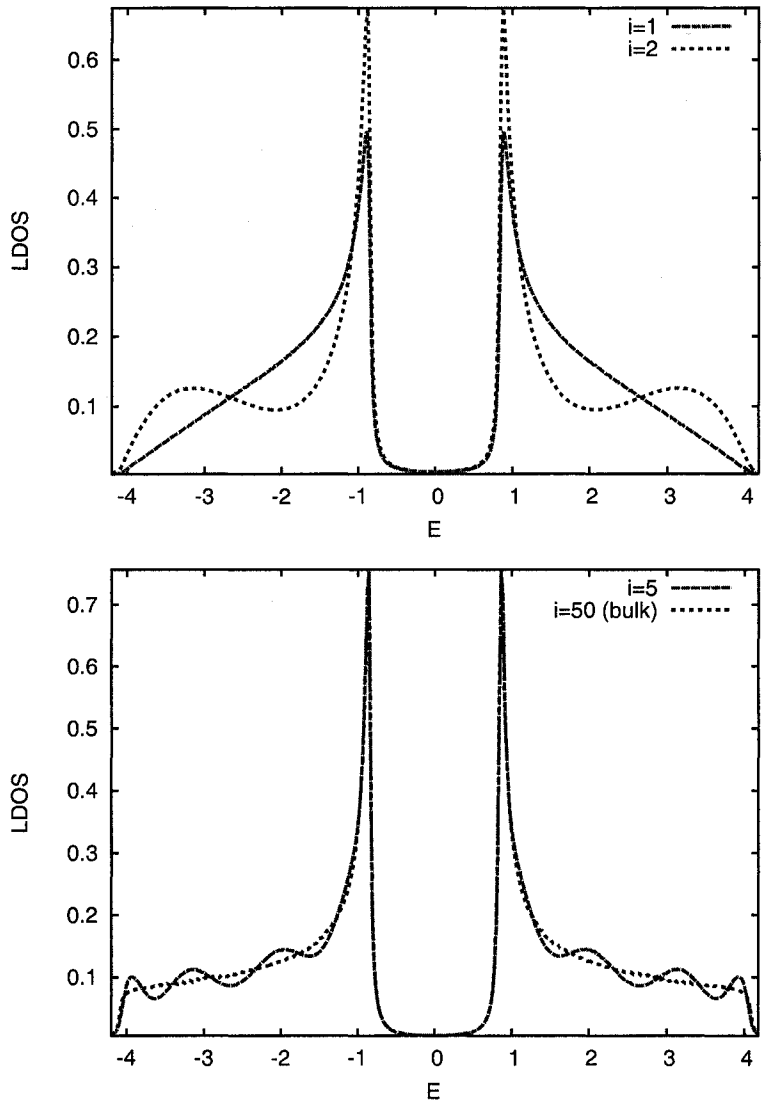

Figure 4.3: LDOS at various distances from the (100) surface; $U = -3t$, $\mu = 0$

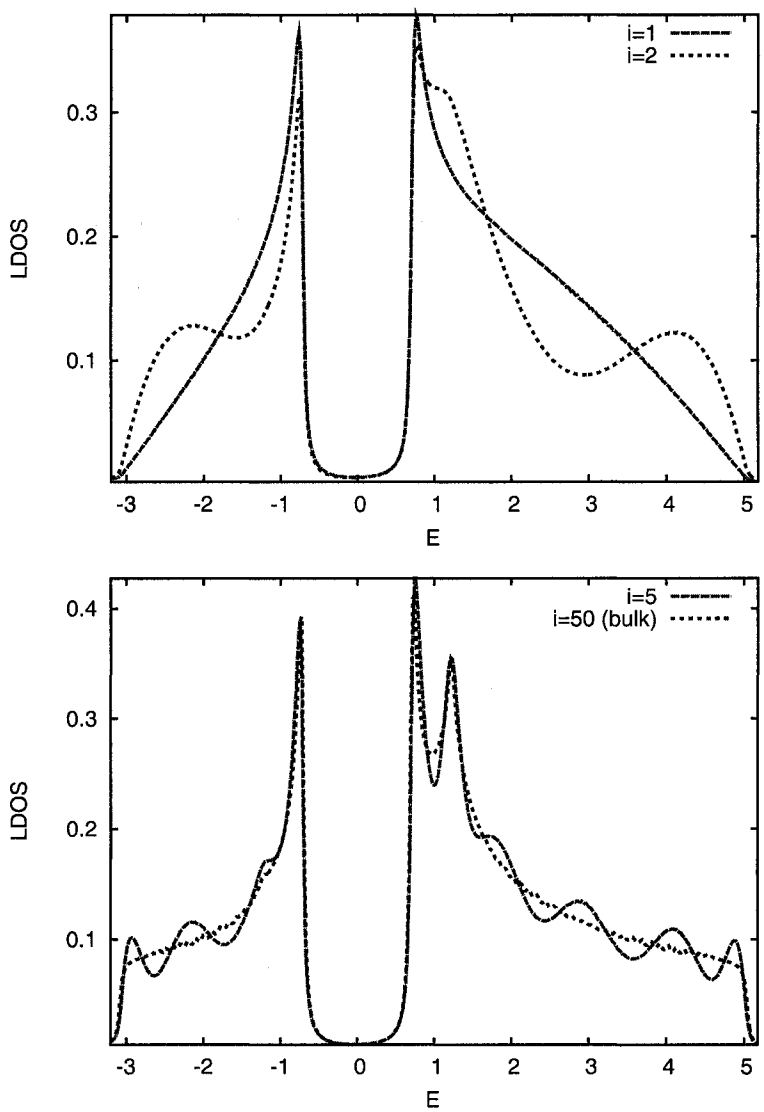

Figure 4.4: LDOS at various distances from the (100) surface; $U = -3t$, $V = 0$, $\mu = -t$

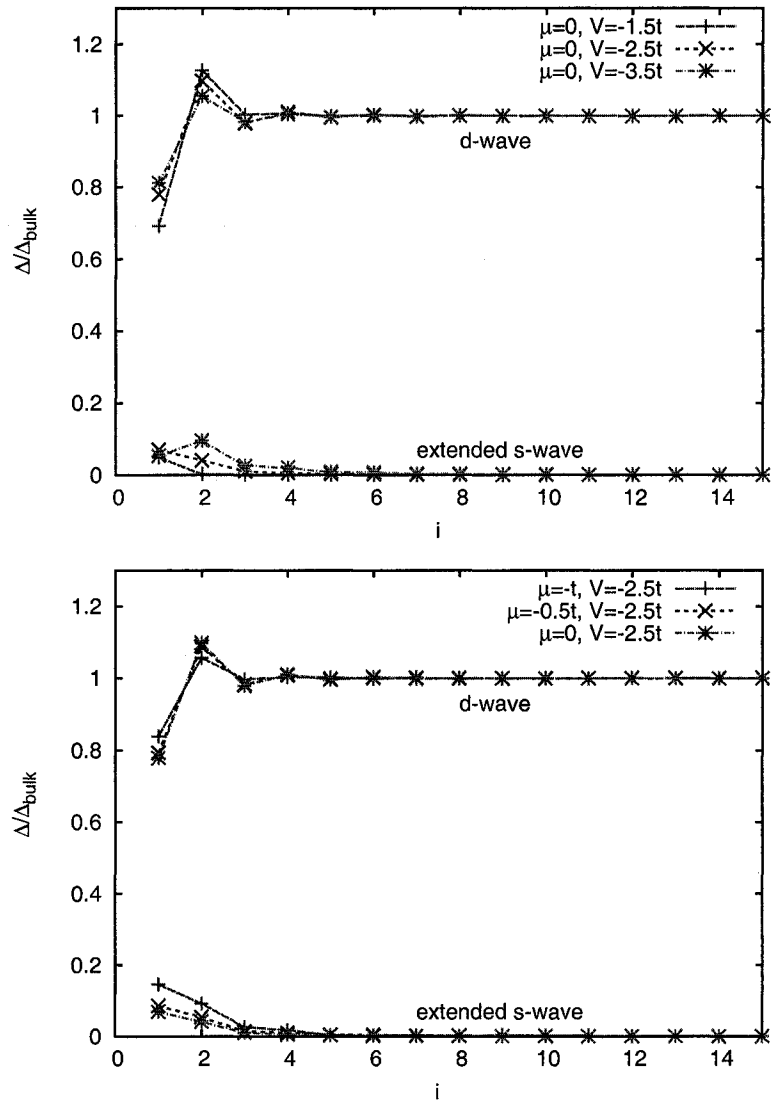

Figure 4.5: D-wave and extended s-wave order parameters near the (100) surface

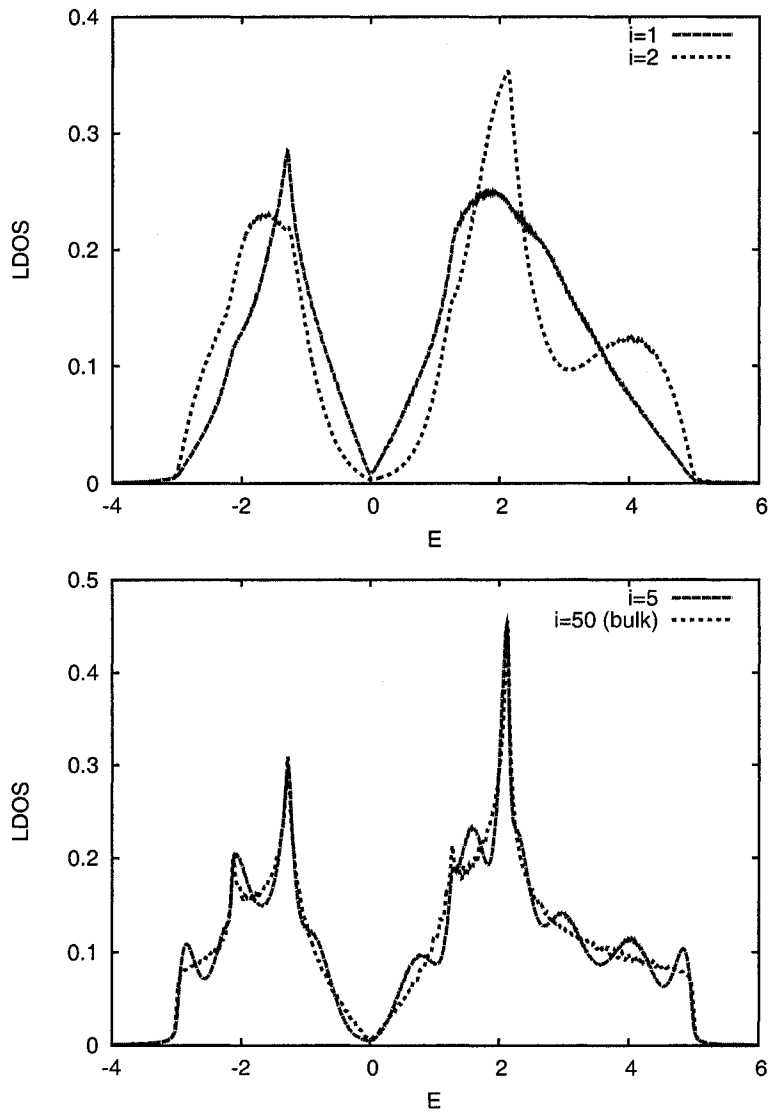

Figure 4.6: LDOS at various distances from the (100) surface; $U = 0$, $V = -3.5t$, $\mu = -t$

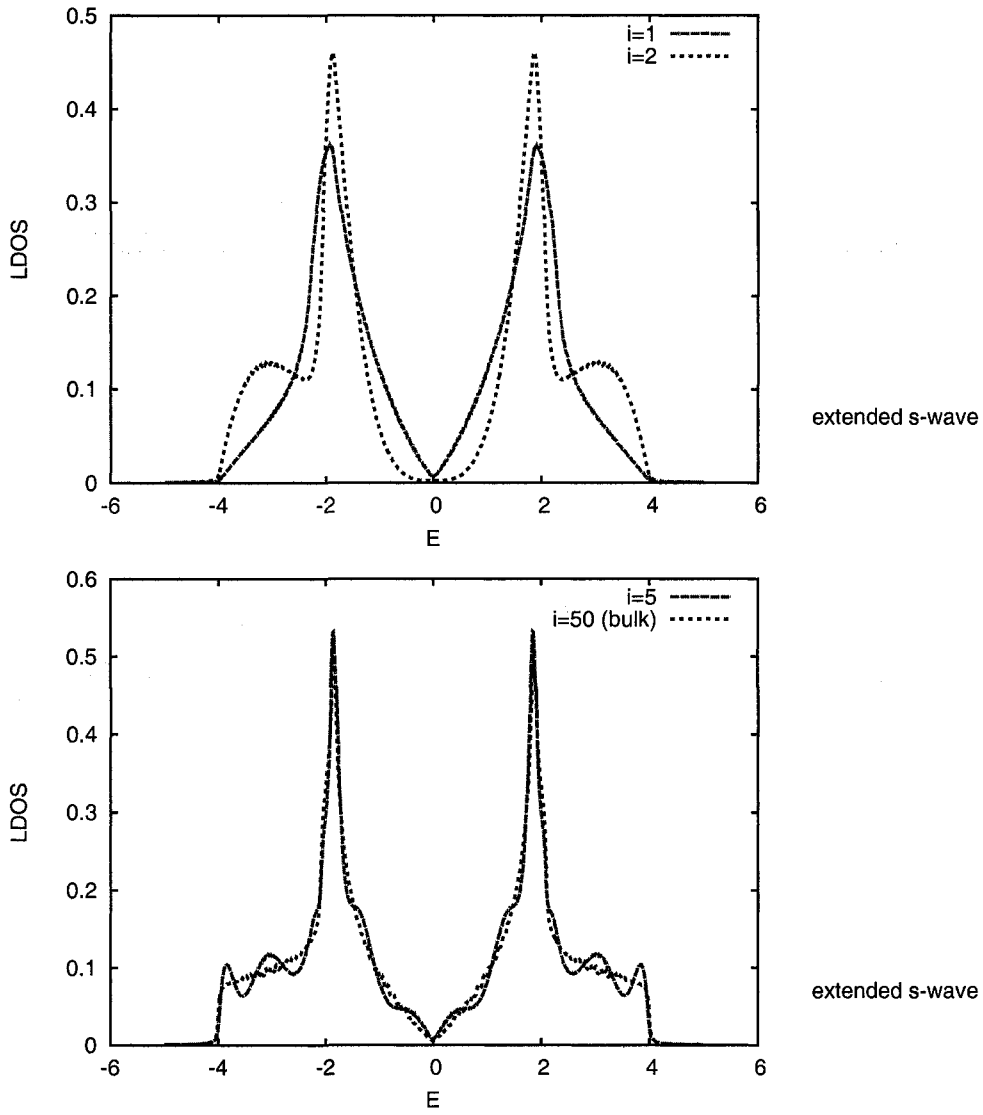

Figure 4.7: LDOS at various distances from the (100) surface; $U = 0$, $V = -3.5t$, $\mu = 0$

Superconductivity near the 110 surface

Interesting behavior near the (110) surface has been reported experimentally in tunneling experiments [21, 28, 92, 93] and has been predicted theoretically [18, 20, 94–98]. Although the same principle used for the (100) surface can be also applied here, the geometry of the (110) surface, complicates the calculation. The smallest unit needed to create a (110) surface is now formed by two adjacent sites, which will have different properties. We call them the A and B type. The methodology of Fourier transforming the (110) surface was presented in a previous chapter (3.2.2),and allows us to describe the surface in terms of a one dimensional problem.

For the d-wave superconductor near the (110) surface we calculate self-consistently the order parameter. In Figure 4.8, we present the d-wave and extended s-wave components of the order parameter for various choices of pairing potentials V and chemical potentials μ. In contrast to the (100) surface, the order parameter varies smoothly near the surface, in concordance with the quasi-classical results. The "healing" distance defines once again the coherence length in the superconductor and has an inverse proportional relation with the pairing potential, and thus with the order parameter. Also, for a fixed pairing potential, the coherence length increases with decreasing chemical potential. In these calculations, the coherence length is observed to be greater that 5 lattice spacings.

A peculiarity observed only for d-wave superconductors near the (110) surface, is the appearance of an extended s-wave component near the surface phase shifted from the d-wave component by $\pi/2$. It is important to note that this s-wave component is induced only at the surface, and that the magnitude of the s-wave component is dependent on both V and μ. The order parameter near the surface is in the form, $d + is$. Previous considerations of this scenario [24, 25] came to the conclusion that the existence of the imaginary s-wave components is equivalent to a state in which time-reversal symmetry is broken, thus spontaneous current form near the surface.

As in the (100) case, we set out to calculate the LDOS for various sites near the surface. The LDOS for sites near the surface, for a choice of parameters $V = -2.5t$ and $\mu = -t$ is presented in Figure 4.9. When compared to the (100) case, we can immediately observe the differences. A strong peak for zero energy develops at the surface. In tunneling experiments this is seen for zero bias, hence the name Zero Bias Conductance Peak (ZBCP). The height of the peak vanishes rapidly in the superconductor, and is completely absent for the B-type sites. The existence of the ZBCP has been predicted theoretically [20, 97], and is in direct relation to the formation of a bound state at the surface. The bound state forms when electrons specularly reflected at the (110) surface encounter an alternating sign order parameter upon two consecutive Andreev reflections. We will investigate further the formation of Andreev bound states in normal metal thin layers in contact with a superconductor in a subsequent section. It is important to note that the Andreev bound state is localized near the surface, thus any experimental probe of the surface will see completely different behavior for the (110) surface as compared

to the (100) one.

An even more interesting phenomenon happens when the system is not at half-filling. In Figure 4.10, we plot the LDOS for sites near the (110) surface, for $V = -2.5t$ and $\mu = -t$. The previously observed ZBCP is now split and it is observed both for sites of the A and B. Again, the height of the peaks goes down rapidly for sites inside the superconductor. In order to investigate further the splitting of the ZBCP, we plot in Figure 4.11, the LDOS at the surface site for various choices of order parameters and chemical potentials. In the upper graph, as the pairing potential increases, from $V = -1.5t$ to $V = -2.5t$, the splitting of the ZBCP appears and increases with increasing V. In the lower graph, the splitting is observed to decrease as the chemical potential increases from $\mu = -t$ to $\mu = 0$. There is a direct correlation between the magnitude of the imaginary extended s-wave component and the amount of splitting. The Andreev bound state is doubly degenerate because states with momenta parallel to the surface but pointing in the opposite direction, have the same energy. The existence of a broken time-reversal symmetry state, which induces spontaneous currents at the surface, will break the degeneracy of the Andreev bound states, and thus the ZBCP is split. A similar scenario is obtained in magnetic field. Increasing the magnetic field will generate surface currents and thus lift the degeneracy of the Andreev bound states.

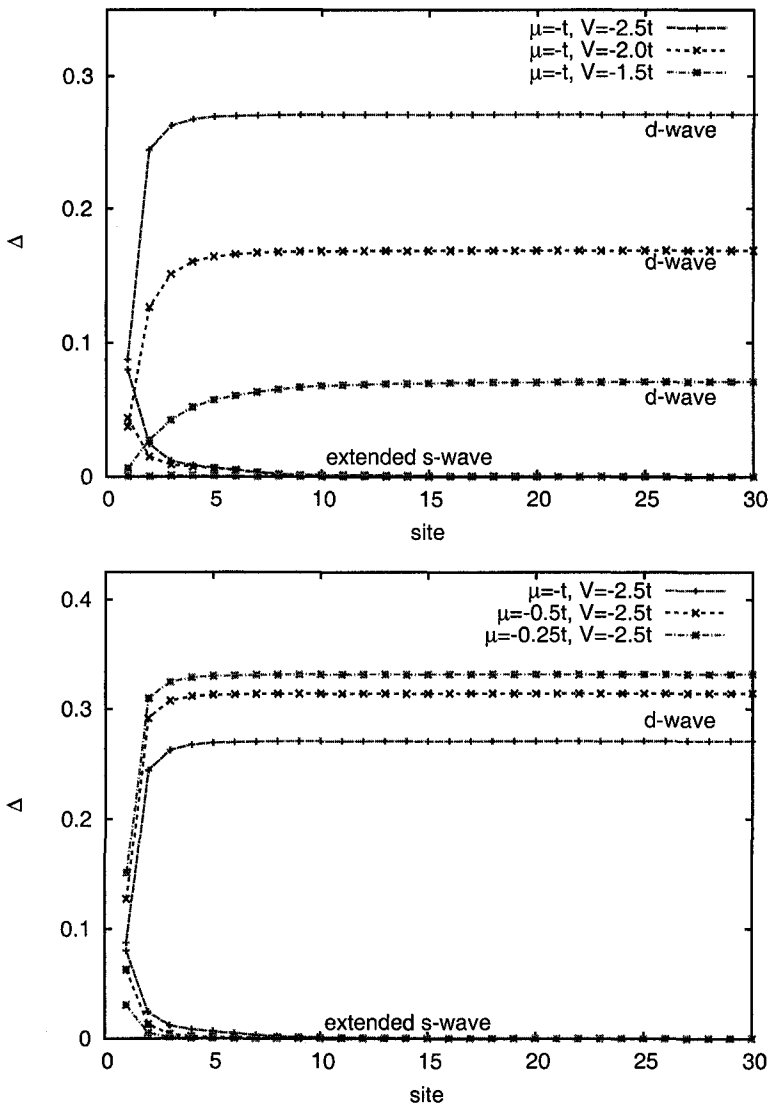

Figure 4.8: D-wave and extended s-wave order parameters near the (110) surface

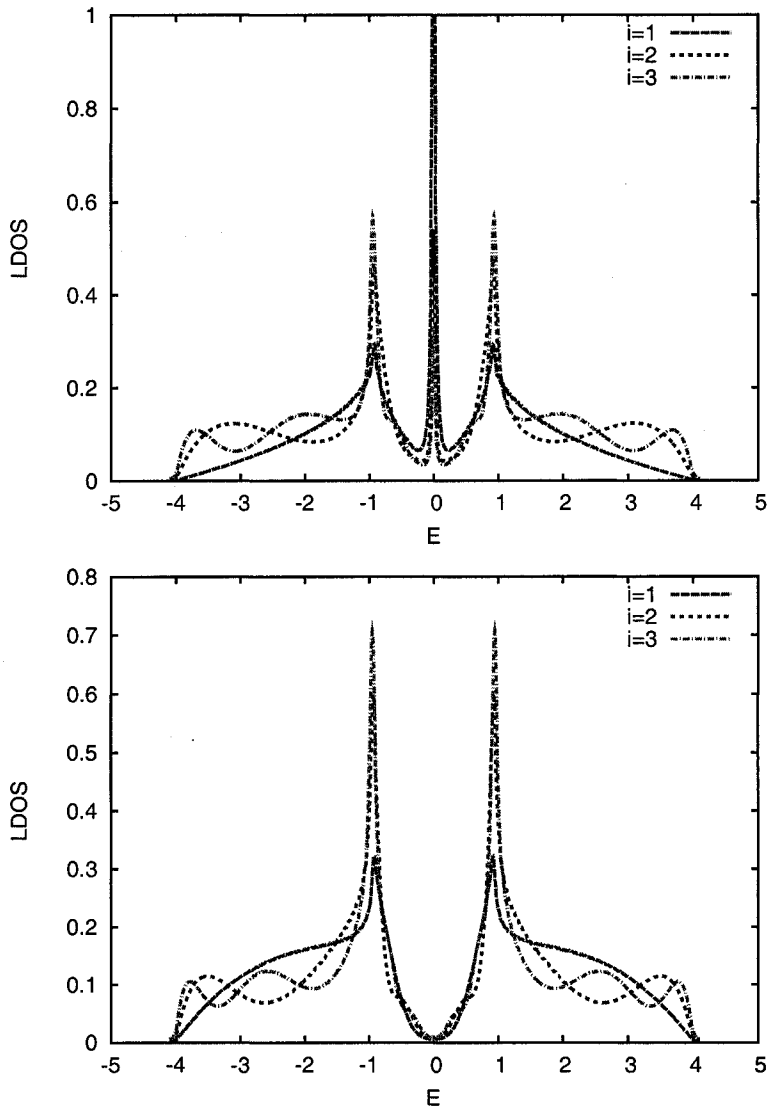

Figure 4.9: LDOS for various sites of type A (upper) and of type B (lower) near the (110) surface; $U = 0$, $V = -2.5t$, $\mu = 0$

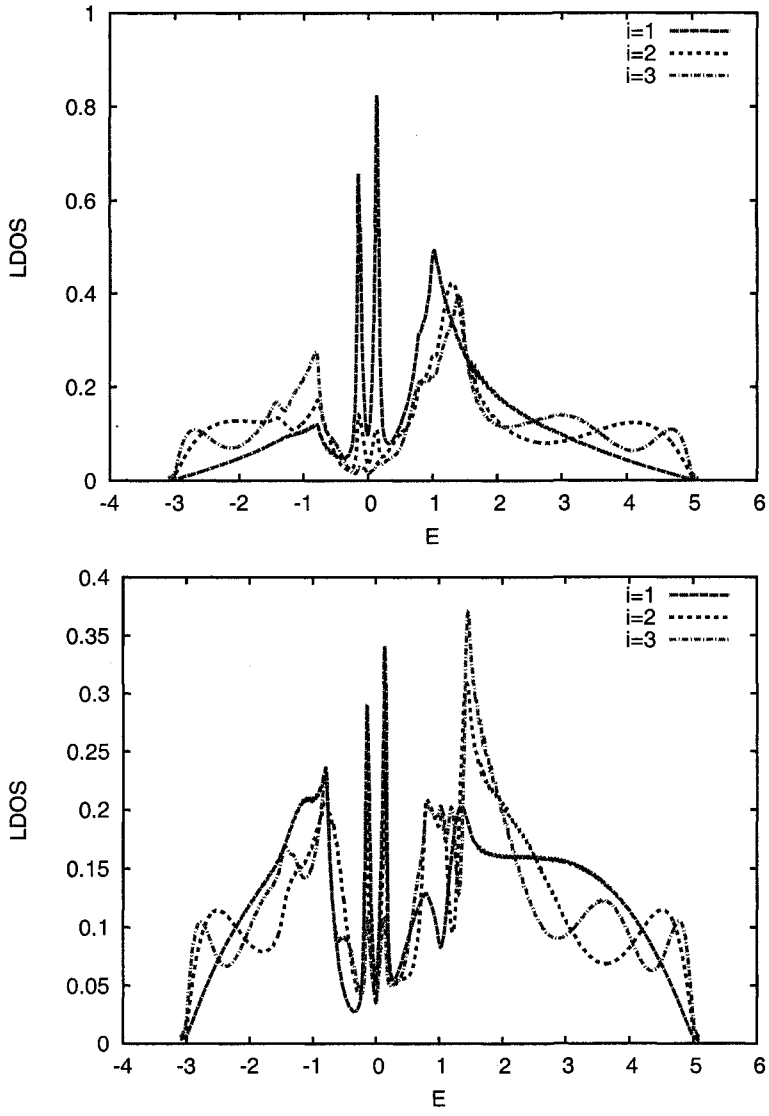

Figure 4.10: LDOS for various sites of type A (upper) and of type B (lower) near the (110) surface; $U = 0$, $V = -2.5t$, $\mu = -t$

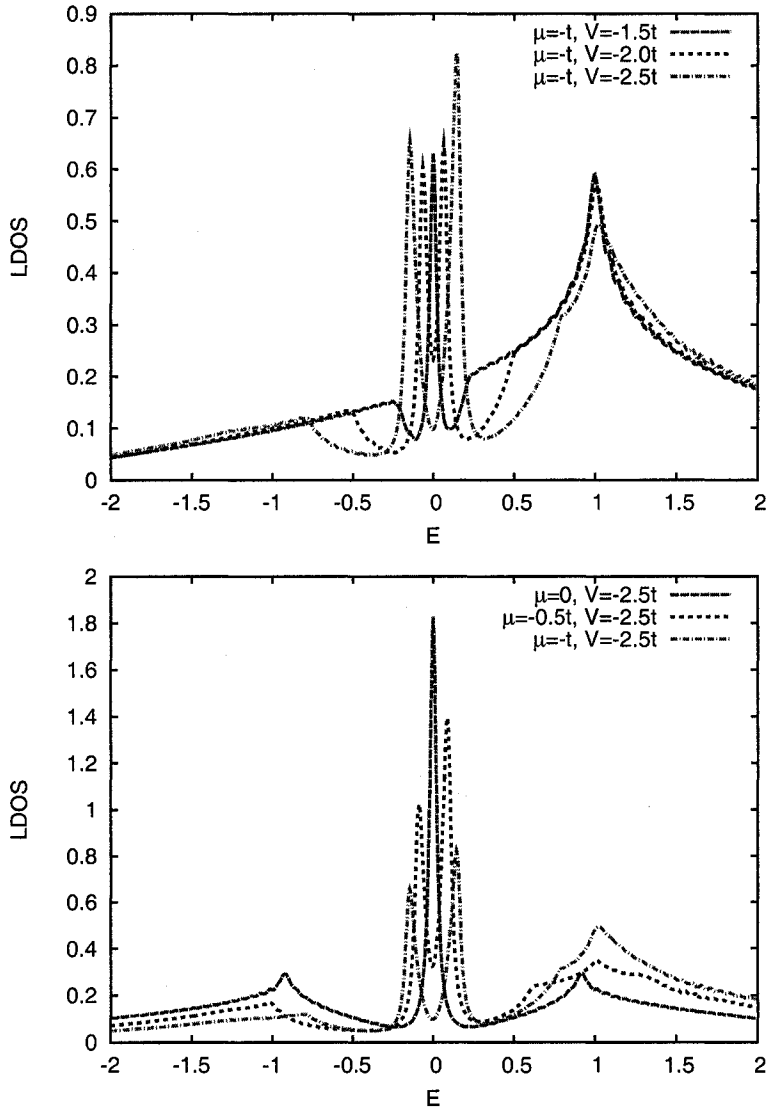

Figure 4.11: LDOS at the (110) surface of d-wave superconductor showing the dependence of the ZBCP splitting on V and μ

4.1.2 Rough surfaces

The existence of rough surfaces in experimental setups is inevitable. Usually the roughness is present at surfaces as faceting; small regions with differently oriented surfaces appear. Having in mind the huge difference between the surface properties of (100) and (110) for d-wave superconductors, one expects rough surfaces to show interesting behavior. This is seen in fact experimentally where (100) oriented surfaces show ZBCP [22,26,27] and (110) ion irradiated surfaces show a depression in the ZBCP [28]. This suggests that a mixture of (100) and (110) oriented regions is the correct way to think about a rough surface.

Using the two-dimensional method of fully diagonalizing the BdG matrix, we set out to investigate the influence of roughness on the LDOS near the surface, for a d-wave superconductors.

First we consider the (100) surface. We form a system of size $50a \times 30a$, and consider a rough surface on the $\hat{x}$ direction by randomly inserting strong impurities ($\xi_i = 100t$) at the surface. Since the impurity potentials are high compared to the hopping amplitude, quasiparticles will not reside on those impurities, and thus a rough surface is formed. There is randomness not only in the location of the impurities but also in the depth at which the impurities penetrate. Facets will form, some of them resembling the (110) geometry. For these locations we expect to see ZBCP forming. The equivalence between strong impurities and a surface has been previously considered [38].

The problem is solved self-consistently for a d-wave scenario. In Figure 4.12 we show the LDOS for a fixed impurity configuration, with $V = -3t$ and $\mu = 0$. Figure 4.12a shows the electron density; sites where impurities are present have zero electron density (shown in white), and define the rough surface. In Figure 4.12b we show the map of the LDOS for $E = 0$; the ZBCPs are observed where the LDOS is peaked, near the rough surface. We observe that facets on the order of one lattice spacing generates the strongest ZBCP. This can be seen in Figure 4.12c, where we plot the LDOS for three different locations on the surface of the superconductor at $x = 15, 25, 34$. Near site 15, the formation of a ZBCP is not favorable, while near sites 25 and 34, multiple facets are present, thus Andreev bound states form when quasiparticles specularly reflect on the boundary in the respective region.

An even rougher surface is considered in Figure 4.13. As shown in Figure 4.13a, up to three impurities can randomly appear at the surface, creating diverse facets with different shapes. The LDOS map for $E = 0$ is shown in Figure 4.13b. The density of the ZBCP is much higher than in the previous case, as there are step-like regions where the orientation is almost (110). This can be seen in the region next to $x = 25$ where strong ZBCPs form. In Figure 4.13c we show the LDOS for few sites, and observe that there is a wide range of LDOS shapes, from (100)-like to (110)-like.

A similar procedure can be applied to the (110) surface, if we consider a square $40a \times 40a$ lattice and put strong impurities on the diagonal in order to form a (110)

surface. Randomness in this surface is obtained by randomly inserting impurities on the off diagonals. Regions with facets of size 2×2 will form along the diagonal.

Again this is solved self-consistently using the full diagonalization method for the $40a \times 40a$ lattice. In Figure 4.14a we show the electron density for a random configuration with $V = -3t$ and $\mu = -t$. Figure 4.14b shows the LDOS map for $E = 0$. Regions where the (110) geometry is retained show strong ZBCP, while the regions where impurities are located, and 2×2 facets appear, are devoid of any ZBCP. LDOS for selected locations on the lattice are shown in Figure 4.14c. The region around $x = 24, y = 25$ shows a LDOS with strong ZBCP, while the region around $x = 34, y = 35$ has a LDOS looking more like the one obtained in the (100) geometry.

In some tunneling experiments (like planar tunneling junctions), we can only measure spatial averaged LDOS. In order to see how a rough surface will manifest in such experiments we average over a number of configurations, and over the surface of the superconductor. The results are shown in Figure 4.15, where we plot the averaged LDOS for various amounts of roughness at the (100) surface (top graph) and at the (110) surface (bottom graph). The amount of roughness is given by p, the probability to put an impurity at the surface. The main results is that, as we increase the roughness, a ZBCP appears at the (100) surface and increases in height with increased roughness. At the same time at the (110) surface, increased roughness will decrease the height of the ZBCP peak. This is the exact behavior observed in various tunneling experiments.

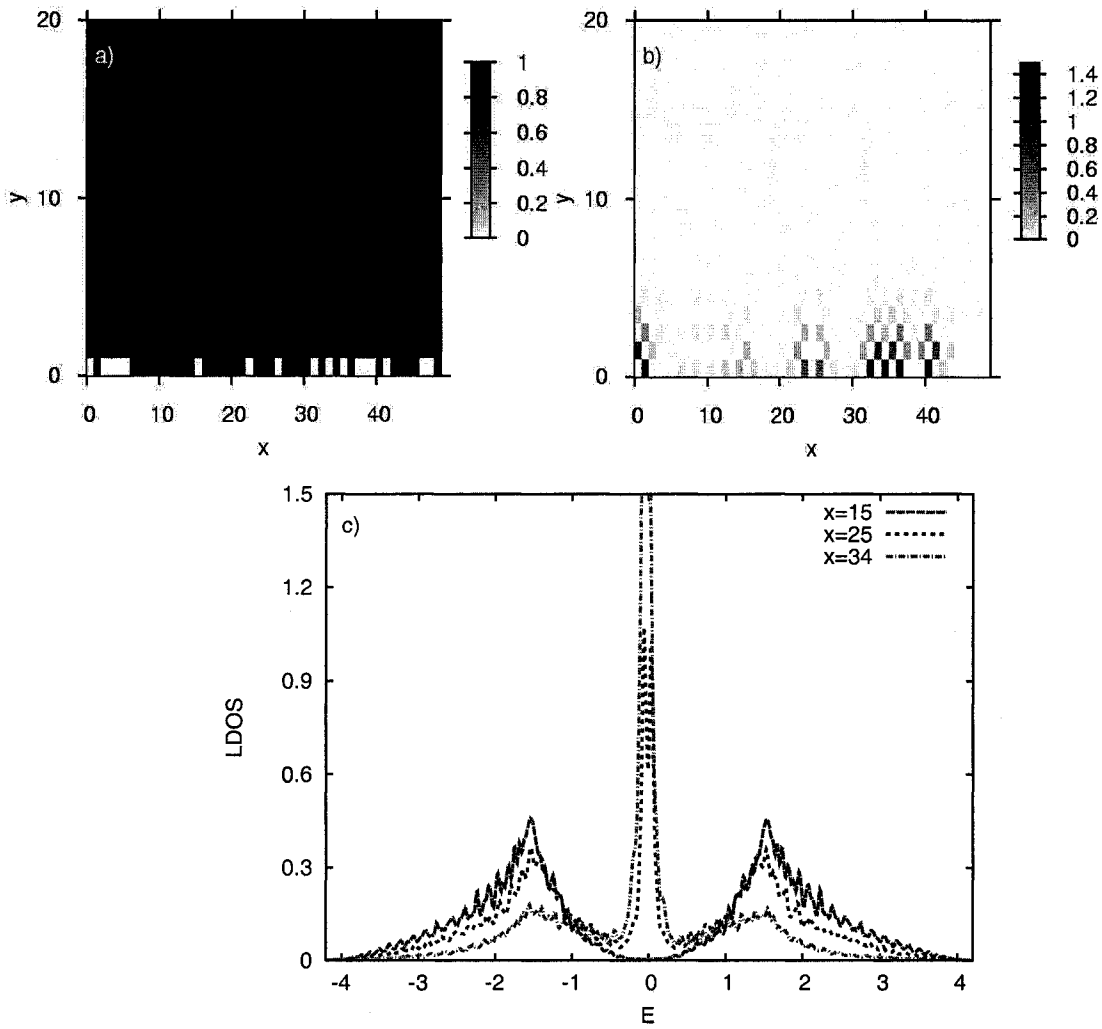

Figure 4.12: The 100 rough surface - a) electron density, b) LDOS map for $E = 0$, c) LDOS for selected locations; $V = -2.5t$, $\mu = 0$

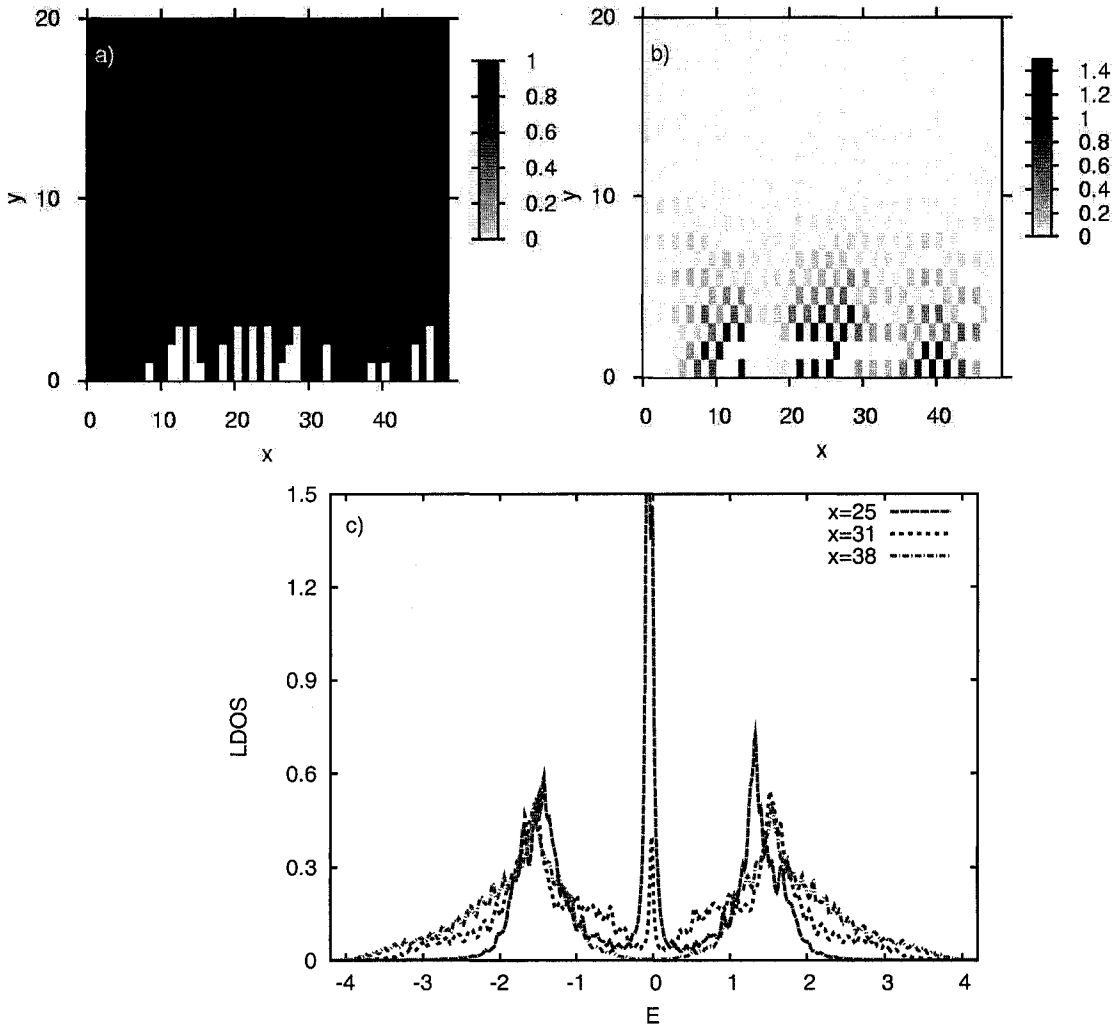

Figure 4.13: The 100 rough surface - a) electron density, b) LDOS map for $E = 0$, c) LDOS for selected locations; $V = -2.5t$, $\mu = 0$

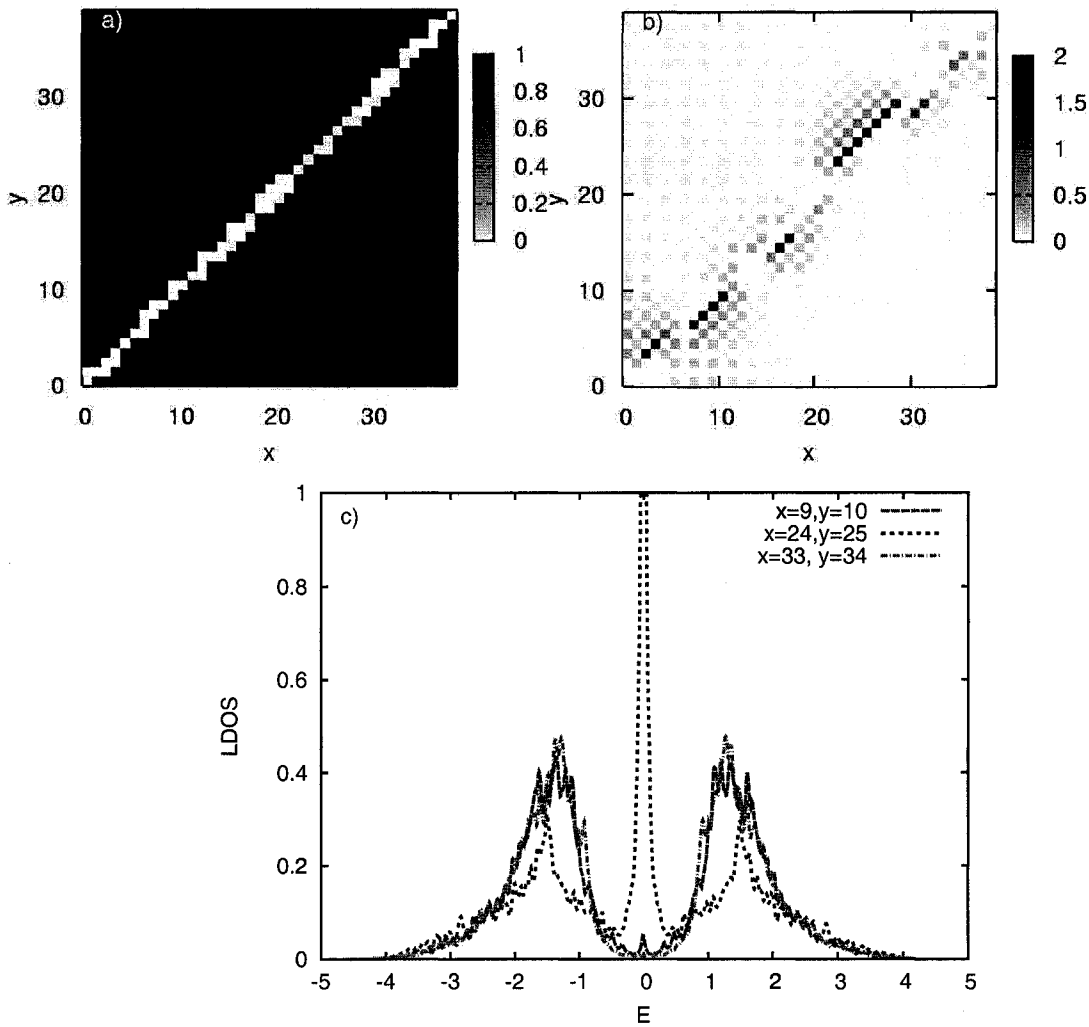

Figure 4.14: The 110 rough surface - a) electron density, b) LDOS map for $E = 0$, c) LDOS for selected locations; $V = -2.5t$, $\mu = 0$

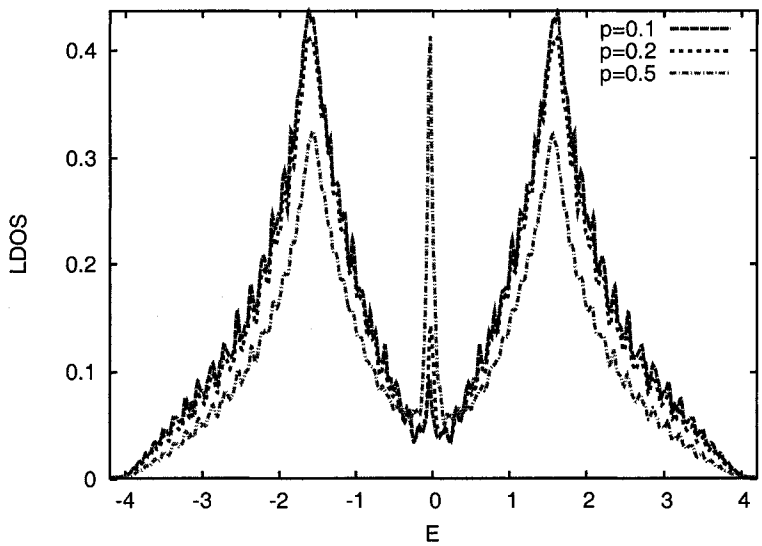

Figure 4.15: Averaged LDOS at the (100) surface for different roughness degrees

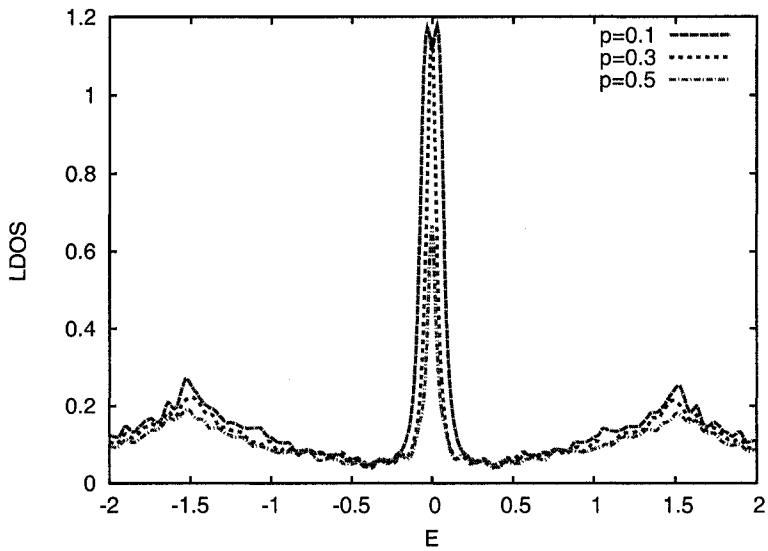

Figure 4.16: Averaged LDOS at the (110) surface for different roughness degrees

4.1.3 Finite systems

So far we have considered infinite surfaces for both s-wave and d-wave symmetries of the order parameter. The most general 2D inhomogeneous case is the one for which the translational symmetry is broken in any direction. This is certainly the case for a square system. Similar work has been previously done [90, 99].

We solve the self-consistent BdG equations for square samples for s-wave and d-wave superconductors. We focus our attention first on the s-wave system. In Figure 4.17, we show the on-site s-wave order parameter for $U = -1.5t$, $V = 0$, $\mu = -t$ and $T = 0.001t$. First of all it is important to note that the order parameter oscillates near the surface. Much like the infinite surface case, Friedel-like oscillations appear near the surfaces. For this low value of the pairing potential, the coherence length in the superconductor is large. Interference effects from the 4 surfaces with the vacuum are observed, making the oscillations near the corners more pronounced. For this choice of parameters, the order parameter is enhanced at the surface. For the same configuration, we plot in Figure 4.18 the electron density. Again, the same Friedel oscillations are observed, along with interesting interference effects near the corners. Right at the corner the electron density is suppressed. If we change the chemical potential to $\mu = 0$, the order parameter is shown in Figure 4.19. The overall oscillations are gone, but strong interference effects modify the order parameter along the diagonals. Right at the surface the order parameter is now suppressed. Furthermore, if we increase the pairing potential to $U = -4t$ (strong coupling), all the oscillations and interference patterns are gone. The coherence length in this case is very short, comparable to the lattice spacing, and the order parameter increases sharply at the surface (Figure 4.20).

The d-wave square lattice is solved in a similar manner, by using the direct diagonalization of the BdG matrix. In Figure 4.21, we plot the d-wave order parameter for $U = 0$, $V = -1.5t$, $\mu = -t$ and $T = 0.001t$. Similar behavior to the s-wave case is observed; Friedel-like oscillations in the electron density and in the order parameter appear at the surface. The d-wave order parameter is always suppressed at the surface, because one of the link order parameters is always zero. Interference patterns are also observed on the diagonal. In Figure 4.22 we plot the extended s-wave order parameter for the same choice of parameters. Deep inside the superconductor, the extended s-wave order parameter cannot coexist with the d-wave one, it is only next to the surface that the suppression of the d-wave order parameter will induce an extended s-wave component. This is similar to the infinite surface case. Differences appear near the corners, where the extended s-wave component oscillates and changes sign. Next, if we plot the electron density for this configuration (Figure 4.23), oscillations near the surfaces and corners are present. Interference effects, similar to those observed for the s-wave case are also seen here. An increase in the chemical potential (Figure 4.24), washes away most of the oscillations.

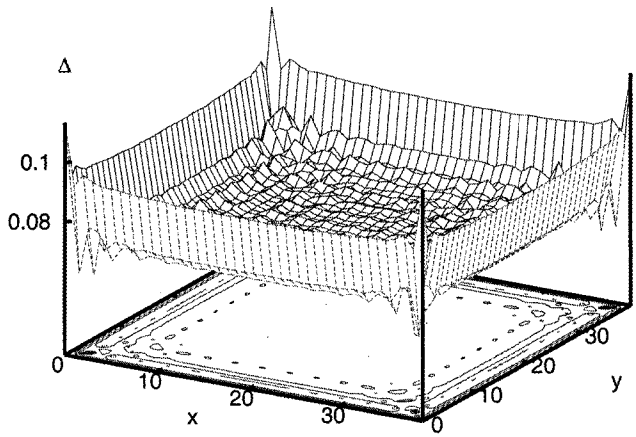

Figure 4.17: On-site s-wave Order parameter for a 40×40 lattice with $U = -1.5t$, $V = 0$, $\mu = -t$ and $T = 0.001t$

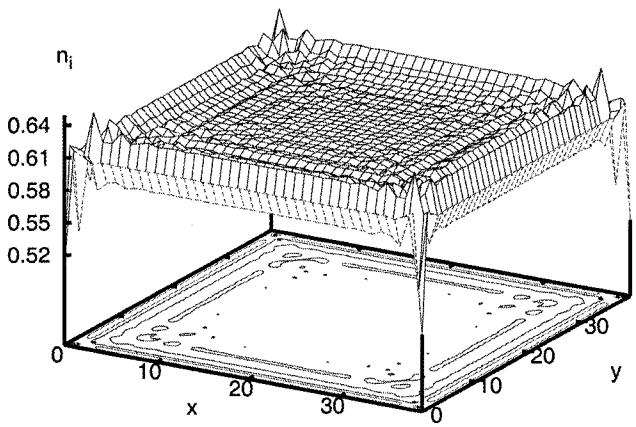

Figure 4.18: Electron density for a 40×40 lattice with $U = -1.5t$, $V = 0$, $\mu = -t$ and $T = 0.001t$

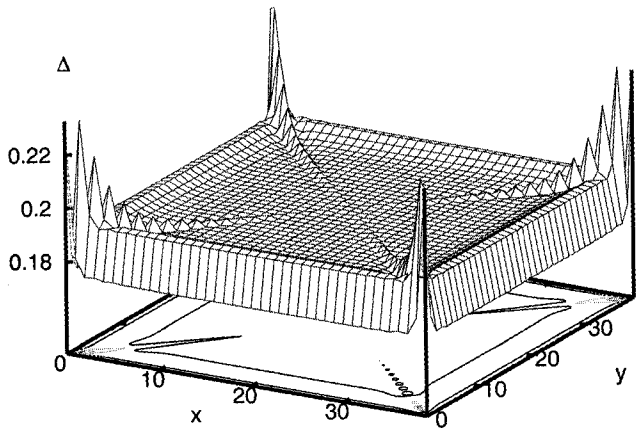

Figure 4.19: On-site s-wave order parameter for a 40×40 lattice with $U = -1.5t$, $V = 0$, $\mu = 0$ and $T = 0.001t$

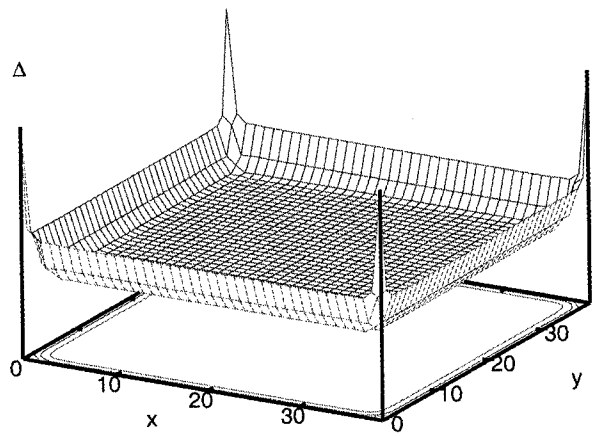

Figure 4.20: On-site s-wave order parameter for a 40×40 lattice with $U = -4t$, $V = 0$, $\mu = -t$ and $T = 0.001t$

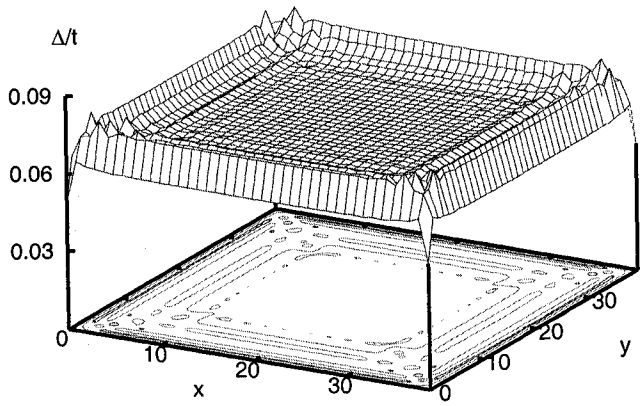

Figure 4.21: D-wave order parameter for a 40×40 lattice with $U = 0$, $V = -1.5t$, $\mu = -t$ and $T = 0.001t$

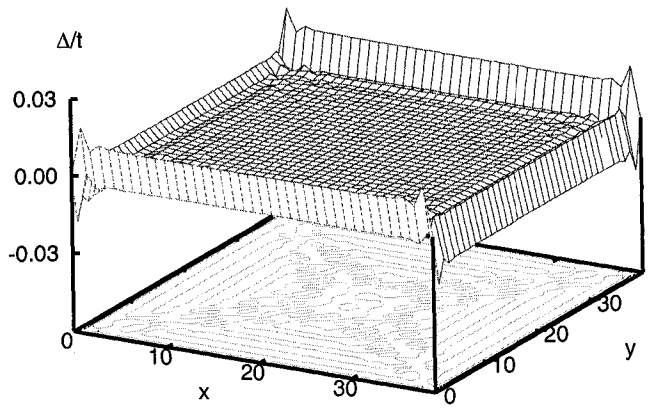

Figure 4.22: Extended s-wave order parameter for a 40×40 lattice with $U = 0$, $V = -1.5t$, $\mu = -t$ and $T = 0.001t$

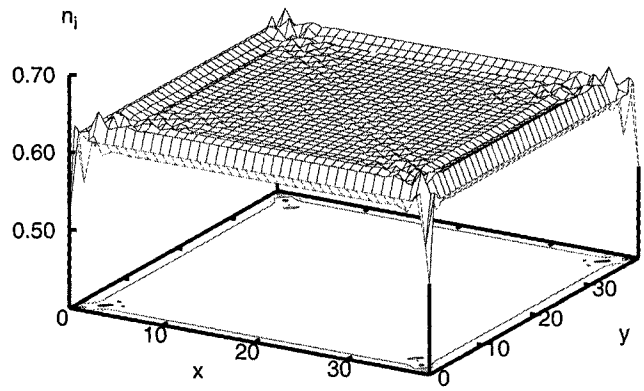

Figure 4.23: Electron density for a 40×40 lattice with $U = 0$, $V = -1.5t$, $\mu = -t$ and $T = 0.001t$

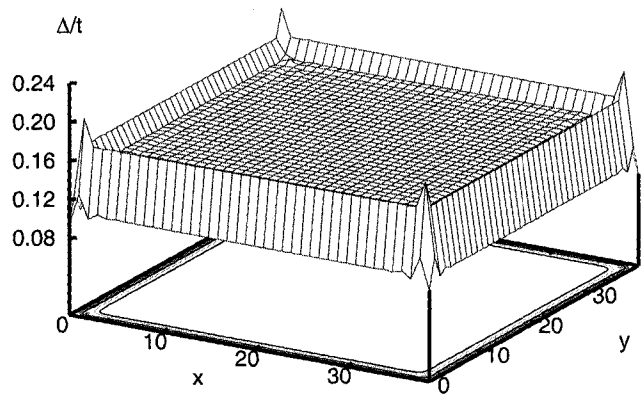

Figure 4.24: D-wave order parameter for a 40×40 lattice with $U = 0$, $V = -1.5t$, $\mu = 0$ and $T = 0.001t$

4.2 The giant proximity effect

The proximity effect between a superconductor and a normal metal has been thoroughly investigated using various techniques: Ginzburg-Landau theory [53–55], quasi-classical Green function methods [100], Gorkov equation methods [101–105], and tight-binding BdG methods [106–108]. We will focus our attention towards a scenario that didn't get much attention. Driven by recent experiments in high T_c superconductors we will investigate the proximity effect between two superconductors with different transition temperatures. When the temperature is higher than the critical temperature of the weak superconductor, it becomes a normal metal. The question we wish to ask is whether this scenario can be treated using the conventional proximity effect, or modifications are needed in order to account for superconducting correlations in the weak superconductor.

In a recent experiment [109] an unusually large proximity effect is reported, and the authors argue that it cannot be explained by the conventional proximity effect. The system used in the experiment is a c-axis oriented one. The c-axis Josephson critical current is measured through a thin film system made of doped LCO with $T_c = 25$K, sandwiched between optimally doped LSCO with $T_c = 45$K. The thin film is considered to be in the clean limit and because of the epitaxial growth of the films the transmission at the interfaces is close to unity and interface roughness is on the order of the lattice constant. In a particular setup, the LCO thin film used had a thickness of 100Å. Fitting the critical current around T_c' the authors extract a coherence length in the LCO film which is two orders of magnitude larger than expected. Because of this discrepancy and the observation of non-zero critical current for $T < 30$K the authors reported this effect to be a "giant proximity effect".

The giant proximity effect is observed in underdoped cuprates, for temperatures $T > T_c'$ for which the middle layer is considered to be in the pseudo-gap state. Previous theoretical investigations of the giant proximity effect [110, 111] considered the N′ layer to be comprised of pockets of superconductivity. In a recent theoretical study [112], interstitial oxygen dopants are considered to modify locally the pairing interactions. The disordered dopants are enhancing the pairing interactions, thus increasing the size of the local gap. This was observed in recent STM experiments [52] in BSCCO, which showed that the regions of enhanced superconductivity are correlated with the positions of the interstitial oxygen atoms. Because of the proximity effect, the superconducting pockets will be coupled and current will flow through percolating paths. The presence of these pockets will effectively shorten the length of the weak link and the strong external superconductors will be coupled for values of the effective length comparable with the leaking distance. The modification of the leaking distance due to the finite value of T_c' will have an important influence on the effective length. Considering randomly distributed areas of strong superconductivity with critical temperature T_c embedded in the weak superconductor with T_c' we will calculate the critical Josephson current and find its dependence on the length of the weak link and on the volume of the embedded

superconducting pockets.

Although the Josephson junction has been thoroughly investigated in the past for both s-wave [113] and d-wave symmetries [114–119], we feel that the calculation of the Cooper pair leaking distance in the case of clean limit and superconducting weak links needs further investigation. We are interested in observing if the leaking distance will be influenced by the finite critical temperature of the weak superconductor. From an experimental point of view, one of the better suited experiments is the measurement of the Josephson critical current in weak links [120].

For coherent transport in the c-axis direction, the properties of the Josephson current for d-wave superconductors will be similar to the properties of the current for s-wave superconductors. For planar interfaces, with $\hat{z}$ the direction perpendicular to the interfaces, the d-wave order parameter will have no k_z dependence, $\Delta(k_x, k_y, k_z) \sim \Delta_0(cos(k_x a) - cos(k_y a))$ and therefore will have properties similar to a superconductor with s-wave symmetry. When Fourier transforming the $\hat{x}$ and $\hat{y}$ directions, and considering an effective 1D problem in the $\hat{z}$ direction, the d-wave order parameter will be due to an effective on-site interaction within each ab-plane. We will calculate the Josephson current in the c-axis direction for a 3D d-wave superconductor. We will also show calculations of the Josephson critical current and the Cooper pair leaking distance for a 2D s-wave superconductor and for the 100 interface of a 2D d-wave superconductor.

The calculations are done using the self-consistent solution of the BdG equations applied to (100) surfaces both for s-wave and d-wave superconductors [121]. When disorder is considered a full 2D calculation without translational symmetry is required. The self-consistent calculation of the order parameter ensures that the order parameter in the "normal metal" region has knowledge about the pair potential in this layer. If the initial guess is a step function, i.e. the order parameter in the middle region is zero, after one iteration the pair amplitude will become non-zero because of the proximity effect. In the case $U' = 0$, the order parameter will remain zero: $\Delta \sim U_i' < c_{i\uparrow} c_{i\downarrow} >$, while for the case $U' < 0$ the new order parameter has a finite value throughout the layer. If we were to fix the order parameter in the superconducting regions (we do not), the $U' = 0$ solution would need only one iteration to converge.

The BdG formalism allows us to calculate the dc current in the absence of applied voltages. In the tight-binding formulation the current operator is:

$$J_{ij} = \sum_{\sigma} t_{ij}(c_{i\sigma}^{\dagger} c_{j\sigma} - c_{j\sigma}^{\dagger} c_{i\sigma}). \tag{4.1}$$

The expectation value of the current will be non-zero only if the order parameters in the two superconducting layers have different phases. For the mean-field Hamiltonian with s-wave order parameters one gets for the continuity equation:

$$< \frac{\partial n_i}{\partial t} > \; = \; < [H, n_i] >$$

$$= \sum_{\sigma} t_{ij}(< c^{\dagger}_{i\sigma}c_{j\sigma} > - < c^{\dagger}_{j\sigma}c_{i\sigma} >) + < c_{i\downarrow}c_{i\uparrow} > \Delta^{\star}_{i} - < c^{\dagger}_{i\uparrow}c^{\dagger}_{i\downarrow} > \Delta_{i} \tag{4.2}$$

If the order parameter is calculated self-consistently $\Delta_i \sim< c_{i\downarrow}c_{i\uparrow} >$, then we recover the continuity equation, $< \frac{\partial n_i}{\partial t} >=< J_{ij} >$. Otherwise, if the order parameters are not calculated self-consistently but set to a desired value (the case of hard boundary) then the last two terms in Eq. (4.2) can be seen as current source terms.

In our calculation the coherence factors, u_k and v_k, are complex numbers and they will give the magnitude and the phase of the order parameters. The magnitude of the order parameters is calculated self-consistently and after each iteration the phase of the external layers is set to a desired value. For the calculation of the dc Josephson current we restrict the phase of the two superconductors to a desired phase difference, while for the weak link, the phase is calculated self-consistently.

Results for SN′S

For the $SN'S$ tri-layers the interactions are only on-site attractive interactions. The value of the parameter U_i will set the magnitude of the order parameter throughout the sample. We consider the following setup (Figure 4.25), $U_i = U$ for $0 < i < A$ and $B < i < N$, while $U_i = U'$ for $A < i < B$. In this particular case V_{ij} is vanishing, because we ignore the d-wave symmetry. The value of U' is chosen so that $|U'| < |U|$, allowing us to describe the N' material with a lower critical temperature T_c'. For temperatures greater than T_c' the $A - B$ region cannot sustain superconductivity by itself. The order parameter will leak from the stronger superconductors, and the characteristic length is called the "leaking" distance.

Figure 4.25 shows the order parameter profile for $U = -3t$, $U' = -2t$ and $T = 0.21t$. Note that $T_c' = 0.205t$ for the weak superconductor, while $T_c = 0.459t$ for the strong one. Similar to the $T_c' = 0$ case the order parameter has an exponential dependence on distance away from the interface, $\Delta \sim \Delta_0 exp(-x/\xi)$. This is true only for temperatures much larger than T_c' and for distances from the interface greater than the coherence length of the stronger superconductors. The coefficient of the exponential decay is given by the leaking distance, ξ. In the normal metal case ($T_c' = 0$ K) the clean limit leaking distance is inverse proportional to the temperature:

$$\xi = \frac{\hbar v_F}{k_B T}. \tag{4.3}$$

For the case of a weak superconductor, the relevant temperature scale is $T - T_c'$. Plotting the order parameter versus distance from the interface on a semi-log scale (Figure 4.26) for different temperatures, we can extract the leaking distance. As expected from the $T_c' = 0$ K case, the leaking distance is decreasing with increasing temperature.

If we plot the order parameter as a function of temperature for different lengths (L) of the weak link (Figure 4.27), we can observe two main effects. First, at $T = 0$ K, the proximity effect will modify the order parameter at $L/2$. For lengths smaller than 10 lattice constants this effect is important. Because the N' layer is superconducting at $T = 0$K, the main length scale in this layer is the superconducting coherence length $\xi = \hbar v_F/\Delta$. The second effect is observed at temperatures close to T_c'. If the N' layer was not connected to the superconducting layers, then, according to the mean-field behavior, the order parameter would vanish at T_c'. For temperatures higher than T_c' the N' layer cannot sustain superconductivity by itself. It is only in the presence of the S layers, that the order parameter at $L/2$ has non-zero values. Note that *the length L for which we obtain non-zero values of the order parameter above T_c' is much larger than the value of the length beyond which effects are unobservable at $T = 0$ K.* In Figure 4.28, we compare the order parameters at $L/2$ for two cases: $U' = 0$ and $U' = -2t$. We observe that the order parameter for the case $U' = -2t$ is larger and that close to T_c' the discrepancy is enhanced. This is a clear indication that the Cooper pair leaking distance is larger in the case of a non-zero T_c'.

In order to investigate further the dependence of the leaking distance on the magnitude of the superconducting correlations in the N' layer, in Figure 4.29, we summarize the extracted leaking distance obtained for different parameters. The $T_c' = 0$K line(dashed) is inversely proportional to the temperature, as expected. For $T_c' > 0$ K the leaking distance is diverging at T_c'; this, of course leads to a giant proximity effect near these temperatures, as the figure visually demonstrates. Another feature of the calculation is that for any given temperature, a higher T_c' will result in a larger leaking distance. For repulsive on-site interactions, $U' = +2t$, the leaking distance is even smaller than in the normal metal case. This is a clear demonstration of the fact that interactions in the N' layer will influence the way Cooper pairs leak from the superconducting side. Such "feedback" will not be captured in calculations that are not self-consistent.

The proximity effect can be observed either by growing superconducting thin films on top of normal metals and measuring the critical temperature of the system, or by forming a Josephson junction and measuring the Josephson current through the weak link. If the two superconducting sides are not coupled then there is no Josephson current. As we bring the superconducting sides closer to one another, the proximity effect will influence the value of the order parameter in the N' layer. A non-zero value of the order parameter throughout the whole system will result in a non-zero value of the Josephson current.

The BdG equations are well suited for calculating the dc Josephson current. In order to have current between the two superconducting sides, the order parameters in the two sides have to have different phases. In our calculation we fix the phases of the order parameter on the S layers, and our self-consistent calculation will give the magnitude and the phase of the order parameter in the N' side. The results of such a calculation are shown in Figure 4.30a and Figure 4.30b. The phase of the order parameter in N'

will vary continuously from ϕ_{left} to ϕ_{right} and the dc Josephson current will be constant throughout the layer. An interesting case is the one where $\Delta\phi = \pi$, for which there is a phase-slip point at $L/2$. Right at the phase-slip the order parameter vanishes. In order to extract only the proximity effect from the current calculation, we need to find the phase difference for which the current is maximal. For a point contact Josephson junction the current has the following behavior [122]:

$$J = J_m sin(\Delta\phi), \tag{4.4}$$

while for a long junction it deviates from the sinusoidal behavior [123].

We calculate the dc Josephson current for different lengths of the weak link and for different temperatures for $U' = -1.5t$ and $U = -3t$. The results are summarized in Figure 4.31. When the two superconducting layers (S) are close together the proximity effect modifies the magnitude of the order parameter at L/2 in the N′ layer. A large value of the order parameter will give a large value for the current. As L increases the order parameter decreases exponentially. This results in a decay of the current as a function of L. The main result is that the behavior of the Josephson current as a function of L and T reflects the existence of a leaking distance larger than the one expected from a normal metal. For $U' = -1.5t$ and $T = 0.125t$, the normal metal gives a leaking distance of $\xi_0 \sim 2a$ while the self-consistently calculated one gives a value of $\xi \sim 7a$. This is seen in Figure 4.31 where for $L = 16a$ the current is non-zero for temperatures close to but greater than T_c', and it has a linear dependence on temperature near T_c'.

As shown in previous attempts to explain the "giant proximity effect", the presence of pockets of superconductivity in the N′ layer will greatly enhance the current through the system, even for long weak links. Coupled with the enhancement of the leaking distance around T_c' the presence of the superconducting pockets will effectively decrease the length of the weak link. We consider randomly distributed superconducting areas with on-site interactions of strength $U = -4t$ embedded in the weak link with interaction strength $U = -2t$. In Figure 4.32 we show the Josephson current averaged over 50 configurations, for different lengths of the weak link and with superconducting pockets occupying a volume percentage $p = 0.1$ of the weak link. The size of the considered pockets is one lattice site. The effect on the Josephson current is drastic — the current has non-zero values well above T_c'. We also notice that for this volume of embedded superconductivity, the current has a weak dependence on the length of the junction.

The strength of the coupling between the exterior superconductors will be given by the volume of the embedded pockets. This is seen in Figure 4.33, where we plot the Josephson current for a weak link of length $L = 32a$ as a function of temperature for different percent volumes of strong superconducting pockets embedded in the weak superconductor. For $p = 0.0$ the junction is too long to couple the strong superconductors and the current vanishes above but very close to T_c'. Increasing p, the junction will effectively shorten and the two exterior superconductors will be coupled well above T_c'.

For a fixed temperature and a random configuration of strong superconducting pockets in the middle layer ($p = 0.1$), we perform self-consistent calculations of the order parameter and of the Josephson current. During the self-consistent calculation, phases for the strong superconductors are kept constant, while in the middle layer a full self-consistent phase gradient is obtained. The dc Josephson effect tells us that supercurrents will flow not only because of the existence of the phase gradient but also because of non-zero anomalous pair amplitudes in the middle layer. In Figure 4.34 we present the Josephson current for such a configuration. The full circles represent the sites where $U = -4t$ while the rest of the sites have a lower on-site interaction $U' = -2t$. As shown before, for a temperature higher than T_c' the order parameter on the sites with $U' = -2t$ should be zero if those sites are isolated.

Because of the vicinity with the stronger superconductor, the proximity effect provides a way of obtaining non-zero pair amplitude. Due to the phase gradient, the current will flow through percolating paths. The current is higher for sites where the order parameter is higher. Maximum current is obtained for clustered pockets of superconductivity (lower part of Figure 4.34). The order parameter as a function of location in the middle layer is presented in Figure 4.35. The proximity effect is observed from both the outside layers and from the embedded pockets of strong superconductivity. The absolute value of the current for the same configuration is presented in Figure 4.36 and it is seen to be correlated with the magnitude of the order parameter in the middle layer.

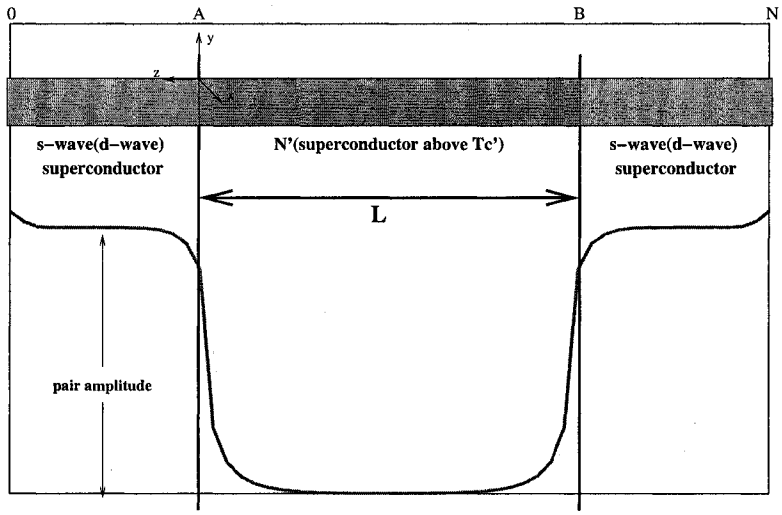

Figure 4.25: The pair amplitude profile through a Josephson junction. The pair amplitude is shown for $U = -3t$ and $U' = 0$. The regions $0 - A$ and $B - N$ are superconducting, while the region $A - B$ is a superconductor above its critical temperature. The interfaces are considered to have perfect transmission and the whole system is in the clean limit.

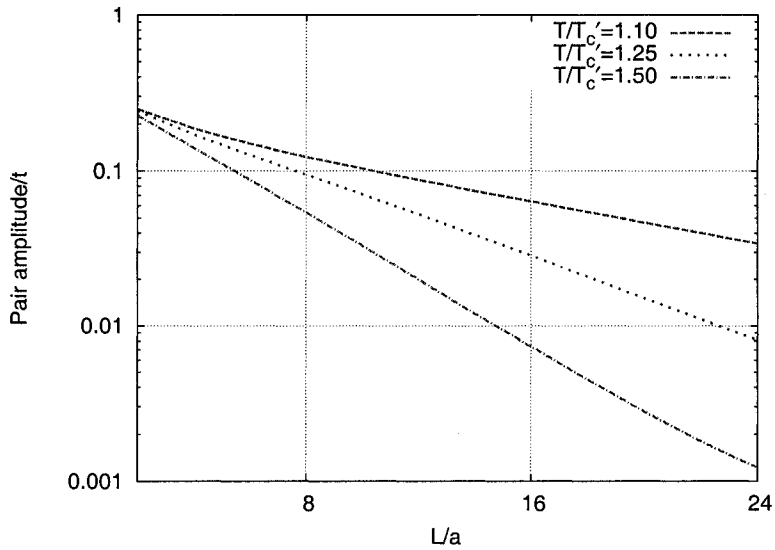

Figure 4.26: The pair amplitude at L/2 as a function of L for different temperatures above T_c' for the SN'S system with $U' = -2t$ and $U = -4t$.

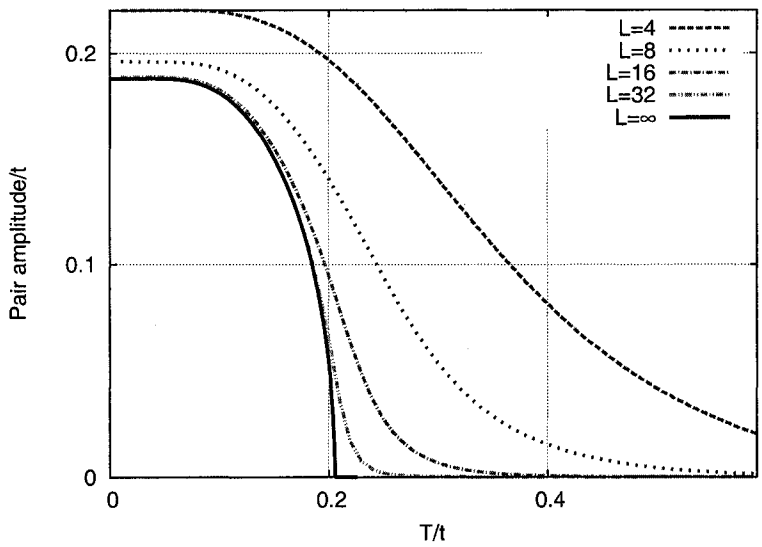

Figure 4.27: The pair amplitude at L/2 as a function of temperature for different L for the SN′S system with $U' = -2t$ and $U = -4t$.

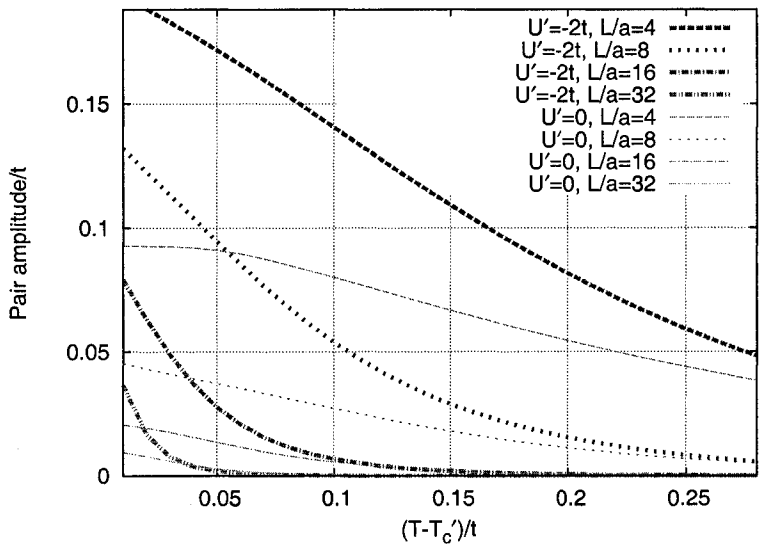

Figure 4.28: The pair amplitude at L/2 as a function of relative temperature for different L for the SN′S system for $U = -4t$, $U' = 0$ and $U = -4t$, $U' = -2t$.

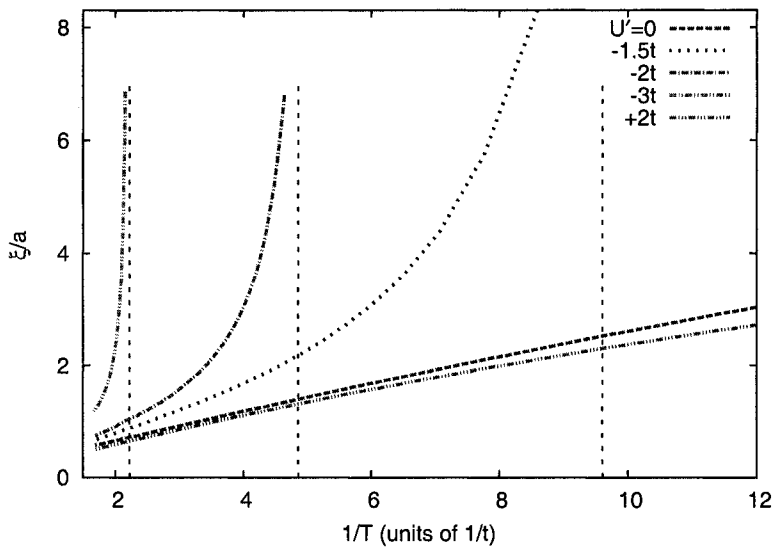

Figure 4.29: The leaking distance as a function of 1/T for different interaction parameters U' for the SN'S system with $U = -4t$. The vertical dashed lines represent the inverse of the critical temperatures for the corresponding U' parameters: $T_c(U' = -1.5t) = 0.104t$, $T_c(U' = -2t) = 0.205t$, $T_c(U' = -3t) = 0.46t$.

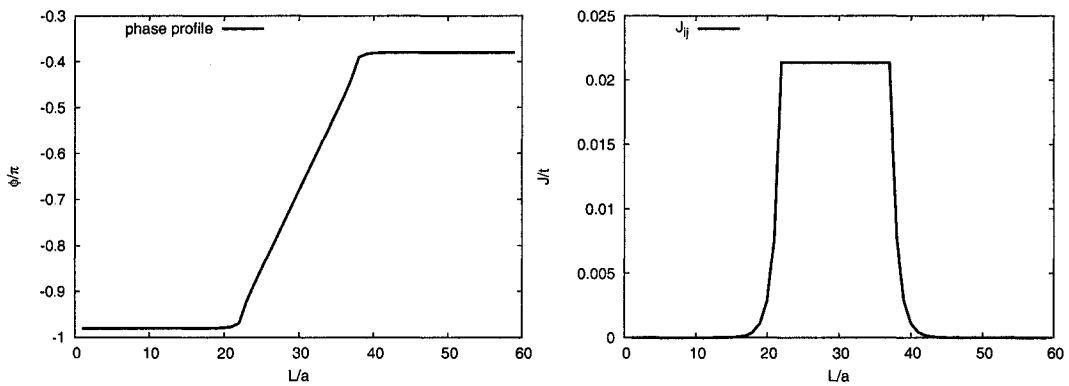

Figure 4.30: (a) Phase profile and (b) dc Josephson current as a function of position. The phase is calculated self-consistently only in the middle layer and the continuity equation is satisfied only in this layer.

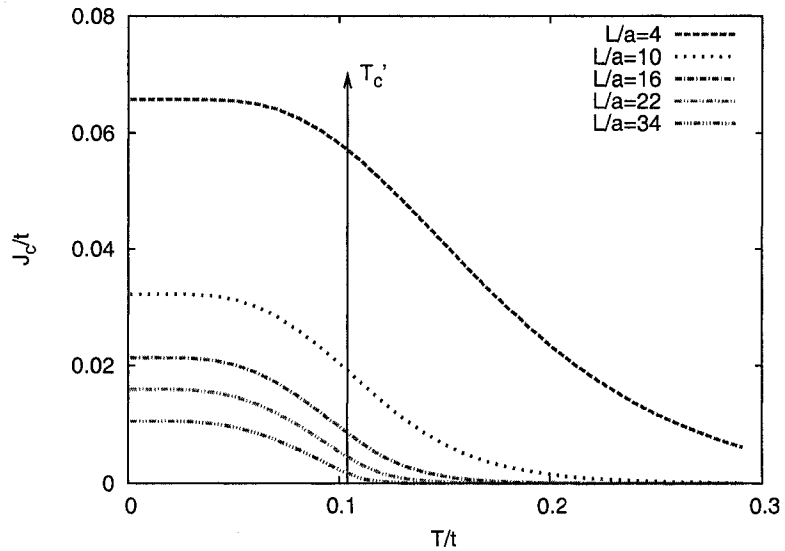

Figure 4.31: The dc Josephson current in the middle layer as a function of temperature for different lengths L of the weak link for the SN′S system with $U = -3t$ and $U' = -1.5t$. The arrow represents the critical temperature of the middle layer, $T_c(U' = -1.5t) = 0.104t$.

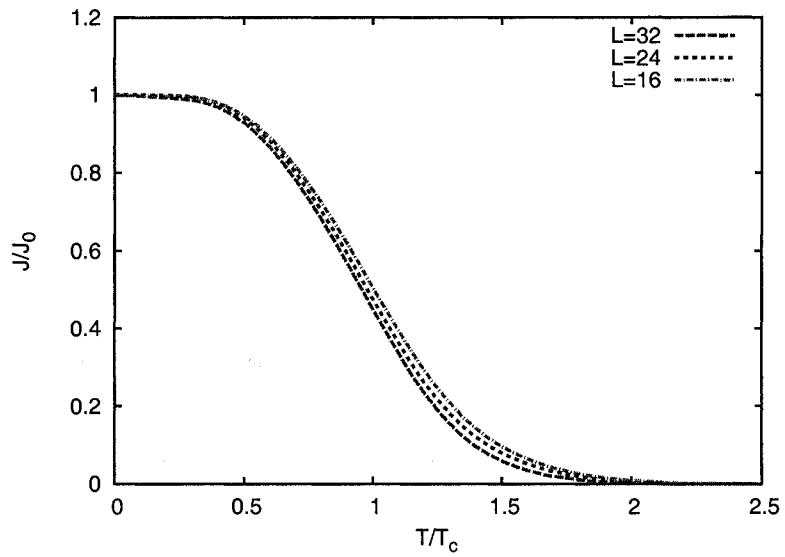

Figure 4.32: The dc Josephson current in the middle layer as a function of temperature for different lengths L of the weak link for the SN′S system with $U = -4t$ and $U' = -2t$. Randomly distributed areas of superconductivity in the N′ layer are considered. The percent volume of the pockets of superconductivity with $U = -4t$ is $p = 0.1$.

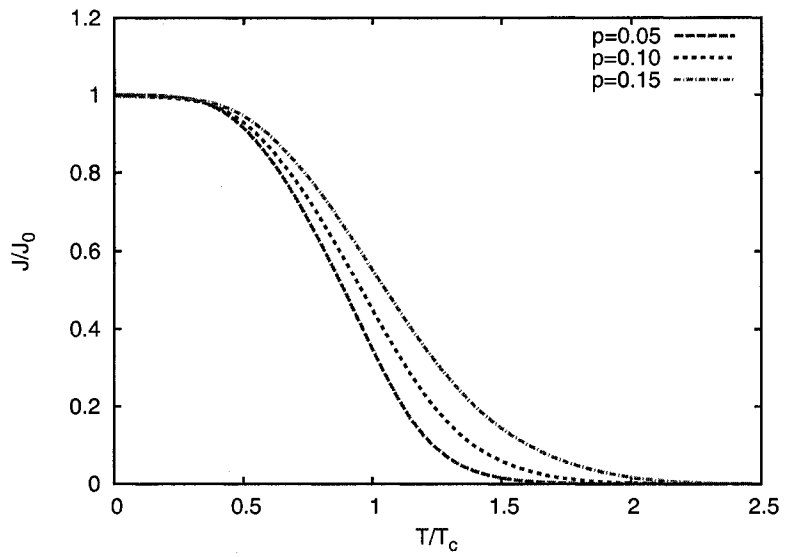

Figure 4.33: The dc Josephson current in the middle layer as a function of temperature for different percent volumes of embedded superconductivity in N′ for the SN′S system with $U = -4t$ and $U' = -2t$. The length L of the weak link is $L = 32a$.

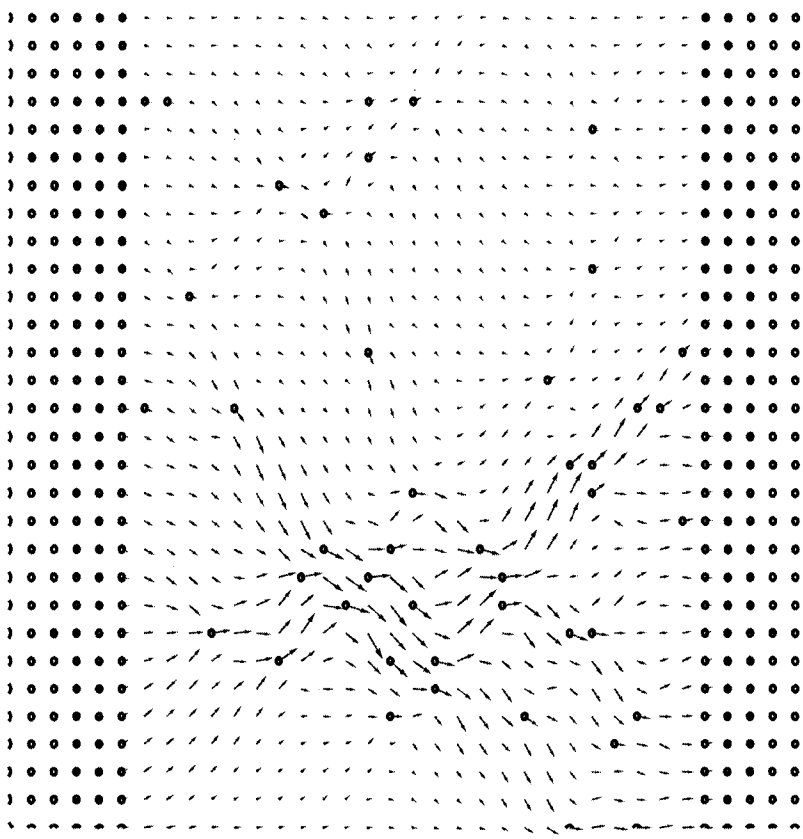

Figure 4.34: Josephson current through a disordered junction. Here $T = 0.25t > T_c'$. At the location of the dots $U = -4t$, elsewhere $U = -2t$.

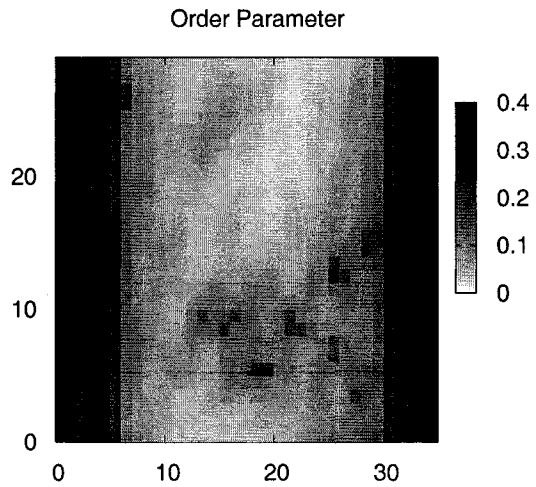

Figure 4.35: Magnitude of the order parameter for a disordered junction

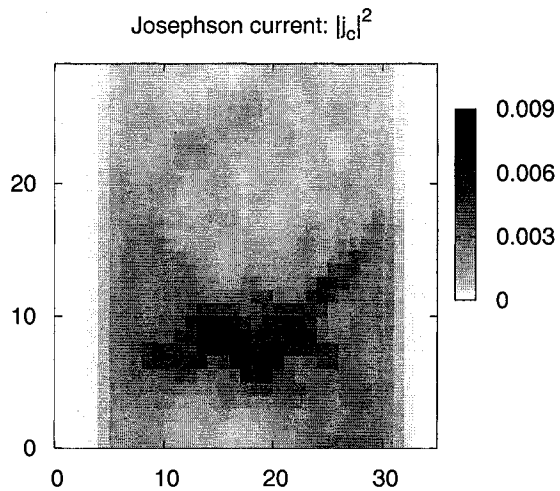

Figure 4.36: Magnitude of the Josephson current through a disordered junction

Results for DN′D

The d-wave symmetry of the order parameter is attained if we consider nearest-neighbor interactions $V_{ii+\delta} = V_i$ and vanishing or repulsive on-site interactions. In a similar manner, as detailed in the SN′S case, we set up V_i so that $V_i = V$ for $0 < i < A$ and $B < i < N$, while $V_i = V'$ for $A < i < B$. This will allow us to describe a weak link with a non-zero critical temperature.

For the (100) interface (between the $a - b$ planes of a high-T_c superconductor), the dependence of the order parameter is very similar to the s-wave case. Figure 4.37 shows the semi-log plot of the order parameter as a function of distance from the interface for different temperatures. Again, we can observe the exponential decay and define the leaking distance ξ. The dependence of the order parameter on temperature for different lengths of the weak link is shown in Figure 4.38 and the two manifestations of the proximity effect are seen. First at $T = 0$K the order parameter is modified if $L/2$ is of the order of the superconducting coherence length in the N′ layer. Secondly, above T_c' the order parameter decays with increasing temperature but has non-zero value even if $L/2$ is greater than the conventional leaking distance defined by the $T_c' = 0$K case. The self-consistently calculated leaking distance is shown in Figure 4.39. Similar to the s-wave case it diverges at T_c' and, for the same temperature, larger interactions in the weak superconductor will increase the leaking distance.

The coherent transport in the c-axis direction will be described by the hopping amplitude in the $\hat{z}$ direction, $t^{\perp} = 0.5t^{||}$. Figure 4.40 shows the Josephson critical current as a function of temperature for different lengths of the weak superconducting layer. The general behavior is similar to the one of the s-wave junction. The d-wave order parameter has no k_z dependence, and thus in the $\hat{z}$ direction it is an effective on-site order parameter.

For short weak links the current does not vanish abruptly above T_c' but rather has a smooth dependence on temperature. This dependence on temperature above T_c' shows that the length of the weak link is comparable to the leaking distance in this layer.

The increase of the leaking distance due to the finite T_c' cannot explain by itself the observed "giant proximity effect". It is only the conjunction with the presence of disordered pockets of superconductivity in the weak link that makes this effect possible. The calculation of the Josephson current in the presence of the disordered pockets from the previous section stands also for the c-axis geometry. The extra dimension will only affect the necessary volume of superconductivity needed to observe a "giant proximity effect". The presence of pockets of strong superconductivity in the middle layer will further decrease the effective size of the Josephson junction. The dependence on the length of the junction is not exponential any more. The Josephson critical current will be non-zero above T_c' for much longer junctions. These results form the basis for a qualitative understanding of the giant proximity effect observed by Bozovic et al [109].

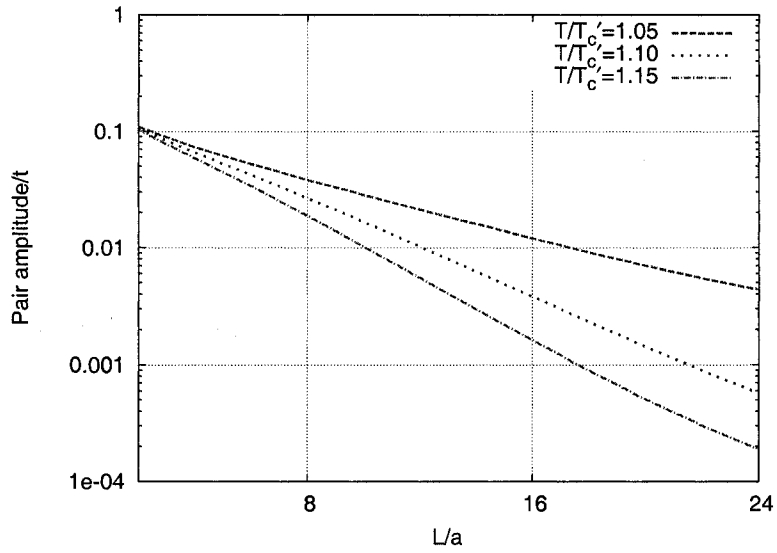

Figure 4.37: D-wave order parameter at L/2 as a function L for different temperatures - 100 d-wave case with $V = -4t$ and $V' = -2t$.

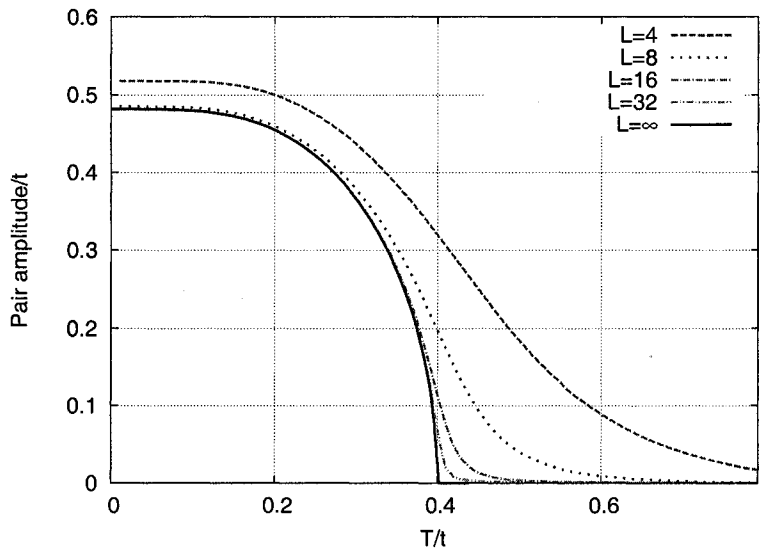

Figure 4.38: D-wave order parameter at L/2 as a function of T for different lengths - 100 d-wave case with $V = -4t$ and $V' = -2t$.

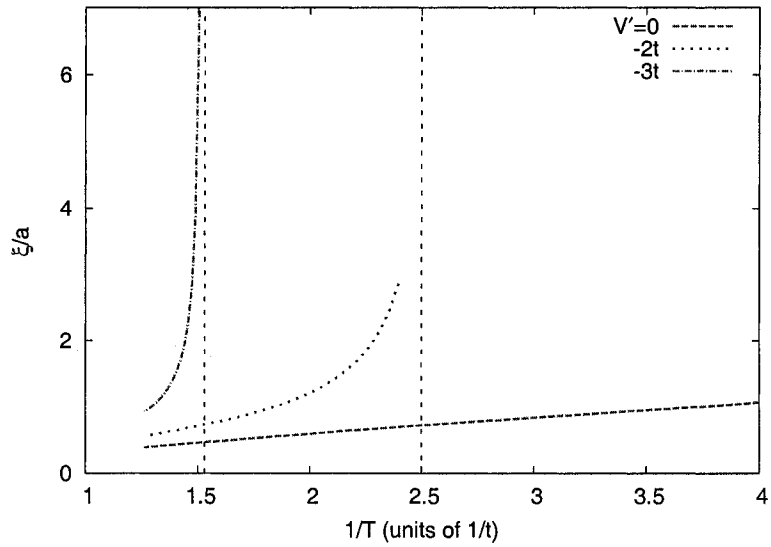

Figure 4.39: Leaking distance as a function of inverse temperature for different interaction strengths - 100 d-wave case with $V = -4t$. The vertical dashed lines represent the inverse of the critical temperatures for the corresponding V' parameters: $T_c(V' = -2t) = 0.4t$, $T_c(V' = -3t) = 0.67t$.

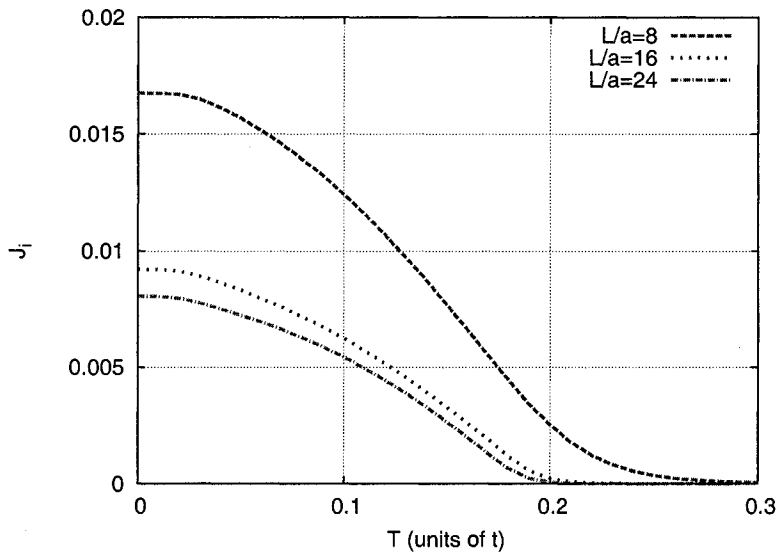

Figure 4.40: The c-axis dc Josephson current in the middle layer as a function of temperature for different lengths L of the weak link for which $V = -4t$ and $V' = -2t$. The c-axis hopping amplitude is $t^{\perp} = 0.5t^{||}$.

4.3 Andreev States

Andreev reflection occurs at the interface between a normal metal and a superconductor [124]. When an electron moving in a normal metal encounters an interface with a superconductor (Figure 4.41), it will be retro-reflected as a hole if its energy is less than the superconducting gap as there are no single particle states below the gap in the superconducting state. The net current will be in the direction of the initial electron. Two electrons will enter the superconductor as a Cooper pair.

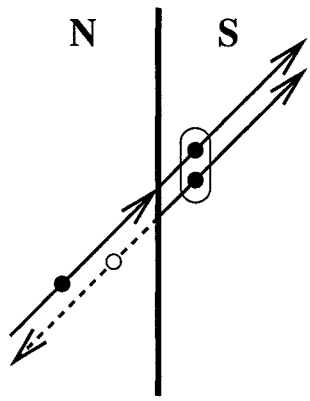

Figure 4.41: Andreev reflection at the N/S interface

It is known that the existence of an inhomogeneous distribution of order parameters will lead to the formation of bound states. This phenomenon is similar to the bound states formed by a potential well, but in this case with boundary conditions that depend on the energy and momentum of the incoming electrons. These bound states have been found theoretically first in normal metal thin films deposited on superconducting slabs [125], then in vortex cores [126] and superconductor-normal metal-superconductor (SNS) thin film structures [127]. More recently the formation of bound states involving d-wave superconductors, either in vortex cores, thin film structures or even as surface states, was investigated [20, 96, 114–116, 118].

Experimentally the existence of the Andreev bound states (ABS) can be observed mainly through transport methods. Directly, these states can be observed with Scanning Tunneling Microscopy (STM), or Josephson junction experiments. In some special cases the energy of the ABS is zero, and they are called Zero Energy States (ZES). The ZES are observed either localized near surfaces, such as the (110) interface of d-wave superconductors [92, 93, 128], near impurities [44] or inside vortex cores [129].

The main effect of the Andreev reflection is the one on transport properties. For conventional s-wave superconductors, Blonder, Tinkham and Klapwijk (BTK) [130] have shown that the conductance spectrum below the gap depends on the transparency of the

N/S interface. For high transparency interfaces, the main process for electrons with energy less than the superconducting gap is the Andreev reflection. As BTK demonstrate, the conductance in this scenario is greatly increased. As the transparency decreases, the reflection at the N/S interface is more and more specular, and the conductance for energies below the gap decreases. For very low transparency interfaces, considered as the tunneling limit, the derivative of the I/V curves will give the superconducting density of states.

For d-wave superconductors, because of the momentum dependent order parameter, the BTK formalism should be slightly modified. Interfaces with various orientations will have different properties mainly because electrons with various momenta impinging on the interface will interact with pairing potentials that have different phases. For the $d_{x^2-y^2}$ symmetry and a (110) interface, electrons travelling in the $\hat{x}$ direction will interact with a positive pair potential, while the electrons travelling in the $\hat{y}$ direction will interact with a negative pair potential.

For a 1D N/(s-wave) SC system, we present in Appendix D the analytical solution of the continuous version of the BdG equations [125, 131]. The main result is the quantization of the electron energy and the localization of these states in the normal metal. The quantization condition is given by:

$$\frac{2L}{\xi_0}\frac{E}{\Delta} = n\pi + \arccos\frac{E}{\Delta} \tag{4.5}$$

where E is the energy of the electron, L is the length of the normal metal region, Δ is the order parameter in the superconductor and $\xi_0 = \hbar v_f/\Delta$ is the superconducting coherence length. For lengths of the normal metal region on the order of the coherence length, there will be only one Andreev level. The energy of this level is pushed towards the gap value for very small lengths. As L increases, Figure D.2 shows that the number of level increases proportionally with L and Δ:

$$n_l = \lceil \frac{2L}{\xi_0 \pi} \rceil. \tag{4.6}$$

Using both the planar interface methods and the recursion method, presented in Chapter 3, we will investigate the formation of the Andreev levels for different orientations of the interfaces and symmetries of the order parameter. Finite size systems will be also considered.

4.3.1 Planar normal metal/s-wave and normal metal/d-wave systems

Planar interfaces between normal metals and superconductors are usually investigated in experimental setups like the Josephson junctions and the planar tunneling spectroscopy

experiments. As previously shown, due to the Andreev reflection at the normal-metal / superconductor (N/S) interface and to the localization of states with energies lower than the superconducting gap, the subgap structure of the density of states is expected to have interesting properties. We will investigate N/S bilayers and S/N/S trilayers with different lattice orientations, for both d-wave and s-wave superconductors.

The (100) surface

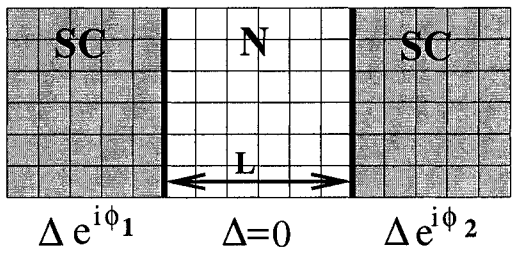

Figure 4.42: The S/N/S trilayer in the (100) orientation

The simplest surface geometry is the (100) surface, which has the a axis normal to the surface. The numerical method applied for this geometry is presented in Chapter 3.2.1. For an s-wave/normal metal/s-wave trilayer, we consider the setup presented in Figure 4.42 by setting the pairing potentials $U_i = -|U|$, $V_{ij} = 0$ if i and j are on the superconducting side and $U_i = 0$, $V_{ij} = 0$ if i and j are on the normal metal side. Self-consistent calculations will give the order parameter profile for the trilayer system.

Usually the analytical solution to the Andreev bound states problem is based on hard boundary conditions (the order parameter is considered to be a step function). This is a very good approximation in a situation in which the superconducting coherence length is small, and the suppression of the order parameter at the interface is over a small distance. Figure 4.43 shows the self-consistent order parameter profile for an s-wave/normal metal/s-wave trilayer. As expected, at the N/S interface, the order parameter is suppressed and vanishes in the normal metal. For the considered pairing potential $U = -2t$, soft boundary conditions differ from the hard boundary conditions over the coherence length (approximately 10 lattice sites), due to the proximity effect. Electrons with energies near the gap value will see a longer normal metal layer in the case of the soft boundary conditions. It is only for energies near the gap, the local density of states will be modified. This is shown in Figure 4.44, where we plot the local density of states calculated both for a self-consistent order parameter profile and for a step-like profile.

For the 1D case (Appendix D), the energies are quantized. Adding an extra dimension, parallel to the surface, there will be a continuum of available states. For each incident angle on the surface, there will be a set of quantized energies. The local density of states for the planar junction will have peaks at energies related to the 1D quantized

energies. The number of peaks can be obtained from the quantization condition for an incident angle $\theta = 0$. Eq. (4.5) and Eq. (4.6) will give the number of Andreev states as a function of the superconducting coherence length and of the length of the normal metal layer. Figure 4.45 shows the subgap LDOS in the normal metal layer as a function of the middle layer length. For lengths L comparable to the coherence length there is a small number of Andreev states, while as L increases there is a large number of states and eventually the LDOS will recover its normal state shape, the tight-binding LDOS in 2D. Plotting the LDOS for the same L but for different values of the order parameter Δ in Figure 4.46, the same behavior is observed. Due to the low number of states in the direction perpendicular to the surface (L is on the order of 40 lattice spacings), the LDOS will show peaks hinting to the finite size nature of the calculation. Some of these peaks can be smoothed out by using a large number of $k^{||}$ points; typically we use up to 1000 points in the direction parallel to the surface. Another solution would be to increase L and decrease U so that the number of Andreev states is constant. This is usually not realizable because the BdG is getting exponentially harder to converge as $U \rightarrow 0$.

Two extra questions could be envisioned when solving the Andreev states problem. First, what is the energy and the number of the Andreev bound states formed in the normal metal layer, when the two external superconductors acquire different phases? This scenario can be modeled with the use of the BdG equations. To the self-consistent calculation of the order parameter we add one more step in which the phases of the outside superconductors are fixed to desired values. It is only in the middle layer where the phase is allowed to converge self-consistently. The method is similar to the one used for calculating the Josephson current through a weak link. Figure 4.47 shows the subgap LDOS for different phase differences between the two outside superconductors. An interesting situation appears when $\Delta\phi = \pi$. As shown before [20, 96], for a d-wave superconductor at the (110) surface, consecutive Andreev reflections with order parameters having a phase shift of π will give rise to zero energy Andreev bound states. This is also true for two s-wave superconductors phase shifted by π. As the phase shift decreases, the location of the first Andreev level increases monotonically towards the value obtained for $\Delta\phi = 0$. The second Andreev level splits and as $\Delta\phi$ decreases it moves towards the first level and eventually join for $\Delta\phi = 0$.

The second problem, which is also addressed by the BTK formalism, is the influence of interface transparency on the conductance and on the formation of the Andreev bound states. A variable transparency of the interface is easily modeled with the use of the BdG equations. The hopping at the interface t' can be made a parameter in the problem. Self-consistent calculations of the order parameter and of the LDOS are performed for various values of the transparency. The results are shown in Figure 4.48. In addition to Andreev reflection, the probability of specular reflection increases as the interface transparency decreases. For a transparent barrier $t' = t$, the electrons with energy less than the order parameter will be confined in the normal metal region. As the transparency decreases we observe a disappearance of the Andreev peaks in the LDOS.

For very low interface transparency $t' = 0.2t$, the LDOS in the normal metal region is similar to that of an isolated metal of size L. As the probability of Andreev reflection decreases, the amplitude of the quasiparticle interference in the normal metal also decreases.

The d-wave/normal metal/d-wave trilayer in the (100) interface has the same general properties. As shown in Figure 4.49 for a choice of parameters $L = 10a$ and $\Delta_d = 0.4t$, there will be two Andreev levels. The top figure shows the LDOS for a site in the normal metal layer, while the bottom figure shows the LDOS for a site in the superconductor, close to the interface. In the (100) geometry the d-wave scenario is similar to the s-wave one. An electron impinging on the N/d-wave interface will feel an order parameter with the same sign, even if the incident angle changes sign. This will lead to a similar Andreev level formation as the s-wave case. Subtler differences will appear because electrons moving in the nodal directions will not be Andreev reflected, due to the fact that the order parameter is zero in the nodal direction. Electrons moving in other directions will feel different strengths of the order parameter.

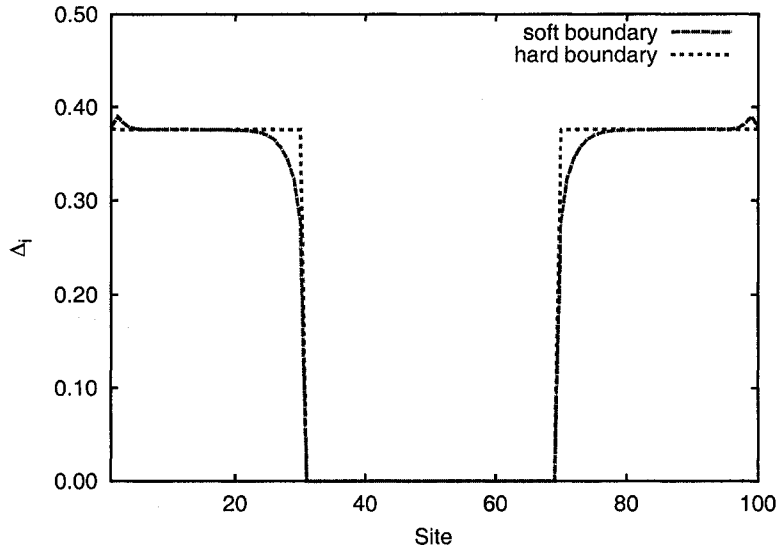

Figure 4.43: Order parameter profile for an s-wave/N/s-wave trilayer, $L = 40a$, $U = -2t$

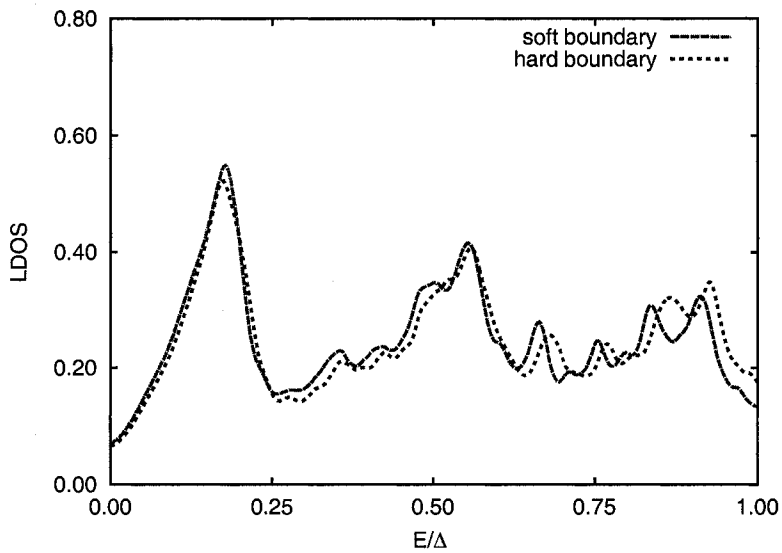

Figure 4.44: LDOS for soft and hard boundary conditions, $L = 40a$, $U = -2t$

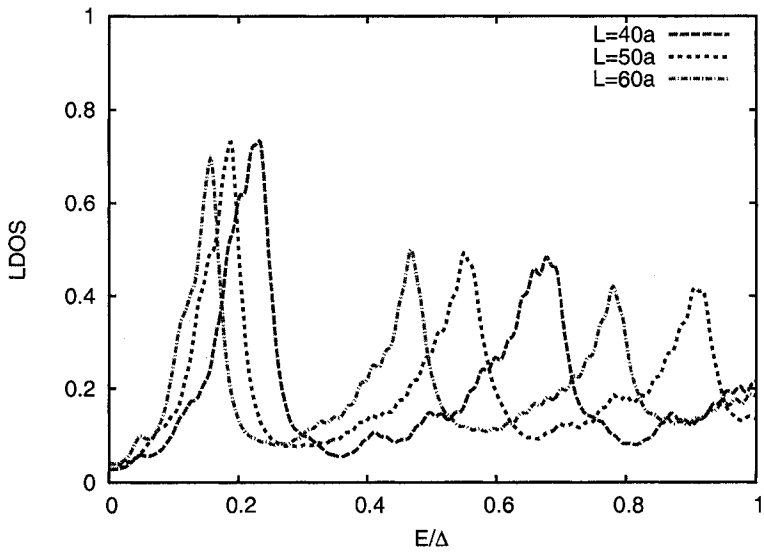

Figure 4.45: Andreev bound states for the s-wave/N/s-wave (100) geometry with $\Delta_s = 0.3t$, for different lengths L

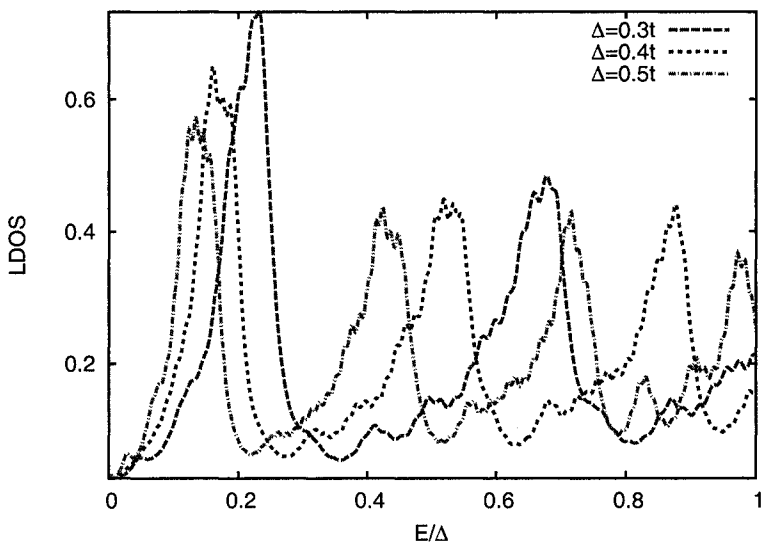

Figure 4.46: Andreev bound states for the s-wave/N/s-wave (100) geometry for $L = 40a$, for different order parameter values Δ_s

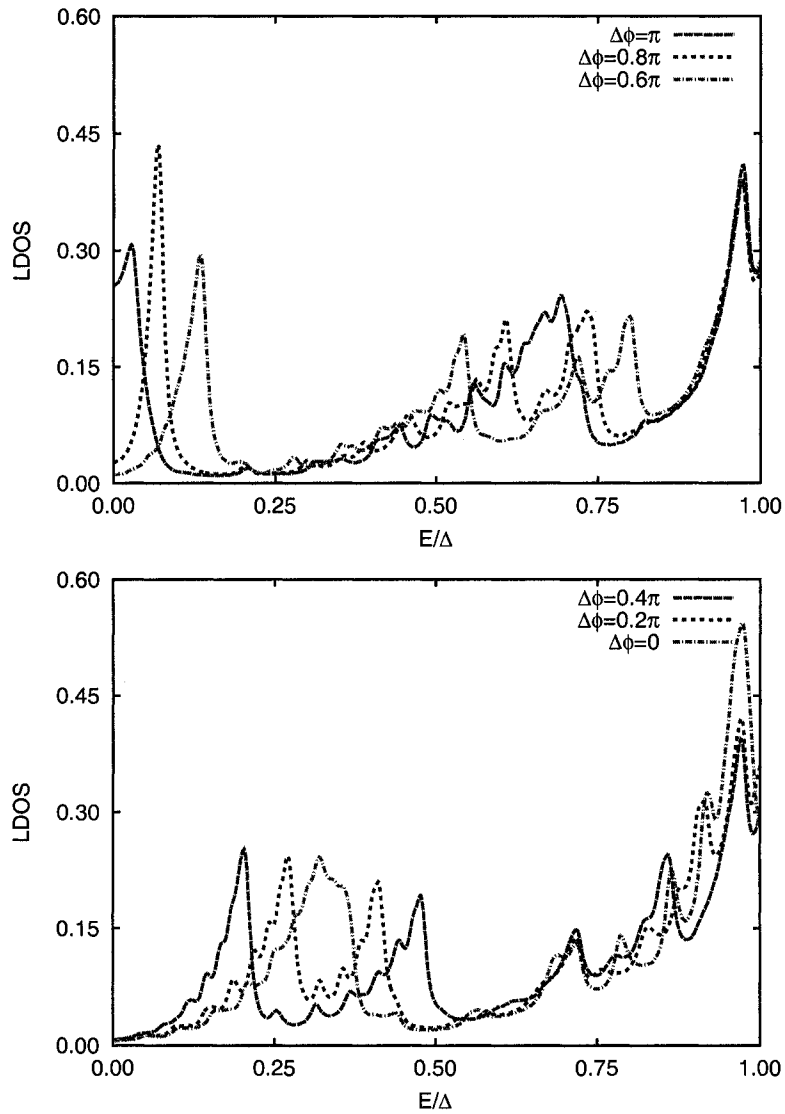

Figure 4.47: Andreev bound states for the (100) geometry and s-wave superconductors, as a function of phase difference $\Delta\phi$, for $L = 20a$ and $U = -2t$.

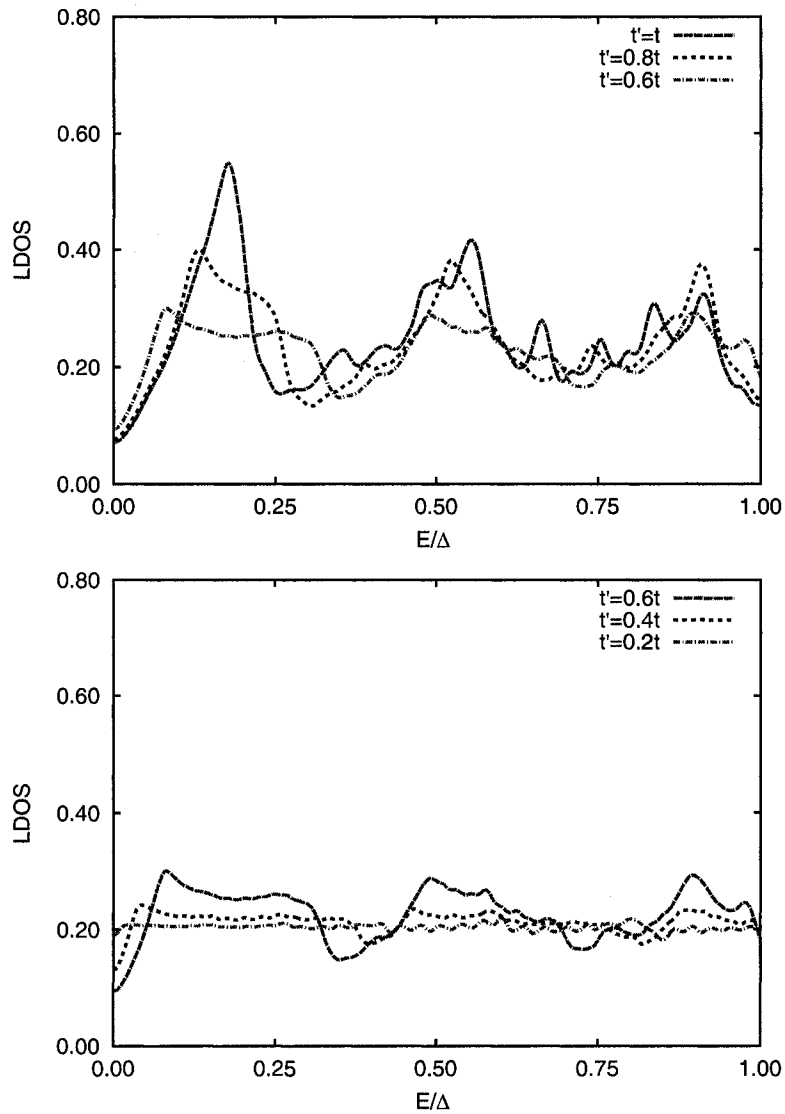

Figure 4.48: Andreev bound states for the (100) geometry and s-wave superconductors, as a function of interface transparency, for $L = 40a$ and $U = -2t$.

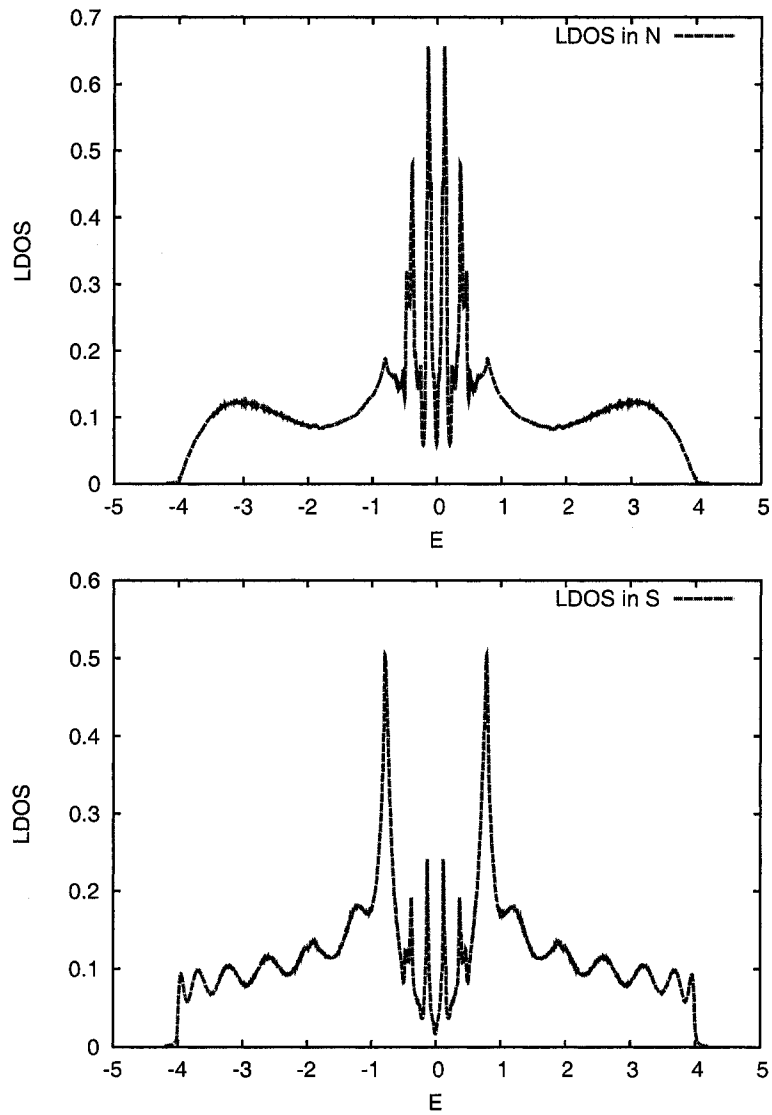

Figure 4.49: Andreev bound states for the d-wave/N/d-wave (100) geometry for $L = 10a$, and $\Delta = 0.4t$

The (110) surface

Different behavior of the LDOS for the (110) interface as compared to the (100) interface arises only for d-wave superconductors. The order parameter, having a $d_{x^2-y^2}$ symmetry, will have the nodes perpendicular to the surface. An incoming electron with an incident angle θ will scatter on an order parameter $\Delta(\theta)$ while an electron with incident angle $-\theta$ will scatter on an order parameter $-\Delta(\theta)$.

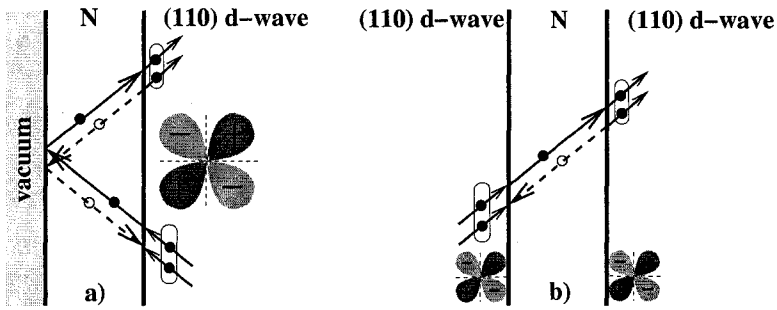

Figure 4.50: Andreev reflection at the (110) for the N/d-wave interface and the d-wave/N/d-wave trilayer

Figure 4.50a shows the Andreev reflection in the vacuum/normal metal/d-wave superconductor (N/D) configuration. An electron incident on the superconducting interface will be reflected back as a hole while a Cooper pair enters the superconductor. The hole has then a specular reflection on the interface with the vacuum. This will switch the sign of the momentum perpendicular to the surface and the new incident angle is opposite in sign as compared to the initial one. The hole will feel a reverse sign order parameter at the normal metal/d-wave interface. Again at the superconducting interface an Andreev reflection occurs, an electron will be reflected back and a Cooper pair exits the superconductor. A net current parallel to the surface is generated in this manner. Because the two consecutive Andreev reflections occur at surfaces with order parameters having opposite sign (or a phase shift of π), similar to the result for two s-wave phase shifted order parameters, a midgap Andreev level with zero energy will appear in the normal metal region. If the length of the normal metal is increased, additional levels with energies lower than the superconducting gap will form. The limit of $L \rightarrow 0$ will allow only one Andreev level, the zero energy state. This is in concordance with the observed zero energy state at the (110) surface of a d-wave superconductor.

We solve the BdG equations for the (110) surface using the infinite surface method presented in Chapter 3. The inhomogeneous N/D interface configuration can be easily setup by setting $V_{ij} = 0$ in the normal metal region and $V_{ij} = -V$ in the superconductor. The order parameter is obtained self-consistently and with the use of the eigenvectors and of the eigenvalues we calculate the local density of states for any location in the

system.

The first problem we wish to address is whether the zero bias conductance peak still survives as we increase the length of the normal metal from 0 to a large value L. Figure 4.52 shows the LDOS at the surface of the normal metal layer for different lengths of this layer. The zero energy state is robust for a wide range of thicknesses of the normal region. In addition to the zero energy Andreev state, additional states appear at finite energies. The number of bound states is related to the thickness of the normal region in a similar manner as shown by Eq. (4.5). Paths incident at a finite angle θ will have different lengths, thus the energy of the Andreev state is shifted. As seen before, if the angular dependence is integrated out, the spectrum becomes continuous, but has peaks around the energies obtained for $\theta = 0$. In the (110) geometry, all incident angles will generate zero energy states, thus the height of the ZBCP is maximal. If the node lines of the order parameter are tilted with respect to the surface, only a finite range of incident angles will generate zero energy states. This scenario is not possible for tight binding methods because only a discrete choice of tilted angles is available. For example one could model the $(nm0)$ surfaces, where n and m are integers, and obtain different angles between the node line and the surface [132].

Figure 4.53 show the LDOS at the surface of the normal metal for $\mu = -t$. Different lengths of the normal metal layer are also considered. For $L = 0$ the induced imaginary s-wave component will split the ZBCP. As L increases to a finite value, we observe that although the ZBCP remains, the splitting drops very rapidly. This happens already for $L = a\sqrt{2}/2$, for which in addition to the formation of two new peaks at the gap edge, we observe that the splitting of the ZBCP disappears. For $L = 3a\sqrt{2}/2$ the splitting is gone altogether and the second Andreev level moves towards smaller energies as expected from the length dependence of the Andreev states. This result shows that induction of an imaginary s-wave component at the surface is very weak when adding a normal layer on top of the d-wave superconductor.

The dependence of the LDOS on the distance from the surface is presented in Figure 4.54 for a site of type A and in Figure 4.55 for a site of type B. The difference in the LDOS for the two types comes from the different local environments and the number of nearest neighbors at the surface. At half filling a ZBCP is observed throughout the normal metal layer. For sites of type A, the ZBCP penetrates in the superconductor, but decays exponentially on the order of the coherence length (see Appendix D). For the B-type sites, the ZBCP is not observed inside the superconductor. The Andreev levels with finite energy observed for both A and B type sites are decaying exponentially in the superconductor. The LDOS as a function of distance from the interface for $\mu = -t$ is shown in Figure 4.56 for A-type sites and in Figure 4.57 for B-type sites. The subgap structure is now similar for both types, and we observe that the splitting of the ZBCP is recovered near the N/D interface. There is a dependence of the splitting with respect to the distance from the interface, mainly because of the proximity effect on the imaginary s-wave component.

For the d-wave/normal metal/d-wave (D/N/D) trilayer (Figure 4.50b), the Andreev reflection provides a way for the supercurrent to travel across the normal metal layer. As the order parameters felt by the electron at the two interfaces have the same phase, there will be no zero energy states forming. A quasiclassical electron will travel only on a straight line between two points on the two interfaces as shown in Figure 4.41b. The reasoning used for the S/N/S interfaces can be applied here; paths with various angles have different lengths and thus the Andreev levels will be continuous. Integrating out all the possible paths will give the peaks at energies close to the 1D quantized ones. The first Andreev level will have finite energy and the number of levels is given by the ratio L/ξ_0. This behavior is seen in Figure 4.58, where we plot the LDOS at the half-way between the two interfaces for $L = 5a$ and $L = 13a$, where L is the distance between the two interfaces.

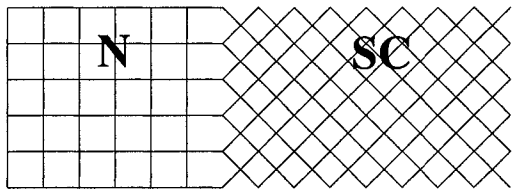

Figure 4.51: Andreev reflection at the (100) N / (110) d-wave SC interface

One might ask if the orientation of the normal metal lattice is important in the formation of the zero energy state. In order to answer this question we form an interface of a (100) oriented normal metal layer with a (110) oriented d-wave superconductor. The numerical calculation can be easily done with the use of the recursion method. The definition of the lattices is contained in the definition of the nearest-neighbors of each site (Figure 4.51). We present the result for two lengths of the normal metal in Figure 4.59. LDOS for a site at the surface of the normal metal is plotted for $L = 10a$ and $L = 16a$. For both cases we observe zero energy states forming. Also additional Andreev states with finite energies can be observed, with the known length dependence. The presence of the ZBCP even in this geometry, shows that the underlying symmetry of the normal metal lattice is not important in the formation of the zero energy states. As long as we have specular reflection at the vacuum/normal metal interface, zero energy states will always form if the node line of the superconductor is perpendicular to the surface. The details of the lattice might only contribute to the width and height of the ZBCP.

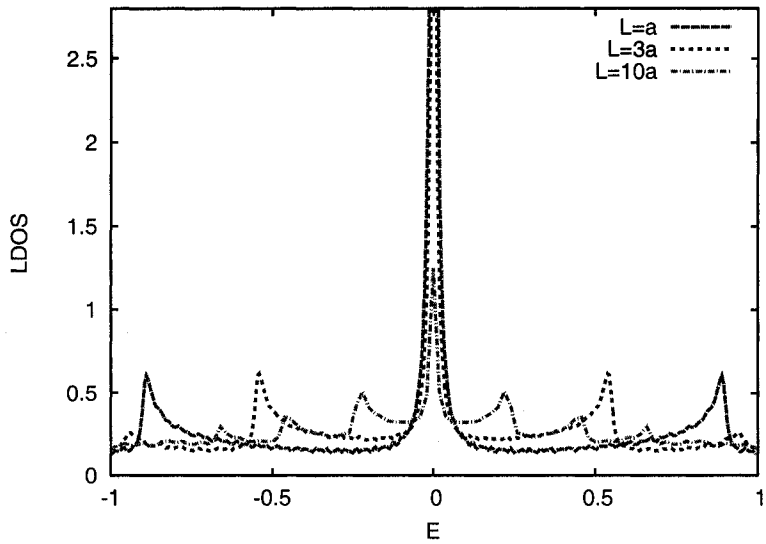

Figure 4.52: LDOS for the N/D (110) geometry for different lengths of the normal metal layer; $V = -2.5t$ and $\mu = 0$

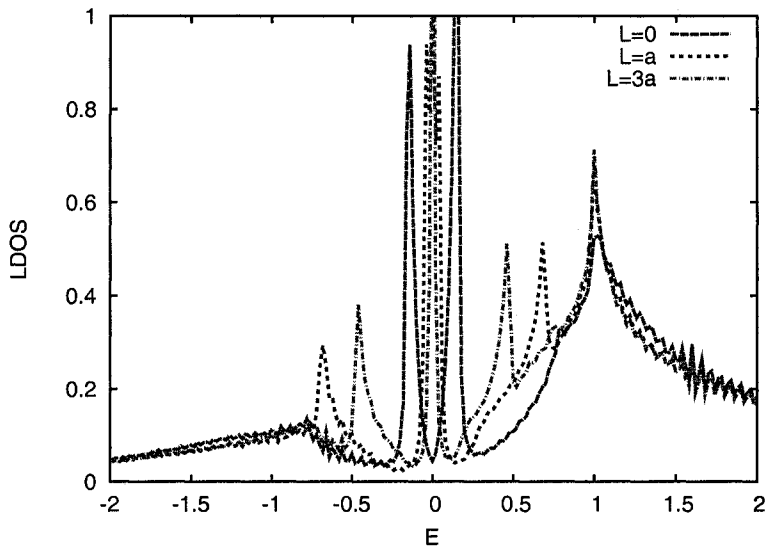

Figure 4.53: LDOS for the N/D (110) geometry for different lengths of the normal metal layer; $V = -2.5t$ and $\mu = -t$

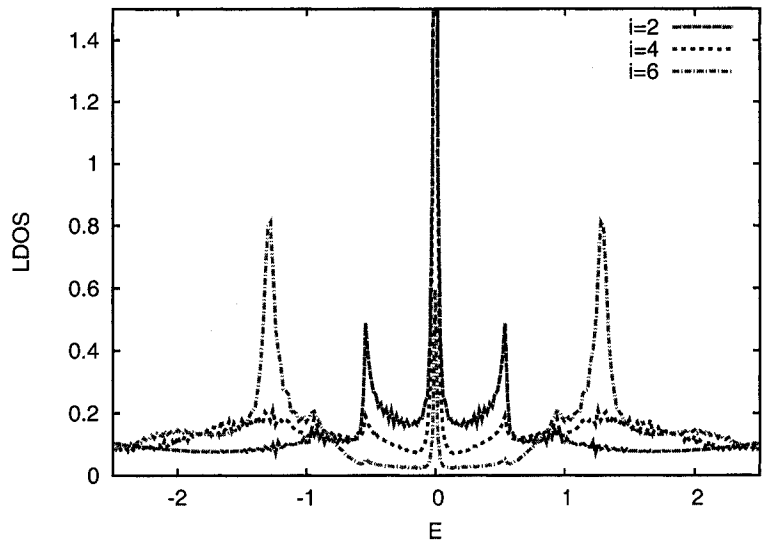

Figure 4.54: LDOS for the N/D (110) geometry at different locations for sites of type A; $L = a$, $V = -2.5t$ and $\mu = 0$

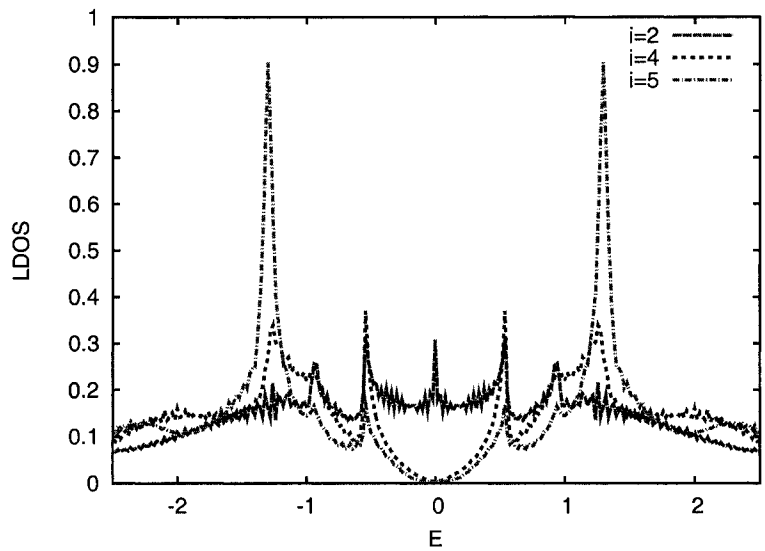

Figure 4.55: LDOS for the N/D (110) geometry at different locations for sites of type B; $L = a$, $V = -2.5t$ and $\mu = 0$

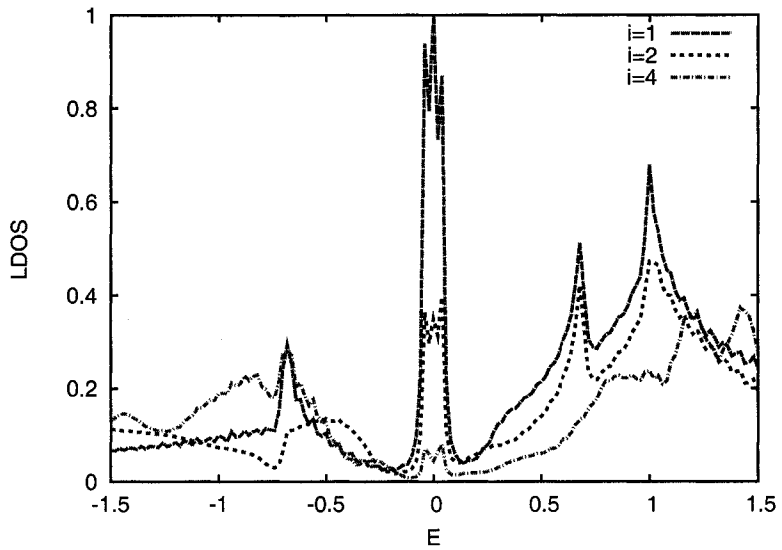

Figure 4.56: LDOS for the N/D (110) geometry at different locations for sites of type A; $L = a$, $V = -2.5t$ and $\mu = -t$

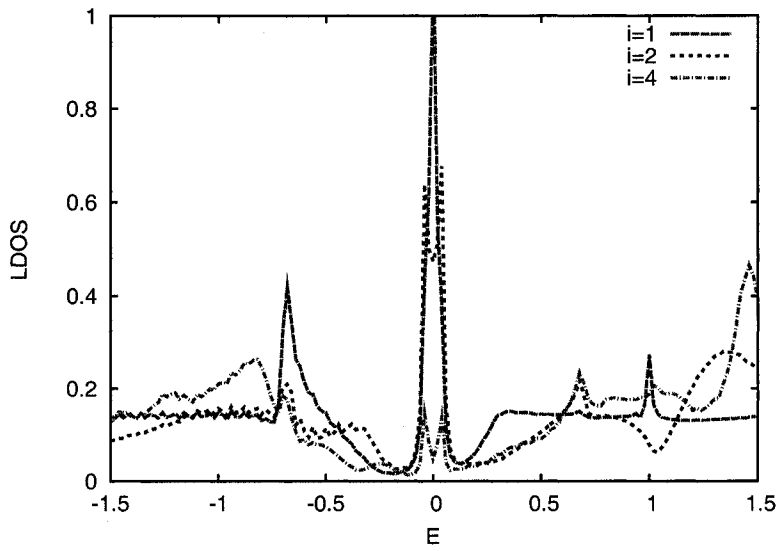

Figure 4.57: LDOS for the N/D (110) geometry at different locations for sites of type B; $L = a$, $V = -2.5t$ and $\mu = -t$

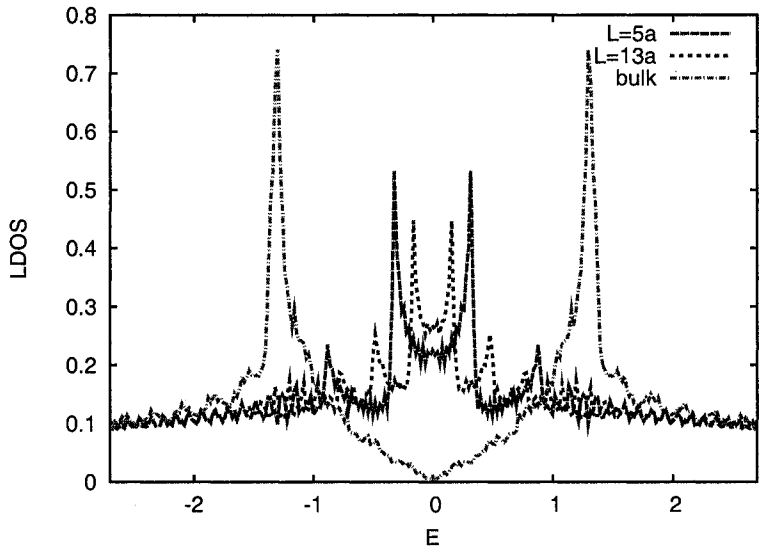

Figure 4.58: LDOS at L/2 for the (110) d-wave/N/d-wave (110) geometry for different lengths of the normal metal region; $V = -2.5t$ and $\mu = 0$

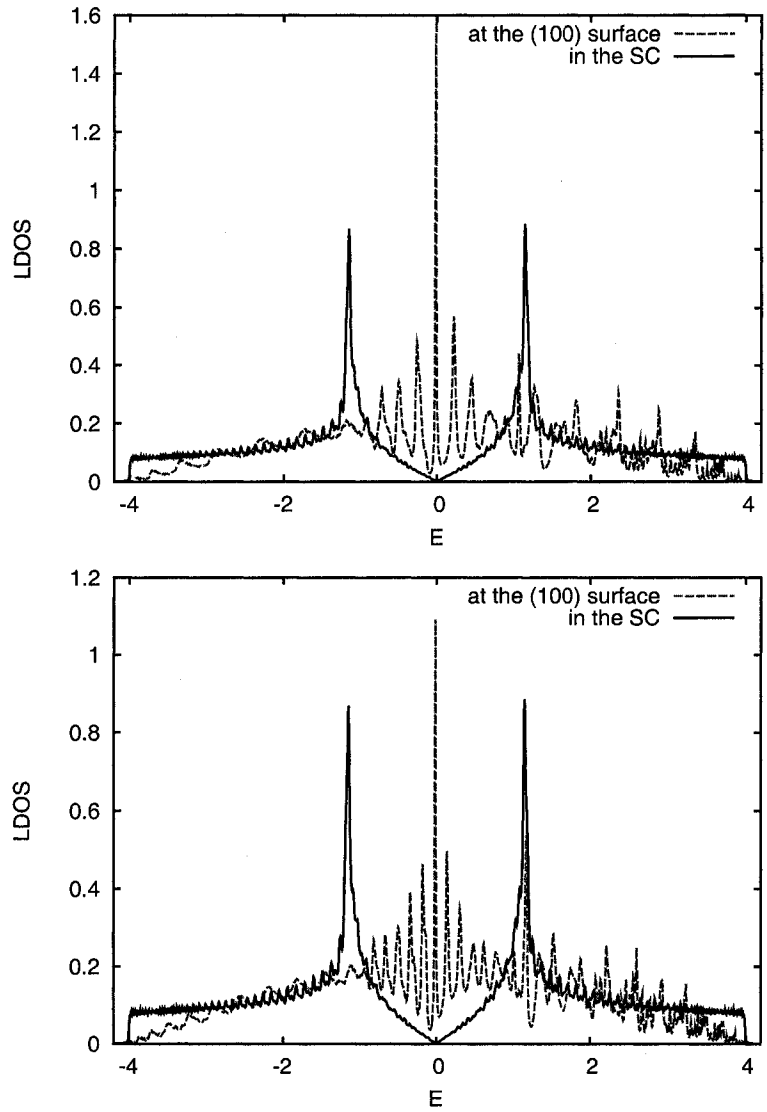

Figure 4.59: Andreev bound states for the vacuum/(100) normal metal/ (110) d-wave SC tryilayer for $\Delta = 0.4t$ and a) $L = 10a$, b) $L = 16a$

4.3.2 Bound states in finite size systems

Mesoscopic and nanoscale devices gain more and more interest nowadays. Small nanoscale structures can be easily built by electron beam lithography. Such structures can be made to contain normal metal/superconductor interfaces, or embedded regions of normal metal into a superconductor. In a recent experiment [133], the authors fabricate mesoscopic Au structures embedded in Nb. Upon cooling the Nb regions become superconducting, while the Au ones remain of normal metal type. STM measurements of the dI/dV spectrum shows sub -gap structure near the normal metal/superconductor interface. These features in the local density of states observed at energies less than the superconducting gap, are the energies of the Andreev states. The authors also observe that the energies of these Andreev levels depend on the location where the STM spectra is measured. As the formation of the Andreev states is an interference phenomenon, we are interested in calculating the local density of states for a finite size normal metal region embedded in a superconductor. The presence of different types of interfaces intersecting at various angles is expected to give non-trivial results for the LDOS. In the quasiclassical approximation, these types of problems are usually called Andreev billiards; besides the usual specular reflection, the Andreev reflection also plays a role in the motion of the particle [134–140].

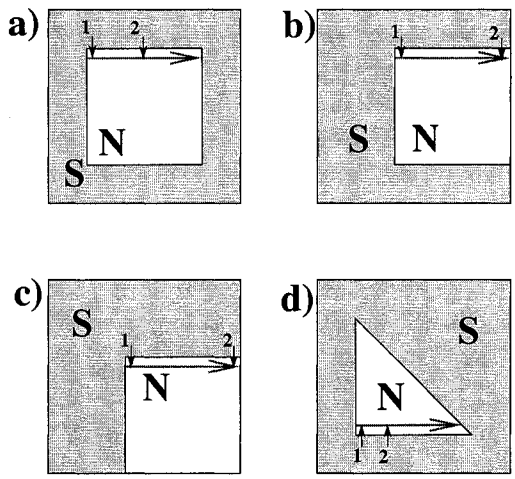

Figure 4.60: Finite size normal metal samples, embedded in a s-wave superconductor. Considered configurations are (a) a square with 4 N/S interfaces,(b) a square with 3 N/S and 1 N/vacuum interfaces, (c) a square with 2 N/S and 2 N/vacuum interfaces and (d) a triangle with 3 N/S interfaces

Using the recursion method presented earlier, we investigate the formation of the Andreev states in a finite size sample. The geometries considered are presented in Figure 4.60. We first model a normal metal square with different numbers of normal-

metal/superconductor interfaces. For example, Figure 4.60a has four N/S interfaces, Figure 4.60b has three N/S interfaces and one vacuum/N (I/N) interface and Figure 4.60c has two N/S interfaces and two I/N interfaces. We also consider the formation of Andreev levels in a triangularly shaped sample as the one presended in Figure 4.60d which has the sides comprised of N/S interfaces. The systems considered in this calculation are clean systems described by ballistic paths. Because the formation of the Andreev levels is an interference phenomenon, the presence of impurities will broaden the energy of the Andreev states [131], thus making the experimental observation difficult.

A simplistic reasoning of how the Andreev states will form in such finite size system can be developed by considering the paths an electron can travel on inside the normal metal region. As shown in Figure 4.61, all the paths bounded by two normal metal/superconductor interfaces are in fact line segments because the electrons are retro-reflected at each interface. Using the 1D formulation of the Andreev levels, we can calculate the allowed energies, which are quantized. If we consider all the paths going through a specified location in the system, and integrate out the angle, θ, these paths make with an arbitrary axis, we can obtain in principle the LDOS for this location. The details of the LDOS will depend on where it is calculated, because the distribution of lengths $L(\theta)$ depends on the location of their intersection point. Thus, the LDOS near the corner will be different from the LDOS calculated in the center of the square. The shape of the system and the properties of the interfaces will define a unique LDOS map.

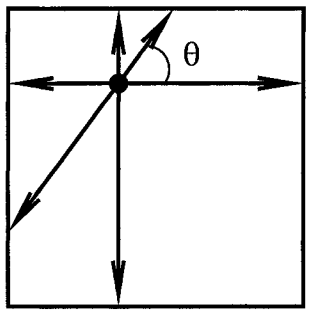

Figure 4.61: Paths in the normal metal defined by the Andreev reflection; all 4 sides are normal metal/superconductor interfaces

The energy and the number of the Andreev bound states will also depend on the size of the normal metal region and on the magnitude of the superconducting order parameter. The size of the investigated system is $80a \times 80a$, and has a normal metal region of size $60a \times 60a$ embedded in the center. Regions with different types are obtained by setting the values of the parameters U_i and V_{ij}, $U_i < 0$ or $V_{ij} < 0$ for the superconducting regions and $U_i = V_{ij} = 0$ for the normal metal regions.

First we consider the square system with 4 N/S interfaces with $L = 60a$ and an s-wave order parameter $\Delta = 0.3t$. In Figure 4.62 we show the LDOS along the arrow

defined in Figure 4.60a. The shape of the LDOS changes when moving along the defined arrow. Right at the corner the Andreev level seems to be located near the gap edge. The shape of the LDOS is dramatically changed from the planar interfaces case and the location of the peaks in the LDOS does not follow the same rule. Half-way between the two corners, the highest subgap density of states is obtained at low energies. In order to see the spatial map of the density of states as a function of energy, we plot in Figure 4.63 the LDOS map for two energies. At $E = 0.26\Delta$ the maximum LDOS is located near the sides of the square, while for $E = 0.5\Delta$ the localized states are near the corners. In both cases we observe a 4-fold symmetry of the LDOS map, in concordance with the symmetry of the system. The physical interpretation of these modes relies on the fact that the quasiparticles with energy less than the superconducting gap are confined in the normal metal region. Similar to an electron in a 2D box, the wavefunction of these modes depend on the energy. This spatial dependence of the LDOS could be directly seen in an STM experiment.

We investigate next the same square system but with 3 N/S interfaces and one I/N interface. The interface with the vacuum can be easily obtained if we redefine the nearest neighbors for the sites located at this interface. Figure 4.64 shows the LDOS for sites along the arrow defined in Figure 4.60b. Surprisingly, the LDOS near the corner is very similar to the one obtained previously for 4 N/S interfaces. In fact the previous LDOS could be obtained by superimposing the actual LDOS with a mirror image of it. At the location "2", near the opposite corner, the LDOS is similar to the planar case, with equally spaced peaks. The LDOS map for $E = 0.16\Delta$, shown in Figure 4.65, is somewhat homogeneous around the center of the sample and suppressed at the two corners defined by the intersection of the N/S interfaces. For $E = 0.5\Delta$, the LDOS map is similar to the one obtained for the 4 N/S case. The existence of these states at the corners, is not affected by the geometry of the entire system. For this case too, the symmetry of the wave function reflects the symmetry of the N/S surfaces. This symmetry is two fold with the symmetry axis perpendicular to the $\hat{y}$ direction.

The 2 N/S interfaces and 2 I/N interfaces case shows similar behavior. The LDOS along the defined line (Figure 4.60c) is almost identical to the one obtained in the 3 N/S + I/N case. This result is presented in Figure 4.66, and shows that the LDOS next to the interfaces is mostly influenced by the proximity to these interfaces. The LDOS map for this configuration is shown in Figure 4.67. The wave function of the Andreev states is now symmetric with respect to the diagonal intersecting the two N/S interfaces. The wave function of the state with energy $E = 0.16\Delta$ is somewhat spread throughout the metal, while $E = 0.5\Delta$ once again is attached to a state localized near the corner of the N/S interfaces.

We model different angles between the interfaces by using a triangular geometry of the normal metal region (Figure 4.60d). When calculating the LDOS along the $\hat{x}$ axis, near the N/S interface (Figure 4.68), we observe that near the corners the spectrum is changed. Near the corner with an angle of 90°, the LDOS is almost identical to the one

seen for all the square geometries. The spatial dependence of the LDOS could be once again obtained by superimposing the LDOS of the isolated corners. The LDOS map for this configuration (Figure 4.69) shows that states with lower energy are localized in the center, while states with higher energy are localized near the corners of the system.

Another interesting problem is the formation of Andreev levels in finite normal regions embedded in d-wave superconductors. In the case of a square with 4 N/d-wave interfaces, the order parameter on the $\hat{x}$ sides will have an reversed sign when compared to the order parameter on the $\hat{y}$ sides. This scenario is expected to show zero energy states for those paths that intersect both the $\hat{x}$ and the $\hat{y}$ sides of the square. We investigate such a system, with the use of the recursion method. We consider a normal metal region of size $40a \times 40a$ embedded in a d-wave superconductor by setting $V_{ij} = 0$ in the normal metal and $V_{ij} = V$ in the superconductor.

In Figure 4.70 we plot the LDOS as a function of energy for different locations in the system. The top graph shows the LDOS along the line defined previously and shown in Figure 4.60a, while the bottom one is taken along a diagonal line. Both graphs show a dependence of the Andreev peaks on the location in the normal metal, depending whether the spectra are taken near the corner or inside the square. There is a striking difference between the LDOS taken along the two lines. When moving along the diagonal one observes that a small peak forms at zero energy, while this it is not observed along the other line. This is a strong indication that some paths produce zero energy states and that they are somewhat localized in specific locations in the sample.

The localization of the Andreev states can be seen in Figure 4.71, where we plot the LDOS map for 4 different energies 0.0, 0.2Δ, 0.26Δ and 0.5Δ. The zero energy states are located along the diagonals but the density of those states is quite low. Increasing the energy to 0.2Δ we obtain a four-fold symmetric mode, localized near the center of the square. A drastic change in the spatial distribution of the Andreev levels is observed when increasing the energy to 0.26Δ. The Andreev states are now pushed towards the sides of the square. At higher energies, $E = 0.5\Delta$, the Andreev states are localized near the corners of the normal region.

We also consider the 3 N/d-wave + 1 I/N geometry, shown in Figure 4.60b. A two-fold symmetric LDOS map is obtained (Figure 4.72). The location of the zero energy states is mostly unchanged, although the LDOS for sites closer to the I/N is modified and slightly increases. The same behavior is observed for $E = 0.2\Delta$, the LDOS near the I/N interfaces becomes more homogeneous and is also increased. For higher energies, $E = 0.26\Delta$ and $E = 0.5\Delta$, some of the states observed in the 4 N/d-wave geometry disappear, namely the ones next to the I/N interface.

It is interesting to note that if we were to measure the LDOS at the I/N interface, we can still gather information about the whole system and infer about the magnitude of the superconducting order parameter and about the size of the embedded normal metal region. It is only in the energy range smaller than the superconducting gap that the normal state LDOS is modified when in proximity with a superconductor.

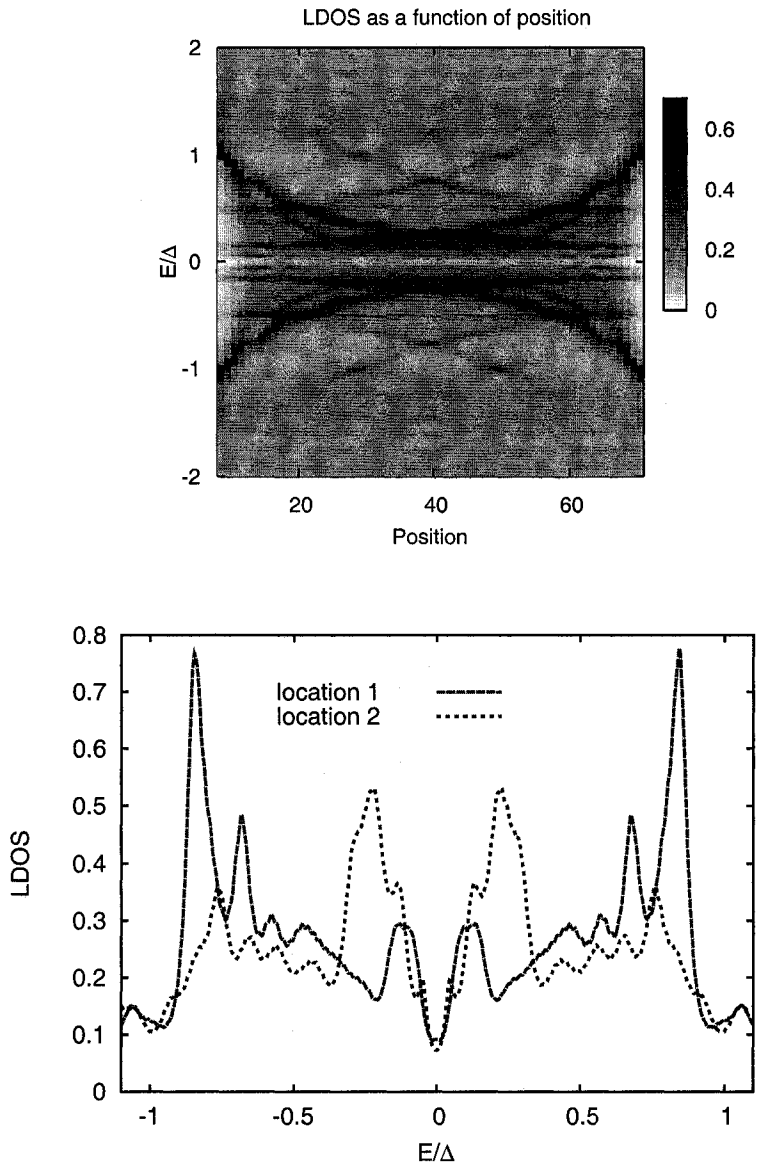

Figure 4.62: LDOS for a square with 4 N/S interfaces (taken along the arrow shown in Figure 4.60a), $\Delta = 0.3t$, $L = 60a$

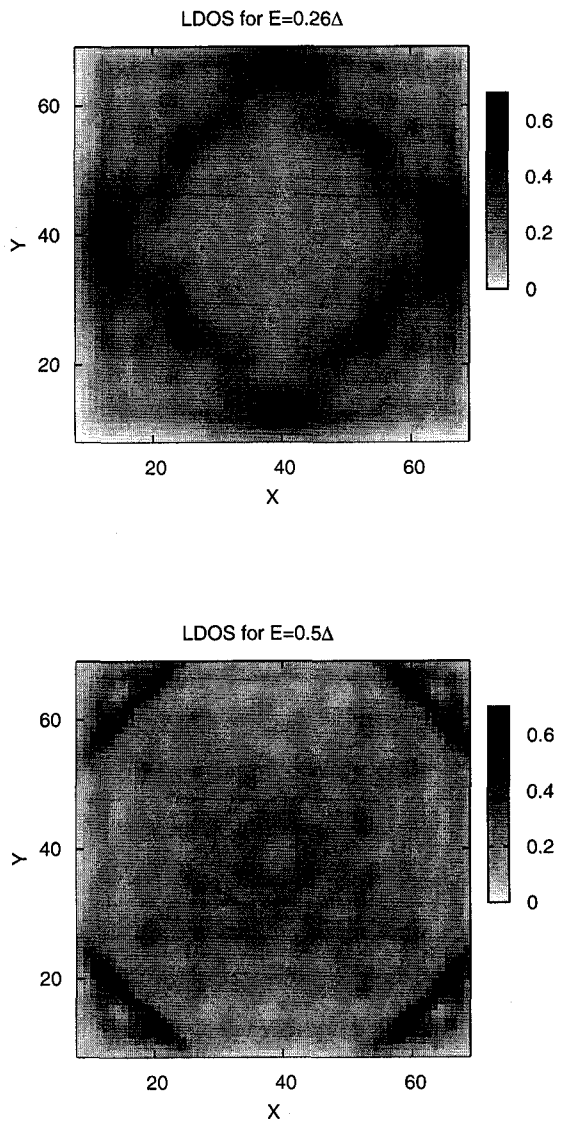

Figure 4.63: LDOS map for a square with 4 N/S interfaces, $\Delta = 0.3t$ and $L = 60a$

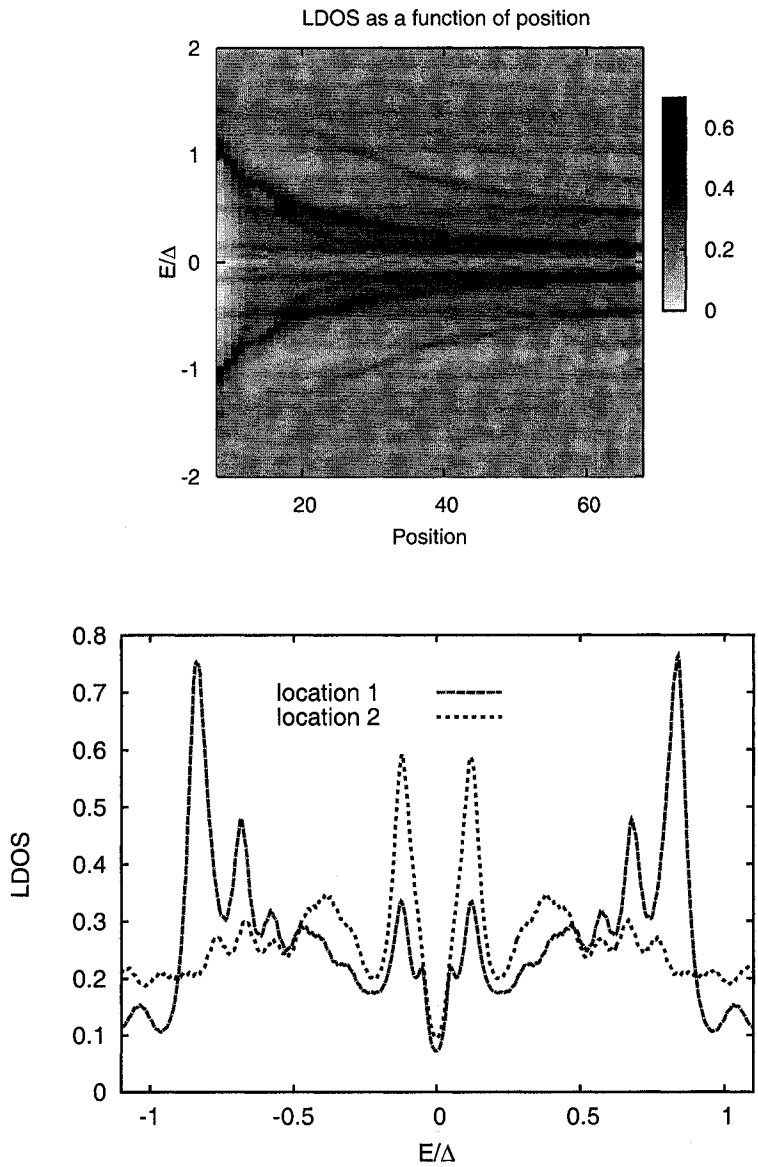

Figure 4.64: LDOS for a square with 3 N/S interfaces (taken along the arrow shown in Figure 4.60b), $\Delta = 0.3t$, $L = 60a$

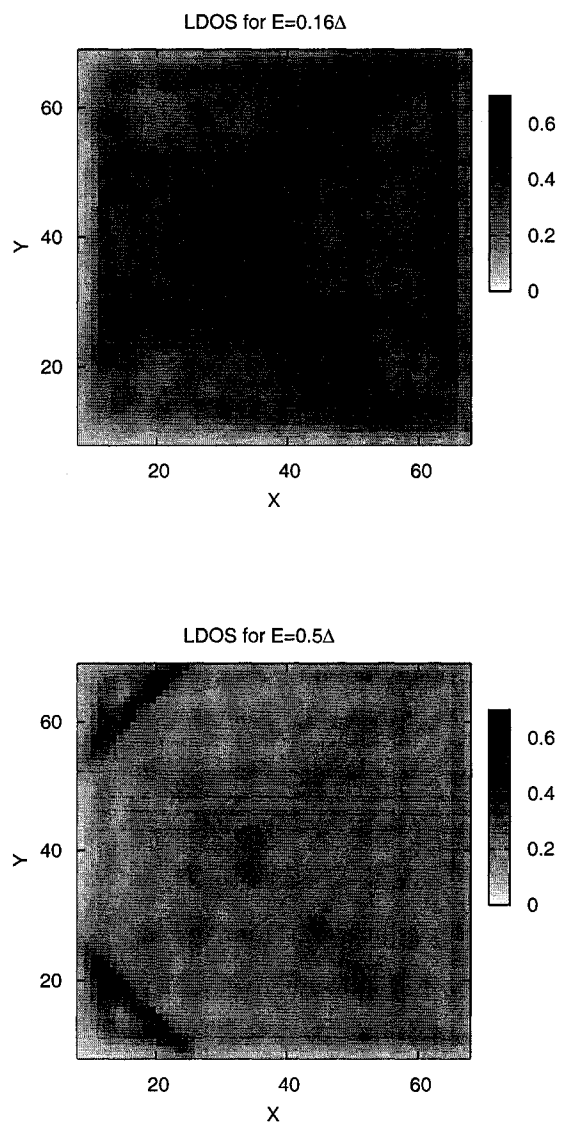

Figure 4.65: LDOS map for a square with 3 N/S interfaces, $\Delta = 0.3t$ and $L = 60a$

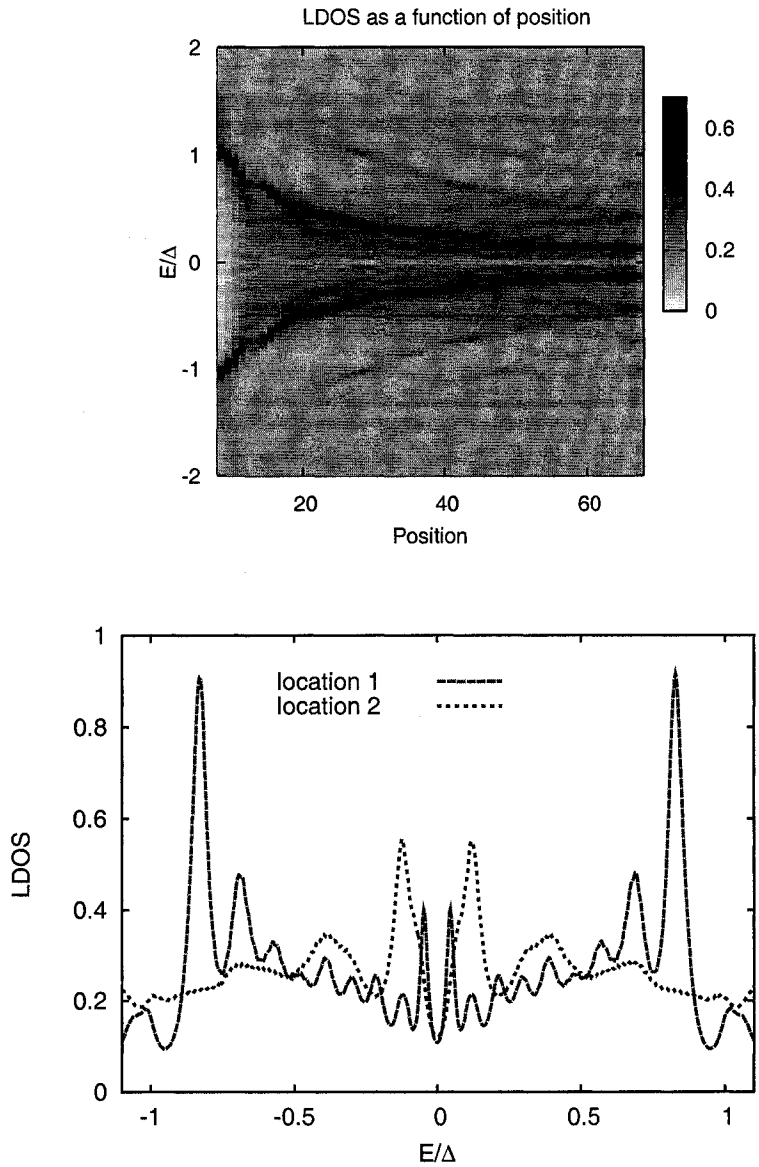

Figure 4.66: LDOS for a square with 2 N/S interfaces (taken along the arrow shown in Figure 4.60c), $\Delta = 0.3t$, $L = 60a$

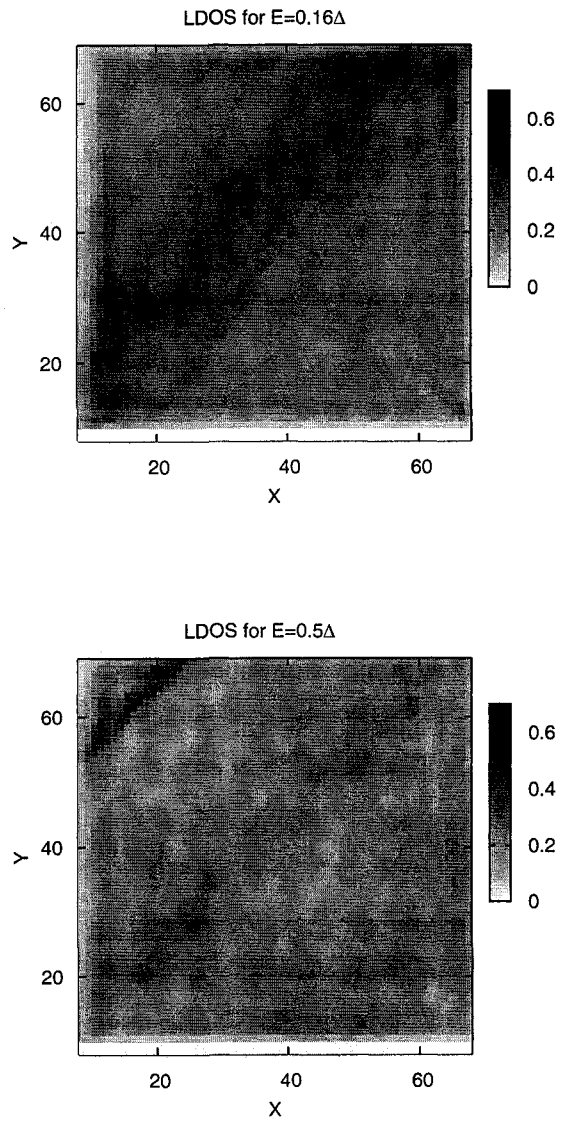

Figure 4.67: LDOS map for a square with 2 N/S interfaces, $\Delta = 0.3t$ and $L = 60a$

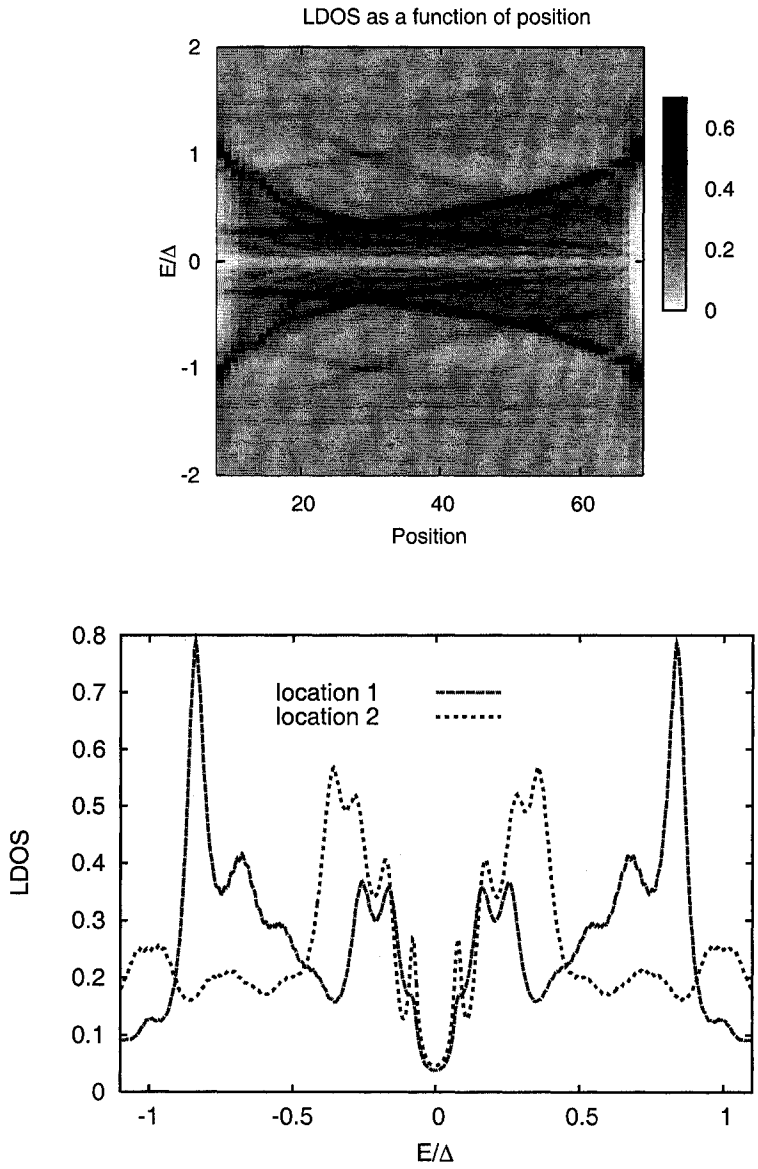

Figure 4.68: LDOS for a triangle with 3 N/S interfaces (taken along the arrow shown in Figure 4.60d), $\Delta = 0.3t$, $L = 60a$

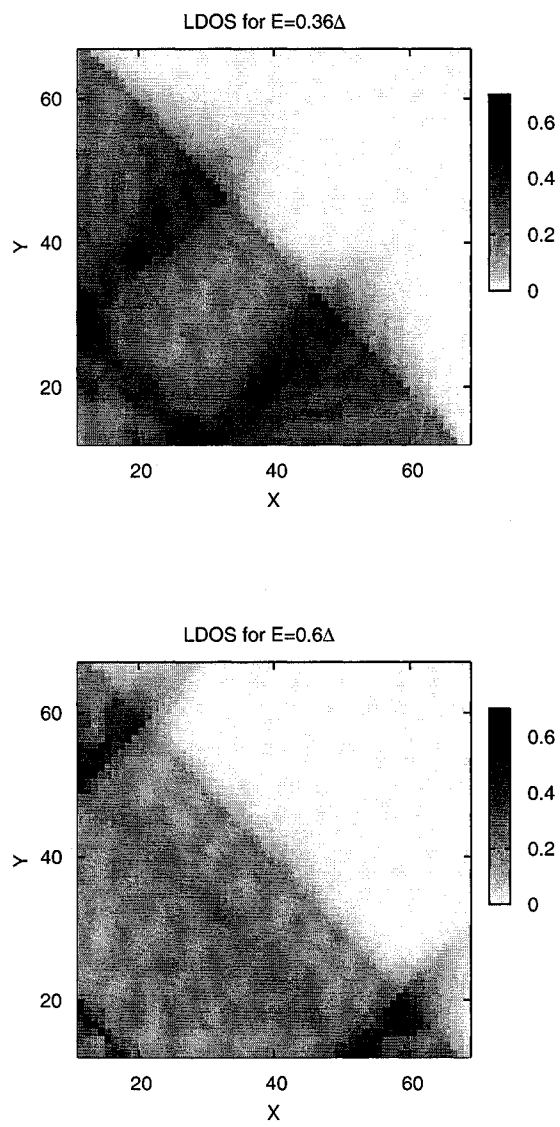

Figure 4.69: LDOS map for a triangle with 3 N/S interfaces, $\Delta = 0.3t$ and $L = 60a$

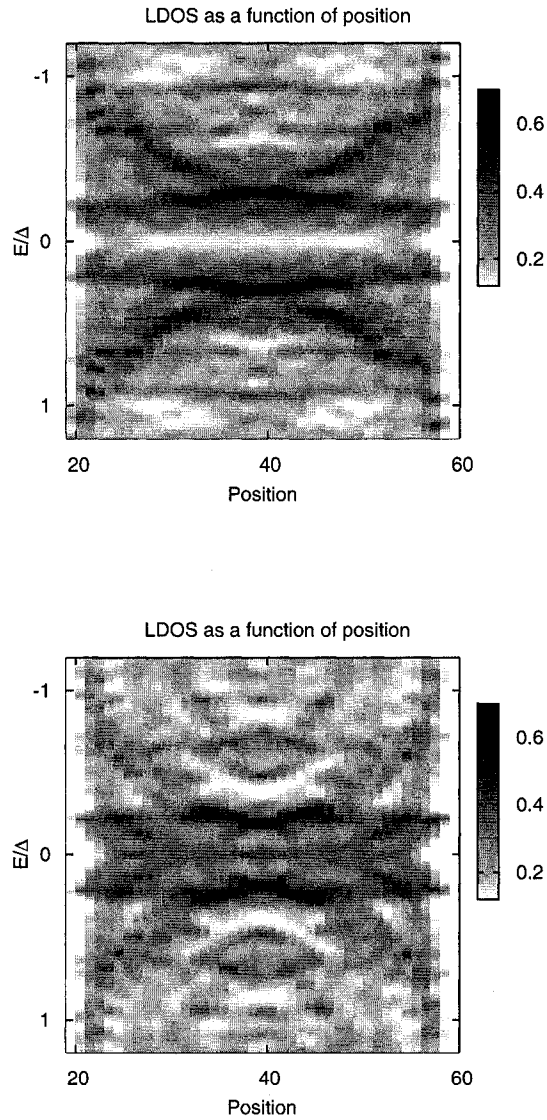

Figure 4.70: LDOS for a square with 4 N/d-wave interfaces (taken along the arrow shown in Figure 4.60a), $\Delta = 0.3t$, $L = 40a$

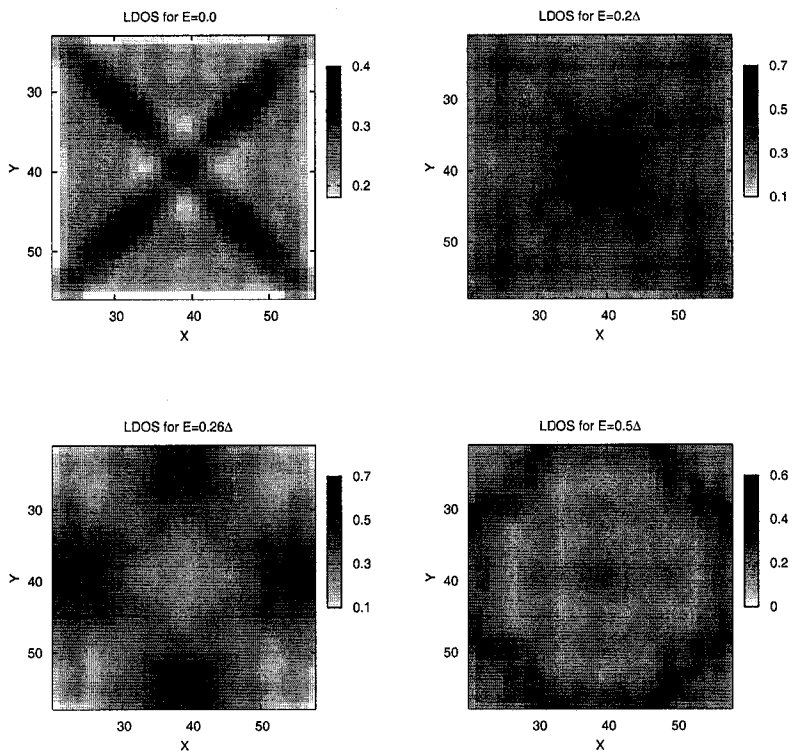

Figure 4.71: LDOS map for a square with 4 N/d-wave interfaces, $\Delta = 0.3t$ and $L = 40a$

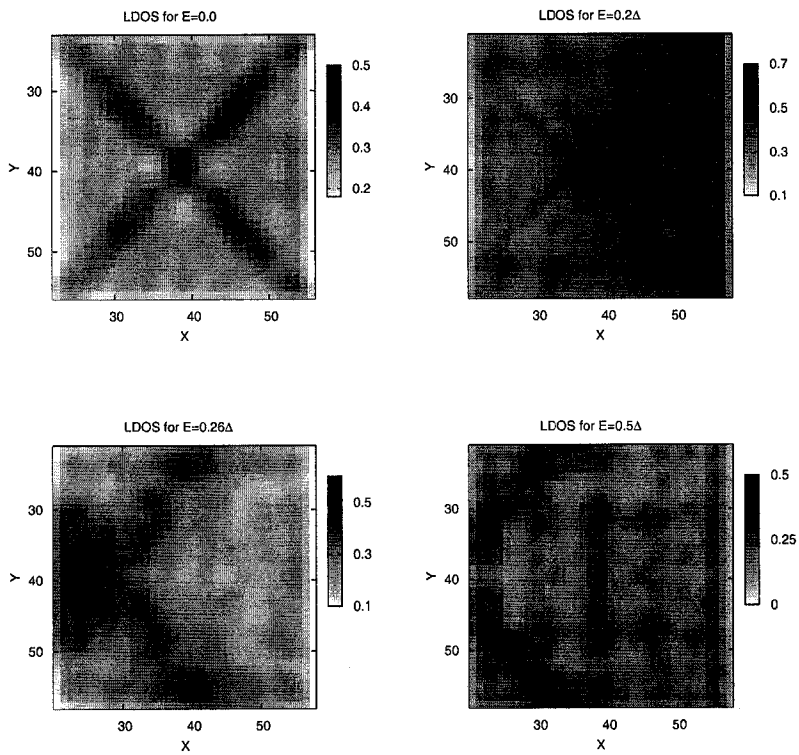

Figure 4.72: LDOS map for a square with 3 N/d-wave interfaces, $\Delta = 0.3t$ and $L = 40a$

Chapter 5

Conclusion

We have used quantum mechanical techniques to describe inhomogeneous problems in superconductors. We employed the Bogoliubov-de Gennes equations to describe important effects of s-wave and d-wave superconductors at surfaces and interfaces, and in the presence of disorder.

First we introduced a numerical method of solving the Bogoliubov-de Gennes equations in real-space. Secondly we considered different simplifications of numerical calculations near surfaces. These simplifications were made possible because of the restored translational symmetry along the surfaces. We have considered different surface geometries, like the (100), (110) and the c-axis ones. We have shown that in these cases the problem becomes an effective one-dimensional problem, making possible the usage of larger systems. We also introduced a recursive method, very well suited for solving quantum mechanical problems in real-space.

All these methods were applied to various applications. First we considered the simple scenario of s-wave and d-wave superconductivity near surfaces. We have shown that the order parameter oscillates near the surface on the order of the coherence length. Significant differences between s-wave and d-wave superconductivity near (100) and (110) surfaces have been uncovered. The appearance of the Zero Bias Conductance peak (ZBCP) due to the Zero Energy Andreev bound states, is observed only at the (110) surface of d-wave superconductors. We have also considered rough surfaces, and shown that due to the faceting on the atomic scale of the surface, ZBCP might appear also for a rough (100) surface, and that the degree of roughness will define the height of the ZBCP. Rough (110) surfaces see a depression of the height of the ZBCP.

We have also described superconductivity in finite size square samples. In addition to the behavior observed near surfaces, we also observe interference effects which are more pronounced when the coherence length of the superconductor is of the same order of magnitude as the size of the system.

Prompted by recent experiments on Josephson junctions made of high-T_c superconductors, we have investigated the giant proximity effect by considering a tri-layer

system made out of strong and weak superconductors. The leaking distance in the middle layer was calculated as a function of temperature and of the nature of the layer. We have shown that the above mentioned Josephson junction should carry supercurrents for temperatures higher than the critical temperature of the middle layer. This effect is not addressed in the conventional treatment of the proximity effect. In addition we have introduced embedded pockets of strong superconductivity and shown that this will increase even further the Josephson current. These results form a qualitative basis of understanding the giant proximity effect.

The formation of the Andreev bound states in a normal metal which is in contact with a superconductor, is also investigated. We describe the Andreev bound states forming in between s-wave and d-wave superconductors, either in the (100) or in the (110) geometry. We show that for the (110) geometry, the Zero Energy States (ZES) always form when a normal metal is in proximity with a d-wave superconductor.

The problem of Andreev bound states, localized in finite size normal metal samples, is solved using the recursive method. We show that the electron wave-function is localized in the normal metal and that the modes corresponding to various sub-gap energies, are localized in different parts of the system.

To summarize, we applied the tight-binding Hubbard Hamiltonian in the context of the Bogoliubov de Gennes equations in order to describe a multitude of inhomogeneous scenarios related to s-wave and d-wave superconductivity.

Bibliography

[1] H. Onnes, Comm. Leiden **120b** (1911).

[2] J.G. Bednorz and K.A. Müller, Zs. Phys B **64**, 189 (1986).

[3] J.G. Bednorz and K.A. Müller, Rev. Mod. Phys. **60**, 588 (1988).

[4] M.K. Wu, J.R. Ashburn, C.J. Torng, P.H. Hor, R.L. Meng, L. Goa, Z.J. Huang, Y.Q. Wang, and C.W. Chu, Phys. Rev. Lett. **58**, 908 (1987).

[5] H. Maeda, Y. Tanaka, M. Fukutomi, and T. Asano, Jpn. J. Appl. Phys. **37**, 3745 (1988).

[6] Z.Z. Sheng and A.M. Hermann, Nature **332**, 55 (1988).

[7] A. Schilling, M. Cantoni, J.D. Guo, and H.R. Ott, Nature **363**, 56 (1993).

[8] F. Steglich, J. Aarts, C. D. Bredl, W. Lieke, D. Meschede, W. Franz, and H. Schäfer, Phys. Rev. Lett. **43**, 1892 (1979).

[9] H. R. Ott, H. Rudigier, Z. Fisk, and J. L. Smith, Phys. Rev. Lett. **50**, 1595 (1983).

[10] G. R. Stewart, Z. Fisk, J. O. Willis, and J. L. Smith, Phys. Rev. Lett. **52**, 679 (1984).

[11] H. Urayama, H. Yamochi, G. Saito, K. Nozawa, T. Sugano, M. Kinoshita, S. Sato, K. Oshima, A. Kawamoto, and J. Tanaka, Chem. Lett. **55** (1988).

[12] C. N. Yang, Rev. Mod. Phys. **34**, 694 (1962).

[13] J. Bardeen, Phys. Rev. Lett. **6**, 57 (1961).

[14] M. H. Cohen, L. M. Falicov, and J. C. Phillips, Phys. Rev. Lett. **8**, 316 (1962).

[15] C. C. Tsuei and J. R. Kirtley, Rev. Mod. Phys. **72**, 969 (2000).

[16] J. Geerk, X. Xi, and G. Linker, Z. Phys. B **73**, 329 (1988).

[17] D. Mandrus, L. Forro, O. Koller, and L. Mihaly, Nature **351**, 460 (1991).

[18] S. Kashiwaya, Y. Tanaka, M. Koyanagi, H. Takashima, and K. Kajimura, Phys. Rev. B **51**, 1350 (1995).

[19] J. Lesueur, L. Greene, W. Feldmann, and A. Inam, Physica C: Supercond. **191**, 325 (1992).

[20] C.-R. Hu, Phys. Rev. Lett. **72**(10), 1526 (1994).

[21] M. Covington, M. Aprili, E. Paraoanu, L. Greene, F. Xu, J. Zhu, and C. Mirkin, Phys. Rev. Lett. **79**, 277 (1997).

[22] J. Wei, N.-C. Yeh, D. Garrigus, and M. Strasik, Phys. Rev. Lett. **81**, 2542 (1998).

[23] M. Matsumoto and H. Shiba, J. Phys. Soc. Jap. **65**, 2194 (1996).

[24] M. Fogelström, D. Rainer, and J. A. Sauls, Phys. Rev. Lett. **79**, 281 (1997).

[25] D. Rainer, H. Burkhardt, M. Fogelström, and J. Sauls, J. Phys. Chem. Solids **59**, 2040 (1998).

[26] I. Iguchi, W. Wang, M. Yamazaki, Y. Tanaka, and S. Kashiwaya, Phys. Rev. B **62**, R6131 (2000).

[27] Covington M., R. Scheuerer, K. Bloom, and L.H. Greene, Appl. Phys. Lett. **68**, 1717 (1996).

[28] M. Aprili, M. Covington, E. Paraoanu, B. Niedermeier, and L. H. Greene, Phys. Rev. B **57**, R8139 (1998).

[29] H. Hilgenkamp and J. Mannhart, Rev. Mod. Phys. **74**, 485 (2002).

[30] E. Il'ichev, V. Zakosarenko, R. Usselsteijn, V. Schultze, H.-G. Meyer, H. Hoenig, H. Hilgenkamp, and J. Mannhart, Phys. Rev. Lett. **81**, 894 (1998).

[31] E. Il'ichev, V. Zakosarenko, R. Ijsselsteijn, H. Hoenig, H.-G. Meyer, M. Fistul, and P. Müller, Phys. Rev. B **59**, 11502 (1999).

[32] Kashiwaya S. and Tanaka Y., Rep. Prog. Phys. **63**, 1641 (2000).

[33] Löfwander T., Shumeiko V.S., and Wendin G., Supercond. Sci. Technol. **14**, R53 (2001).

[34] A. V. Balatsky, I. Vekhter, and J.-X. Zhu, Rev. Mod. Phys. **78**, 373 (2006).

[35] Anderson P. W., J. Phys. Chem. Solids **11**, 26 (1959).

[36] A. Ghosal, M. Randeria, and N. Trivedi, Phys. Rev. Lett. **81**, 3940 (1998).

[37] R. Moradian, J. F. Annett, B. L. Györffy, and G. Litak, Phys. Rev. B **63**, 024501 (2000).

[38] K. Tanaka and F. Marsiglio, Phys. Rev. B **62**, 5345 (2000).

[39] J. M. Byers, M. E. Flatté, and D. J. Scalapino, Phys. Rev. Lett. **71**, 3363 (1993).

[40] A. V. Balatsky, M. I. Salkola, and A. Rosengren, Phys. Rev. B **51**, 15547 (1995).

[41] M. I. Salkola, A. V. Balatsky, and D. J. Scalapino, Phys. Rev. Lett. **77**, 1841 (1996).

[42] A. Yazdani, C. M. Howald, C. P. Lutz, A. Kapitulnik, and D. M. Eigler, Phys. Rev. Lett. **83**, 176 (1999).

[43] E. W. Hudson, S. H. Pan, A. K. Gupta, K.-W. Ng, and J. C. Davis, Science **285**, 88. (1999).

[44] S. Pan, E. Hudson, K. Lang, H. Elsaki, S. Uchida, and J. Davis, Nature **403**, 746 (2000).

[45] A. Yazdani, B. A. Jones, C. P. Lutz, M. F. Crommie, and D. M. Eigler, Science **275**, 1767 (1997).

[46] P. T. Sprunger, L. Petersen, E. W. Plummer, E. Lægsgaard, and F. Besenbacher, Science **275**, 1764 (1997).

[47] J. E. Hoffman, E. W. Hudson, K. M. Lang, V. Madhavan, H. Eisaki, S. Uchida, and J. C. Davis, Science **295**, 466 (2002).

[48] J. E. Hoffman, K. McElroy, D.-H. Lee, K. M. Lang, H. Eisaki, S. Uchida, and J. C. Davis, Science **297**, 1148 (2002).

[49] K. McElroy, R. W. Simmonds, J. E. Hoffman, D. H. Lee, J. Orenstein, H. Eisaki, S. Uchida, and J. C. Davis, Nature **422**, 592 (2003).

[50] S. H. Pan, J. P. O'Neal, R. L. Badzey, C. Chamon, H. Ding, J. R. Engelbrecht, Z. Wang, H. Eisaki, S. Uchida, A. K. Gupta, *et al.*, Nature **413**, 282 (2001).

[51] K. M. Lang, V. Madhavan, J. E. Hoffman, E. W. Hudson, H. Eisaki, S. Uchida, and J. C. Davis, Nature **415**, 412 (2002).

[52] McElroy K., Jinho Lee, J. A. Slezak, D.-H. Lee, H. Eisaki, S. Uchida, and J. C. Davis, Science **309**, 1048 (2005).

[53] V. L. Ginzburg and L. D. Landau, Zh. Eksp. Teor. Fiz. **20**, 1064 (1950).

[54] J. H. Chen, Phys. Rev. B **42**, 3952 (1990).

[55] J. H. Chen, Phys. Rev. B **42**, 3957 (1990).

[56] J. Bardeen, L.N. Cooper, and J.R. Schrieffer, Phys. Rev. **106**, 162 (1957).

[57] L. Gor'kov, Sov. Phys. JETP **7**, 505 (1958).

[58] A.A. Abrikosov, L.P. Gor'kov, and I.E. Dzayolshinski, *Methods of quantum field theory in statistical physics* (Dover, New York, 1963).

[59] G. Eilenberger, Z. Phys. **214**, 195 (1968).

[60] J. Rammer and H. Smith, Rev. Mod. Phys. **58**, 323 (1986).

[61] N. B. Kopnin, *Theory of nonequilibrium superconductivity* (Clarendon Press, Oxford, 2001).

[62] K. D. Usadel, Phys. Rev. Lett. **25**, 507 (1970).

[63] P. G. de Gennes, *Superconductivity of Metals and Alloys* (Benjamin, New York, 1966).

[64] L.N. Cooper, Phys. Rev. **104**, 1189 (1956).

[65] J. Bardeen, L.N. Cooper, and J.R. Schrieffer, Phys. Rev. **108**, 1175 (1957).

[66] Fröhlich, Phys. Rev. **79**, 845 (1950).

[67] R. Micnas, J. Ranninger, and S. Robaszkiewicz, Rev. Mod. Phys. **62**, 113 (1990).

[68] N. Bogoliubov, JETP USSR **43**, 58 (1958).

[69] J.G. Valatin, Nuovo Cim. **7**, 843 (1958).

[70] R. Combescot, Europhys. Lett **43**, 701 (1998).

[71] R. Micnas, J. Ranninger, S. Robaszkiewicz, and S. Tabor, Phys. Rev. B **37**, 9410 (1988).

[72] E. Anderson, Z. Bai, C. Bischof, S. Blackford, J. Demmel, J. Dongarra, J. Du Croz, A. Greenbaum, S. Hammarling, A. McKenney, *et al.*, *LAPACK Users' Guide* (Society for Industrial and Applied Mathematics, Philadelphia, PA, 1999), 3rd ed., ISBN 0-89871-447-8 (paperback).

[73] R. Haydock, V. Heine, and M. J. Kelly, Journal of Physics C: Solid State Physics **5**(20), 2845 (1972).

[74] R. Haydock, V. Heine, and M. J. Kelly, Journal of Physics C: Solid State Physics **8**(16), 2591 (1975).

[75] R. Haydock, Solid State Phys. **35**, 215 (1980).

[76] M. Foulkes and R. Haydock, Journal of Physics C: Solid State Physics **19**(33), 6573 (1986).

[77] M. J. Kelly, Solid State Phys. **35**, 295 (1980).

[78] G. D. Mahan, *Many Particle Physics* (Kluwer, New York, 2000), 3rd ed.

[79] C. Lanczos, J. Res. Nat.Bur.Stand. **45**, 255 (1950).

[80] G. Litak and B. Györffy, Phys Rev B **62**(10), 6629 (2000).

[81] A. M. Martin and J. F. Annett, Superlattices and Microstructures **25**, 1019 (1999).

[82] A. M. Martin and J. F. Annett, Phys. Rev. B **57**, 8709 (1998).

[83] E. Vecino, A. Martin-Rodero, and A. Yeyati, Phys. Rev. B **64**, 1845021 (2001).

[84] Y. Nambu, Phys. Rev. **117**, 648 (1960).

[85] J. R. Schrieffer, *Theory of superconductivity* (Perseus Books, Reading, Massachusetts, 1964), revised ed.

[86] S. Balay, K. Buschelman, W. D. Gropp, D. Kaushik, M. G. Knepley, L. C. McInnes, B. F. Smith, and H. Zhang, *PETSc Web page* (2001), http://www.mcs.anl.gov/petsc.

[87] R. Golub, R. Underwood, and J. H. Wilkinson, Tech. Rep. STAN-CS-72-720, Comp. Sci. Dept., Stanford University (1972).

[88] B. N. Parlett and D. Scott, Math. Comp **33**, 217 (1979).

[89] H. D. Simon, Math. Comp. **42**(165), 115 (1986).

[90] K. Tanaka and F. Marsiglio, J. Phys. Chem. of Solids **63**, 2287 (2002).

[91] A. L. Fetter, Phys. Rev. **140**, A1921 (1965).

[92] A. Sharoni, O. Millo, A. Kohen, Y. Dagan, R. Beck, G. Deutscher, and G. Koren, Phys. Rev. B **65**, 134526 (2002).

[93] L. Alff, H. Takashima, S. Kashiwaya, N. Terada, H. Ihara, Y. Tanaka, M. Koyanagi, and K. Kajimura, Phys. Rev. B **55**, R14757 (1997).

[94] J. H. Xu, J. H. Miller, and C. S. Ting, Phys. Rev. B **53**, 3604 (1996).

[95] Y. Tanuma, Y. Tanaka, M. Ogata, and S. Kashiwaya, Phys. Rev. B **60**, 9817 (1999).

[96] C.-R. Hu, Phys. Rev. B **57**(2), 1266 (1998).

[97] J. Yang and C.-R. Hu, Phys. Rev. B **50**, 16766 (1994).

[98] J.-X. Zhu, B. Friedman, and C. S. Ting, Phys. Rev. B **59**, 3353 (1999).

[99] N. Stefanakis, Phys. Rev. B **66**, 024514 (2002).

[100] V. G. Kogan, Phys. Rev. B **26**, 88 (1982).

[101] P. G. de Gennes, Rev. Mod. Phys. **36**, 225 (1964).

[102] W. L. McMillan, Phys. Rev. **175**, 559 (1968).

[103] W. L. McMillan, Phys. Rev. **175**, 537 (1968).

[104] N. R. Werthamer, Phys. Rev. **132**, 2440 (1963).

[105] J. Z. Wu, X. X. Yao, C. S. Ting, and W. K. Chu, Phys. Rev. B **46**, 14059 (1992).

[106] J. E. Hirsch, Physica C **194**, 119 (1992).

[107] J.-X. Zhu and C. S. Ting, Phys. Rev. B **61**, 1456 (2000).

[108] K. Halterman and O. T. Valls, Phys. Rev. B **65**, 014509 (2001).

[109] I. Bozovic, G. Logvenov, M. A. J. Verhoeven, P. Caputo, E. Goldobin, and M. R. Beasley, Phys. Rev. Lett. **93** (2004).

[110] V. Kresin, Yu. Ovchinnikov, and S. Wolf, Appl. Phys. Lett. **83**, 722 (2003).

[111] G. Alvarez, M. Mayr, A. Moreo, and E. Dagotto, Phys. Rev. B **71**, 014514 (2005).

[112] Z. X. Zhu (2005), cond-mat/0508646.

[113] A. A. Golubov, M. Y. Kupriyanov, and E. Il'ichev, Reviews of Modern Physics **76**, 411 (2004).

[114] Y. Tanaka and S. Kashiwaya, Phys. Rev. Lett. **74**, 3451 (1995).

[115] Y. Tanaka and S. Kashiwaya, Phys. Rev. B **56**, 892 (1997).

[116] Y. Tanaka and S. Kashiwaya, Phys. Rev. B **53**, R11957 (1996).

[117] Y. Tanaka, Y. V. Nazarov, and S. Kashiwaya, Phys. Rev. Lett. **90**(16), 167003, 167003 (4 pages) (2003).

[118] Y. Tanaka, Y. V. Nazarov, A. A. Golubov, and S. Kashiwaya, Phys. Rev. B **69**, 144519 (2004).

[119] K. A. Delin and A. W. Kleinsasser, Supercond. Sci. Technol. **9**, 227 (1996).

[120] K. K. Likharev, Rev. Mod. Phys. **51**, 101 (1979).

[121] L. Covaci and F. Marsiglio, Phys. Rev. B **73**, 014503 (2006).

[122] V. Ambegaokar and A. Baratoff, Phys. Rev. Lett. **10**, 486 (1963).

[123] A. Martín-Rodero, F. J. García-Vidal, and A. Levy Yeyati, Phys. Rev. Lett. **72**, 554 (1994).

[124] A. Andreev, Sov. Phys. JETP **19**, 1228 (1964).

[125] P. De Gennes and D. Saint-James, Phys. Lett. **4**, 151 (1963).

[126] C. Caroli, P. De Gennes, and J. Matricon, Phys. Lett. **9**, 307 (1964).

[127] A. F. Andreev, Sov. Phys. JETP **22**, 455 (1966).

[128] R. Wilkins, M. Amman, R. Soltis, E. Ben-Jacob, and R. Jaklevic, Phys. Rev. B **41**, 8904 (1990).

[129] H. Hess, R. Robinson, and J. Waszczak, Phys. Rev. Lett. **64**, 2711 (1990).

[130] G. Blonder, M. Tinkham, and T. Klapwijk, Phys. Rev. B **25** (1982).

[131] M. Titov, N. A. Mortensen, H. Schomerus, and C. W. J. Beenakker, Phys. Rev. B **64**, 134206 (2001).

[132] Y. Tanuma, Y. Tanaka, M. Yamashiro, and S. Kashiwaya, Phys. Rev. B **57**, 7997 (1998).

[133] W. Escoffier, C. Chapelier, and F. Lefloch, Phys. Rev. B **72**, 140502 (2005).

[134] I. Kosztin, D. L. Maslov, and P. M. Goldbart, Phys. Rev. Lett. **75**, 1735 (1995).

[135] A. Lodder and Y. V. Nazarov, Phys. Rev. B **58**, 5783 (1998).

[136] F. Libisch, S. Rotter, J. Burgdorfer, A. Kormanyos, and J. Cserti, Phys. Rev. B **72**, 075304 (2005).

[137] J. Cserti, A. Bodor, J. Koltai, and G. Vattay, Phys. Rev. B **66**, 064528 (2002).

[138] J. Cserti, A. Kormányos, Z. Kaufmann, J. Koltai, and C. J. Lambert, Phys. Rev. Lett. **89**, 057001 (2002).

[139] A. Kormanyos, Z. Kaufmann, J. Cserti, and C. J. Lambert, Phys. Rev. B **67**, 172506 (2003).

[140] H. Schomerus and C. W. J. Beenakker, Phys. Rev. Lett. **82**, 2951 (1999).

Appendix A

Homogeneous superconductivity - k-space

In the presence of homogeneity and periodic boundary conditions, we can Fourier transform all the spatial operators to momentum-space operators:

$$c_{i\sigma} = \frac{1}{N}\sum_{k} c_{k\sigma} e^{-i\mathbf{k}\cdot\mathbf{R_i}}, \tag{A.1}$$

where N is the total number of points in the lattice.

Applying this transformation to the kinetic part of the mean-field Hamiltonian Eq. (2.18) we have:

$$\mathcal{K} = \frac{1}{N^2}\sum_{<ij>\sigma}(-t-\delta_{ij}\mu)\sum_{kq} c^{\dagger}_{k\sigma}c_{q\sigma}e^{-i(\mathbf{q}-\mathbf{k})\cdot\mathbf{R}_i}e^{-i\mathbf{q}\cdot\delta} \tag{A.2}$$

where $\delta = \mathbf{R_j} - \mathbf{R_i}$. For nearest-neighbors on a 2D square lattice δ is $\pm a\mathbf{x}$ or $\pm a\mathbf{y}$, where a is the lattice constant. Because we consider an uniform system with periodic boundary conditions, the following relation is true:

$$\frac{1}{N}\sum_{i} e^{-i(\mathbf{q}-\mathbf{k})\cdot\mathbf{R}_i} = \delta(q-k), \tag{A.3}$$

where $\delta(q-k)$ is the Dirac delta function. Using Eq. (A.3), the Fourier transform of the kinetic energy becomes:

$$\mathcal{K} = \frac{1}{N}\sum_{k\sigma}(\epsilon_k - \mu)c^{\dagger}_{k\sigma}c_{k\sigma}, \tag{A.4}$$

where,

$$\epsilon_k = -2tcos(k_x a) - 2tcos(k_y a) \tag{A.5}$$

is the kinetic energy of an electron with momentum k.

The potential energy term from the Hamiltonian has two parts, $\mathcal{V} = \mathcal{V}_o + \mathcal{V}_{nn}$, describing the on-site and the nearest neighbor interactions. The same procedure as presented above can be applied for obtaining the momentum-space potential energy. The on-site potential energy can be written as:

$$\begin{aligned}
\mathcal{V}_o &= U\sum_i \langle c_{i\downarrow}c_{i\uparrow}\rangle c^\dagger_{i\uparrow}c^\dagger_{i\downarrow} + h.c. \\
&= \frac{U}{N^4}\sum_i \sum_{k_1,k_2,k_3,k_4} \langle c_{k_1\downarrow}c_{k_2\uparrow}\rangle c^\dagger_{k_3\uparrow}c^\dagger_{k_4\downarrow} e^{-i\mathbf{R}_i(\mathbf{k}_1-\mathbf{k}_3+\mathbf{k}_2-\mathbf{k}_4)} + h.c. \\
&= \frac{U}{N^3}\sum_{k_2,k_3,k_4} \langle c_{-k_2+k_3+k_4\downarrow}c_{k_2\uparrow}\rangle c^\dagger_{k_3\uparrow}c^\dagger_{k_4\downarrow} + h.c. \qquad \text{(A.6)}
\end{aligned}$$

the summation over i resulted in a Dirac delta function, according to Eq. (A.1). This allows the elimination of one momentum variable (k_1). Changing the momentum variables: $k_2 = k$, $k_3 = k'$ and $k_4 + k_3 = q$, equation (A.6) becomes:

$$\mathcal{V}_o = \frac{U}{N^3}\sum_{k,q-k',k'} \langle c_{-k+q\downarrow}c_{k\uparrow}\rangle c^\dagger_{k'\uparrow}c^\dagger_{q-k'\downarrow} + h.c. \qquad \text{(A.7)}$$

We now choose the reduced Hamiltonian form, for which the momentum q is set to zero. This state corresponds to the lowest energy state with zero center of mass momentum, paired electrons will have opposite momenta. Eq. (A.7) will now have the reduced form:

$$\mathcal{V}_o = \frac{U}{N^2}\sum_{k,k'} \langle c_{-k'\downarrow}c_{k'\uparrow}\rangle c^\dagger_{k\uparrow}c^\dagger_{-k\downarrow} + h.c. \qquad \text{(A.8)}$$

For a typical term in the nearest-neighbor part of the potential energy, we obtain:

$$\begin{aligned}
\mathcal{V}_{nn} &= \frac{V}{2}\sum_{\langle i,j\rangle} \langle c_{i\alpha}c_{j\beta}\rangle c^\dagger_{j\beta}c^\dagger_{i\alpha} \\
&= \frac{V}{N^4}\sum_{k_1,k_2,k_3,k_4} \sum_{i,\delta} \langle c_{k_1\alpha}c_{k_2\beta}\rangle c^\dagger_{k_3\beta}c^\dagger_{k_4\alpha} e^{i\mathbf{R}_i(\mathbf{k}_1-\mathbf{k}_4+\mathbf{k}_2-\mathbf{k}_3)} e^{i\delta(\mathbf{k}_2-\mathbf{k}_4)} \\
&= \frac{V}{2N^3}\sum_{k_1,k_2,k_3} \sum_{\delta} \langle c_{-k_2+k_3+k_4\alpha}c_{k_2\beta}\rangle c^\dagger_{k_3\beta}c^\dagger_{k_4\alpha} e^{-i\delta(\mathbf{k}_4-\mathbf{k}_2)}, \qquad \text{(A.9)}
\end{aligned}$$

where $\delta = \mathbf{R}_j - \mathbf{R}_i$ is the distance between nearest neighbors. The spin indices α and β will be $\uparrow$,$\downarrow$ or $\downarrow$,$\uparrow$ depending on which term in the Hamiltonian we are referring to. Using the previously introduced momentum change of variables and considering only the zero center of mass situation ($q = 0$), Eq. (A.9) becomes:

$$\mathcal{V}_{nn} = \frac{V}{2N^2}\sum_{k,k'} \langle c_{-k'\alpha}c_{k'\beta}\rangle c^\dagger_{k\beta}c^\dagger_{-k\alpha} \sum_{\delta} e^{-i\delta(\mathbf{k}-\mathbf{k}')} \qquad \text{(A.10)}$$

Gathering the information contained in Eq. (A.4), Eq. (A.8) and Eq. (A.10) the momentum-space counterpart of the extended Hubbard Hamiltonian has the following form:

$$\mathcal{H} = \frac{1}{N}\sum_{k,\sigma}(\epsilon_k - \mu)c^{\dagger}_{k\sigma}c_{k\sigma} + \frac{1}{N}\sum_{k}\Delta_k c^{\dagger}_{k\uparrow}c^{\dagger}_{-k_\downarrow} + h.c. \tag{A.11}$$

The superconducting order parameter is defined as:

$$\Delta_k = \frac{1}{N}\sum_{k'} V_{kk'}\langle c_{-k'\downarrow}c_{k'\uparrow}\rangle, \tag{A.12}$$

where $V_{kk'} = U + V\gamma_{k-k'}$ with $\gamma_k = 2(\cos k_x a + \cos k_y a)$.

Appendix B

The Bogoliubov-de Gennes Equations

Using the real-space Hamiltonian Eq. (2.18) and the Bogoliubov-Valatin transformations Eq. (2.61),Eq. (2.62), we can write the following commutators:

$$\begin{aligned}
[\mathcal{H}, \gamma_{n\sigma}] &= \sum_{n'\sigma'} \epsilon_{n'} [\gamma^{\dagger}_{n'\sigma'}\gamma_{n'\sigma'}, \gamma_{n\sigma}] \\
&= \sum_{n'\sigma'} \epsilon_{n'} (\gamma^{\dagger}_{n'\sigma'}\gamma_{n'\sigma'}\gamma_{n\sigma} - \gamma_{n\sigma}\gamma^{\dagger}_{n'\sigma'}\gamma_{n'\sigma'}) \\
&= -\sum_{n'\sigma'} \epsilon_{n'} \{\gamma^{\dagger}_{n'\sigma'}, \gamma_{n\sigma}\}\gamma_{n'\sigma'} \\
&= -\sum_{n'\sigma'} \epsilon_{n'} \delta_{n,n'}\delta_{\sigma,\sigma'}\gamma_{n'\sigma'} \\
&= -\epsilon_n \gamma_{n\sigma}, \qquad \text{(B.1)}
\end{aligned}$$

and

$$\begin{aligned}
[\mathcal{H}, \gamma^{\dagger}_{n\sigma}] &= \sum_{n'\sigma'} \epsilon_{n'} [\gamma^{\dagger}_{n'\sigma'}\gamma_{n'\sigma'}, \gamma^{\dagger}_{n\sigma}] \\
&= \sum_{n'\sigma'} \epsilon_{n'} (\gamma^{\dagger}_{n'\sigma'}\gamma_{n'\sigma'}\gamma^{\dagger}_{n\sigma} - \gamma^{\dagger}_{n\sigma}\gamma^{\dagger}_{n'\sigma'}\gamma_{n'\sigma'}) \\
&= \sum_{n'\sigma'} \epsilon_{n'} \gamma^{\dagger}_{n'\sigma'} \{\gamma^{\dagger}_{n\sigma}, \gamma_{n'\sigma'}\} \\
&= \sum_{n'\sigma'} \epsilon_{n'} \delta_{n,n'}\delta_{\sigma,\sigma'}\gamma^{\dagger}_{n'\sigma'} \\
&= \epsilon_n \gamma^{\dagger}_{n\sigma}. \qquad \text{(B.2)}
\end{aligned}$$

In order to obtain the Bogoliubov-de Gennes equations, we must calculate the commutator of the mean-field Hamiltonian with the electron operators $c_{i\uparrow}$ and $c_{i\downarrow}$ in two separate ways, either by using directly the electron operators, or by using the quasiparticle operators.

First we use the form of the Hamiltonian dependent on the electron operators:

$$[\mathcal{H}, c_{l\uparrow}] = \left[\sum_{\langle ij\rangle\sigma}(-t_{ij} - \delta_{ij}(\mu - \xi_i))c^\dagger_{i\sigma}c_{j\sigma} + \sum_i(\Delta_i c^\dagger_{i\uparrow}c^\dagger_{i\downarrow} + h.c.) + \sum_{\langle ij\rangle}[(\Delta^{\downarrow\uparrow}_{ij}c^\dagger_{j\uparrow}c^\dagger_{i\downarrow} + \Delta^{\uparrow\downarrow}_{ij}c^\dagger_{j\downarrow}c^\dagger_{i\uparrow}) + h.c.], c_{l\uparrow}\right]. \quad \text{(B.3)}$$

Calculating each term separately we obtain:

$$\begin{aligned}
[c^\dagger_{i\sigma}c_{j\sigma}, c_{l\uparrow}] &= c^\dagger_{i\sigma}c_{j\sigma}c_{l\uparrow} - c_{l\uparrow}c^\dagger_{i\sigma}c_{j\sigma} \\
&= -\{c^\dagger_{i\sigma}, c_{l\uparrow}\}c_{j\sigma} \\
&= -\delta_{il}\delta_{\sigma\uparrow}c_{j\sigma}, \\
[c^\dagger_{i\uparrow}c^\dagger_{i\downarrow}, c_{l\uparrow}] &= c^\dagger_{i\uparrow}c^\dagger_{i\downarrow}c_{l\uparrow} - c_{l\uparrow}c^\dagger_{i\uparrow}c^\dagger_{i\downarrow} \\
&= -\{c^\dagger_{i\uparrow}, c_{l\uparrow}\}c^\dagger_{i\downarrow} \\
&= -\delta_{il}c^\dagger_{i\downarrow}, \\
[c^\dagger_{j\uparrow}c^\dagger_{i\downarrow}, c_{l\uparrow}] &= c^\dagger_{j\uparrow}c^\dagger_{i\downarrow}c_{l\uparrow} - c_{l\uparrow}c^\dagger_{j\uparrow}c^\dagger_{i\downarrow} \\
&= -\{c^\dagger_{j\uparrow}, c_{l\uparrow}\}c^\dagger_{j\downarrow} \\
&= -\delta_{jl}c^\dagger_{i\downarrow}, \\
[c^\dagger_{j\downarrow}c^\dagger_{i\uparrow}, c_{l\uparrow}] &= c^\dagger_{j\downarrow}c^\dagger_{i\uparrow}c_{l\uparrow} - c_{l\uparrow}c^\dagger_{j\downarrow}c^\dagger_{i\uparrow} \\
&= c^\dagger_{j\downarrow}\{c_{l\uparrow}, c^\dagger_{j\downarrow}\} \\
&= \delta_{il}c^\dagger_{j\downarrow}, \\
[c_{i\uparrow}c_{i\downarrow}, c_{l\uparrow}] &= 0, \\
[c_{i\uparrow}c_{j\downarrow}, c_{l\uparrow}] &= 0.
\end{aligned}$$

The terms in the commutator $[\mathcal{H}, c_{l\downarrow}]$ can be obtained in a similar manner:

$$\begin{aligned}
[c^\dagger_{i\sigma}c_{j\sigma}, c_{l\downarrow}] &= -\delta_{il}\delta_{\sigma\downarrow}c_{j\sigma}, \\
[c^\dagger_{i\uparrow}c^\dagger_{i\downarrow}, c_{l\downarrow}] &= \delta_{il}c^\dagger_{i\uparrow}, \\
[c^\dagger_{j\uparrow}c^\dagger_{i\downarrow}, c_{l\downarrow}] &= \delta_{jl}c^\dagger_{j\uparrow}, \\
[c^\dagger_{j\downarrow}c^\dagger_{i\uparrow}, c_{l\downarrow}] &= \delta_{jl}c^\dagger_{i\uparrow}, \\
[c_{i\uparrow}c_{i\downarrow}, c_{l\downarrow}] &= 0, \\
[c_{i\uparrow}c_{j\downarrow}, c_{l\downarrow}] &= 0.
\end{aligned}$$

Putting everything together in Eq. (B.3) and summing over $< ij >$ and σ the commutators simplify to:

$$[\mathcal{H}, c_{l\uparrow}] = \sum_{\delta} t_{ll+\delta} c_{l+\delta\uparrow} + (\mu + \xi_l) c_{l\uparrow} + \sum_{\delta} (-\Delta^{\downarrow\uparrow}_{ll+\delta} + \Delta^{\uparrow\downarrow}_{ll+\delta}) c_{l+\delta\downarrow} - \Delta_l c_{l\downarrow} \quad \text{(B.4)}$$

$$[\mathcal{H}, c_{l\downarrow}] = \sum_{\delta} t_{ll+\delta} c_{l+\delta\downarrow} + (\mu + \xi_l) c_{l\downarrow} + \sum_{\delta} (\Delta^{\downarrow\uparrow}_{ll+\delta} - \Delta^{\uparrow\downarrow}_{ll+\delta}) c_{l+\delta\uparrow} + \Delta_l c_{l\uparrow}, \quad \text{(B.5)}$$

where $\sum_{\delta}$ is a summation over the nearest neighbors of l.

If we use the diagonal form of the Hamiltonian coupled with the Bogoliubov-Valatin transformations and compute the same commutators we get:

$$\begin{aligned} [\mathcal{H}, c_{l\uparrow}] &= \sum_{n} [u^l_n [\mathcal{H}, \gamma_{n\uparrow}] - v^{l\star}_n [\mathcal{H}, \gamma^{\dagger}_{n\downarrow}]] \\ &= \sum_{n} [-\epsilon_n u^l_n \gamma_{n\uparrow} - \epsilon_n v^{l\star}_n \gamma^{\dagger}_{n\downarrow}], \quad \text{(B.6)} \\ [\mathcal{H}, c_{l\downarrow}] &= \sum_{n} [u^l_n [\mathcal{H}, \gamma_{n\downarrow}] + v^{l\star}_n [\mathcal{H}, \gamma^{\dagger}_{n\uparrow}]] \\ &= \sum_{n} [-\epsilon_n u^l_n \gamma_{n\downarrow} + \epsilon_n v^{l\star}_n \gamma^{\dagger}_{n\uparrow}]. \quad \text{(B.7)} \end{aligned}$$

Using once again the Bogoliubov-Valatin transformations in Eq. (B.4) and Eq. (B.5) and identifying the coefficients of $\gamma_{n\uparrow}$, $\gamma_{n\downarrow}$,$\gamma^{\dagger}_{n\uparrow}$ and $\gamma^{\dagger}_{n\downarrow}$ we obtain:

$$\epsilon_n u^l_n = -\sum_{\delta} t_{ll+\delta} u^{l+\delta}_n - (\mu + \xi_l) u^l_n + \Delta_l v^l_n + \sum_{\delta} (\Delta^{\downarrow\uparrow}_{ll+\delta} - \Delta^{\uparrow\downarrow}_{ll+\delta}) v^{l+\delta}_n \quad \text{(B.8)}$$

$$\epsilon_n v^l_n = \sum_{\delta} t_{ll+\delta} v^{l+\delta}_n + (\mu + \xi_l) v^l_n + \Delta^{\star}_l u^l_n + \sum_{\delta} (\Delta^{\downarrow\uparrow\star}_{ll+\delta} - \Delta^{\uparrow\downarrow\star}_{ll+\delta}) u^{l+\delta}_n \quad \text{(B.9)}$$

Eq. (B.8) and Eq. (B.9) are known as the Bogoliubov-de Gennes equations [63].

Appendix C

Fourier transform in the 110 direction

The description of 110 surfaces is shown in Figure 3.5. Consider two type of sites A and B forming a unit cell with index coordinates x and y. The presence of a 110 surface implies that the system in homogeneous in the y direction. We can Fourier transform the y coordinate to momentum space k. The spatial coordinates of type A sites are $R^A_{xy} = xa\sqrt{(2)}\hat{x} + ya\sqrt{2}\hat{y}$ while the coordinates of type B sites are $R^B_{xy} = (x+1/2)a\sqrt{2}\hat{x} + (y+1/2)a\sqrt{2}\hat{y}$, where a is the lattice constant. The Fourier transform of the electron operators is:

$$c^A_{xy\sigma} = \frac{1}{N}\sum_k c_{x\sigma}(k)e^{-iyka\sqrt{2}} \tag{C.1}$$

$$c^B_{xy\sigma} = \frac{1}{N}\sum_k c_{x\sigma}(k)e^{-i(y+\frac{1}{2})ka\sqrt{2}} \tag{C.2}$$

In the presence of periodic boundary conditions in the y direction, the following relation is true:

$$\frac{1}{N}\sum_k e^{iy(k-k')a} = \delta(k-k'). \tag{C.3}$$

Considering the mean-field Hamiltonian (2.18), it can be rewritten in terms of the unit cells defined previously. If we write explicitly the nearest neighbors, for the kinetic energy part we get:

$$\begin{aligned}\mathcal{K} = \sum_{xy\sigma} & -t^a_{xx}c^{A\dagger}_{x\,y\sigma}c^B_{x\,y\sigma} - t^A_{xx-1}c^{A\dagger}_{x\,y\sigma}c^B_{x-1\,y\sigma} - t^A_{xx-1}c^{A\dagger}_{x\,y\sigma}c^B_{x-1\,y-1\sigma} - t^A_{xx}c^{A\dagger}_{x\,y\sigma}c^B_{x\,y-1\sigma} - \\ & - t^B_{xx}c^{B\dagger}_{x\,y\sigma}c^A_{x\,y\sigma} - t^B_{xx+1}c^{B\dagger}_{x\,y\sigma}c^A_{x+1\,y\sigma} - t^B_{xx}c^{B\dagger}_{x\,y\sigma}c^A_{x\,y+1\sigma} - t^B_{xx+1}c^{B\dagger}_{x\,y\sigma}c^A_{x+1\,y+1\sigma},\end{aligned} \tag{C.4}$$

where $t^A_{xx} = t^B_{xx}$, $t^A_{xx-1} = t^B_{x-1x}$ and $t^B_{xx+1} = t^A_{x+1x}$ are the hopping amplitudes dependent only on the x coordinate. A surface at $x = i$ is achieved if we set $t^A_{ii-1} = 0$ and $t^B_{i-1i} = 0$.

Using the Fourier transform (C.1) - (C.1) and the relation (C.3) into Eq. (C.4), the kinetic part of the Hamiltonian becomes:

$$\begin{aligned}\mathcal{K} &= \frac{1}{N}\sum_{xk\sigma} -2\cos\frac{ka\sqrt{2}}{2}\left[t^A_{xx}c^{A\dagger}_{x\sigma}(k)c^B_{x\sigma}(k) + t^A_{xx-1}c^{A\dagger}_{x\sigma}(k)c^B_{x-1\sigma}(k)\right.\\ &+ \left. t^B_{xx}c^{B\dagger}_{x\sigma}(k)c^A_{x\sigma}(k) + t^B_{xx+1}c^{B\dagger}_{x\sigma}(k)c^A_{x+1\sigma}(k)\right]. \qquad \text{(C.5)}\end{aligned}$$

For the chemical potential term we obtain:

$$\mathcal{H}_\mu = \frac{1}{N}\sum_{k\sigma}(-\mu-\xi_x)[c^{A\dagger}_{x\sigma}(k)c^A_{x\sigma}(k) + c^{B\dagger}_{x\sigma}(k)c^B_{x\sigma}(k)] \qquad \text{(C.6)}$$

The on-site interaction term can be calculated in a similar way:

$$\mathcal{H}_0 = \frac{1}{N}\sum_{xk}\Delta^A_x c^{A\dagger}_{x\uparrow}(k)c^{A\dagger}_{x\downarrow}(-k) + \Delta^B_x c^{B\dagger}_{x\uparrow}(k)c^{B\dagger}_{x\downarrow}(-k) + h.c., \qquad \text{(C.7)}$$

where we assumed that $\langle c_{xy\uparrow}c_{xy\downarrow}\rangle$ is not dependent on y. We can define Bogoliubov - Valatin transformations for type A electron operator:

$$c^A_{x\uparrow}(k) = \sum_n u^{xA}_n(k)\gamma_{n\uparrow}(k) - v^{xA*}_n(k)\gamma^\dagger_{n\downarrow}(-k), \qquad \text{(C.8)}$$

$$c^A_{x\downarrow}(-k) = \sum_n u^{xA}_n(k)\gamma_{n\downarrow}(-k) + v^{xA*}_n(k)\gamma^\dagger_{n\uparrow}(k) \qquad \text{(C.9)}$$

and identical for type B, $c^B_{x\uparrow}(k)$ and $c^B_{x\downarrow}(-k)$. Making use of these transformations and of the quasiparticle averages $\langle\gamma^\dagger_{n\alpha}\gamma_{m\beta}\rangle = \delta_{mn}\delta_{\alpha\beta}f_n$ and $\langle\gamma_{n\alpha}\gamma_{m\beta}\rangle = 0$ we can write the on-site order parameters:

$$\Delta^A_x = -\frac{1}{N}\sum_k\sum_n u^{Ax}_n(k)v^{Ax*}_n(k)(1-2f_n(k)) \qquad \text{(C.10)}$$

$$\Delta^B_x = -\frac{1}{N}\sum_k\sum_n u^{Ax}_n(k)v^{Ax*}_n(k)(1-2f_n(k)) \qquad \text{(C.11)}$$

The nearest neighbor interaction term, similar to the kinetic energy, can be written as the sum over the cells containing both A and B type sites:

$$\begin{aligned}\mathcal{H}_{nn} &= \sum_{xy}[V^B_{xx}\langle c^A_{xy+1\uparrow}c^B_{xy\downarrow}\rangle c^{B\dagger}_{xy\downarrow}c^{A\dagger}_{xy+1\uparrow} + V^B_{xx+1}\langle c^A_{x+1y+1\uparrow}c^B_{xy\downarrow}\rangle c^{B\dagger}_{xy\downarrow}c^{A\dagger}_{x+1y+1\uparrow}\\ &+ V^A_{x-1x}\langle c^B_{x-1y\uparrow}c^A_{xy\downarrow}\rangle c^{A\dagger}_{xy\downarrow}c^{B\dagger}_{x-1y\uparrow} + V^A_{xx}\langle c^B_{xy\uparrow}c^A_{xy\downarrow}\rangle c^{A\dagger}_{xy\downarrow}c^{B\dagger}_{xy\uparrow}\\ &+ V^B_{xx}\langle c^A_{xy+1\downarrow}c^B_{xy\uparrow}\rangle c^{B\dagger}_{xy\uparrow}c^{A\dagger}_{xy+1\downarrow} + V^B_{xx+1}\langle c^A_{x+1y+1\downarrow}c^B_{xy\uparrow}\rangle c^{B\dagger}_{xy\uparrow}c^{A\dagger}_{x+1y+1\downarrow}\end{aligned}$$

$$+ \quad V^A_{x-1x}\langle c^B_{x-1y\downarrow}c^A_{xy\uparrow}\rangle c^{A\dagger}_{xy\uparrow}c^{B\dagger}_{x-1y\downarrow} + V^A_{xx}\langle c^B_{xy\downarrow}c^A_{xy\uparrow}\rangle c^{A\dagger}_{xy\uparrow}c^{B\dagger}_{xy\downarrow}] + h.c. \qquad \text{(C.12)}$$

The Fourier transform applied to Eq. (C.12) will lead to:

$$\begin{aligned}
\mathcal{H}_{nn} &= \frac{1}{N}\sum_{xk} e^{ika\sqrt{2}/2}\Delta^{-A\uparrow B\downarrow}_{xx}c^{B\dagger}_{x\downarrow}(-k)c^{A\dagger}_{x\uparrow}(k) \\
&+ e^{ika\sqrt{2}/2}\Delta^{-A\uparrow B\downarrow}_{xx+1}c^{B\dagger}_{x\downarrow}(-k)c^{A\dagger}_{x+1\uparrow}(k) \\
&+ e^{-ika\sqrt{2}/2}\Delta^{+B\uparrow A\downarrow}_{xx-1}c^{A\dagger}_{x\downarrow}(-k)c^{B\dagger}_{x-1\uparrow}(k) \\
&+ e^{-ika\sqrt{2}/2}\Delta^{+B\uparrow A\downarrow}_{xx}c^{A\dagger}_{x\downarrow}(-k)c^{B\dagger}_{x\uparrow}(k) \\
&+ e^{-ika\sqrt{2}/2}\Delta^{+A\downarrow B\uparrow}_{xx}c^{B\dagger}_{x\uparrow}(k)c^{A\dagger}_{x\downarrow}(-k) \\
&+ e^{-ika\sqrt{2}/2}\Delta^{+A\downarrow B\uparrow}_{xx+1}c^{B\dagger}_{x\uparrow}(k)c^{A\dagger}_{x+1\downarrow}(-k) \\
&+ e^{ika\sqrt{2}/2}\Delta^{-B\downarrow A\uparrow}_{xx-1}c^{A\dagger}_{x\uparrow}(k)c^{B\dagger}_{x-1\downarrow}(-k) \\
&+ e^{ika\sqrt{2}/2}\Delta^{-B\downarrow A\uparrow}_{xx}c^{A\dagger}_{x\uparrow}(k)c^{B\dagger}_{x\downarrow}(-k) \qquad \text{(C.13)}
\end{aligned}$$

where the order parameters, after we use the Bogoliubov - Valatin transformations, can be written as

$$\begin{aligned}
\Delta^{-A\uparrow B\downarrow}_{xx} &= \frac{1}{N}\sum_n\sum_k e^{-ika\sqrt{2}/2}V^B_{xx}[u^{Bx}_n(k)v^{Ax*}_n(k)f_n(k) - u^{Ax}_n v^{Bx\star}_n(1-f_n(k))] \\
\Delta^{-A\uparrow B\downarrow}_{xx+1} &= \frac{1}{N}\sum_n\sum_k e^{-ika\sqrt{2}/2}V^B_{xx+1}[u^{Bx}_n(k)v^{Ax+1*}_n(k)f_n(k) - u^{Ax+1}_n v^{Bx\star}_n(1-f_n(k))] \\
\Delta^{+B\uparrow A\downarrow}_{xx-1} &= \frac{1}{N}\sum_n\sum_k e^{ika\sqrt{2}/2}V^A_{x-1x}[u^{Ax}_n(k)v^{Bx-1*}_n(k)f_n(k) - u^{Bx-1}_n v^{Ax\star}_n(1-f_n(k))] \\
\Delta^{+B\uparrow A\downarrow}_{xx} &= \frac{1}{N}\sum_n\sum_k e^{ika\sqrt{2}/2}V^A_{xx}[u^{Ax}_n(k)v^{Bx*}_n(k)f_n(k) - u^{Bx}_n v^{Ax\star}_n(1-f_n(k))] \\
\Delta^{+A\downarrow B\uparrow}_{xx} &= -\frac{1}{N}\sum_n\sum_k e^{ika\sqrt{2}/2}V^B_{xx}[u^{Bx}_n(k)v^{Ax*}_n(k)f_n(k) - u^{Ax}_n v^{Bx\star}_n(1-f_n(k))] \\
\Delta^{+A\downarrow B\uparrow}_{xx+1} &= -\frac{1}{N}\sum_n\sum_k e^{ika\sqrt{2}/2}V^B_{xx+1}[u^{Bx}_n(k)v^{Ax+1*}_n(k)f_n(k) - u^{Ax+1}_n v^{Bx\star}_n(1-f_n(k))] \\
\Delta^{-B\downarrow A\uparrow}_{xx-1} &= -\frac{1}{N}\sum_n\sum_k e^{-ika\sqrt{2}/2}V^A_{x-1x}[u^{Ax}_n(k)v^{Bx-1*}_n(k)f_n(k) - u^{Bx-1}_n v^{Ax\star}_n(1-f_n(k))] \\
\Delta^{-B\downarrow A\uparrow}_{xx} &= -\frac{1}{N}\sum_n\sum_k e^{-ika\sqrt{2}/2}V^A_{xx}[u^{Ax}_n(k)v^{Bx*}_n(k)f_n(k) - u^{Bx}_n v^{Ax\star}_n(1-f_n(k))]
\end{aligned}$$

For each momentum k in the y direction the Hamiltonian describes an inhomogeneous chain of size $2N_x$, where N_x is the number of cells in the x direction.

Appendix D

Andreev levels, 1D N/S system

Andreev reflection occurs at the interface between a normal metal and a superconductor [124, 127]. Incoming electrons with energy lower than the superconducting gap cannot enter the superconductor as there are no allowed states below the gap. The only allowed process is the transmission of a Cooper pair. This implies that a hole will be reflected back.

The electronic excitation spectra can be calculated analytically for a one-dimensional system [125, 131], as the one shown in Figure D.1.

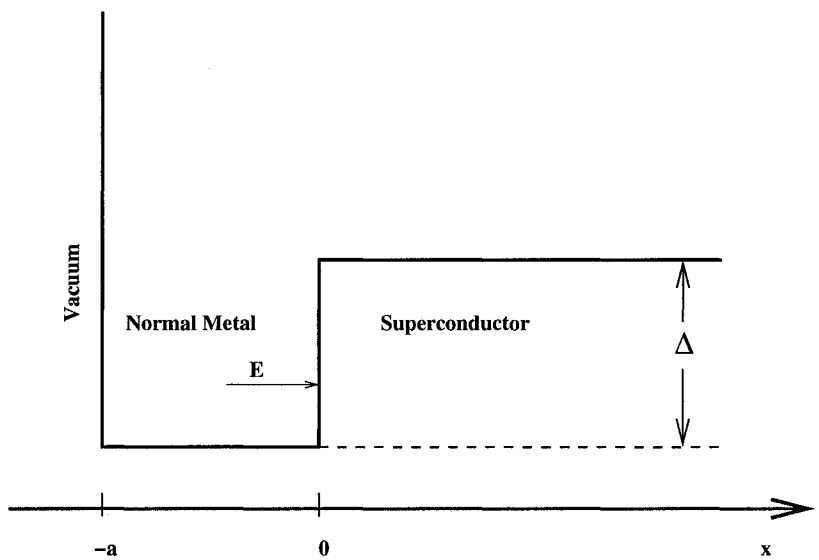

Figure D.1: NS interface near a normal metal-vacuum surface

This system is described by the Bogoliubov-de Gennes equations, $H\Phi(x) = E\Phi(x)$. The wave function has two components $u(x)$ and $v(x)$, while the Hamiltonian is a 2×2

matrix.

$$\begin{pmatrix} -\frac{\hbar}{2m}\nabla^2 - E_F & \Delta(x) \\ \Delta^*(x) & \frac{\hbar}{2m}\nabla^2 + E_F \end{pmatrix} \begin{pmatrix} u(x) \\ v(x) \end{pmatrix} = E \begin{pmatrix} u(x) \\ v(x) \end{pmatrix} \tag{D.1}$$

We are interested in finding the wave functions for energies smaller than the superconducting order parameter. An incoming electron from the superconducting side with $E < \Delta$ cannot enter the superconductor, as the density of states below the gap is zero. This electron will be confined in the normal-metal region. We can split the problem in two cases: $-a < x < 0$ and $x > 0$. For $x < 0$, $\Delta(x) = 0$ and the equations become decoupled, describing an electron and a hole.

$$\left(-\frac{\hbar}{2m}\nabla^2 - E_F\right) u(x) = Eu(x) \tag{D.2}$$

$$\left(\frac{\hbar}{2m}\nabla^2 + E_F\right) v(x) = Ev(x) \tag{D.3}$$

Using the fact that the wave function has to be zero at the interface with the vacuum, one can write the solution of these equations:

$$u(x) = Asin[k_e(x+a)] \tag{D.4}$$

$$v(x) = Bsin[k_h(x+a) - n\pi] \tag{D.5}$$

where $k_e = \sqrt{\frac{2m(E_F+E)}{\hbar^2}} \approx k_F + k$ and $k_h = \sqrt{\frac{2m(E_F-E)}{\hbar^2}} \approx k_F - k$ are the electron and hole momenta.

For $x > 0$ the order parameter is considered to be constant $\Delta(x) = \Delta$, and the BdG equations take the form:

$$\left(-\frac{\hbar}{2m}\nabla^2 - E_F\right) u(x) + \Delta v(x) = Eu(x) \tag{D.6}$$

$$\left(\frac{\hbar}{2m}\nabla^2 + E_F\right) v(x) + \Delta^* u(x) = Ev(x) \tag{D.7}$$

Substituting $v(x)$ from Eq. (D.6) into Eq. (D.7) we obtain the following equation for $u(x)$:

$$\left[\left(\frac{\hbar^2}{2m}\nabla^2\right)^2 + 2E_F\frac{\hbar^2}{2m}\nabla^2 + |\Delta|^2 + E_F^2 - E^2\right] u(x) = 0 \tag{D.8}$$

We substitute in Eq. (D.8) a solution of form $u(x) = \alpha e^{kx}$:

$$k^4 + 2E_F k^2 + \Delta^2 + E_F^2 - E^2 = 0 \tag{D.9}$$

The solutions of this 4-th order equation are:

$$k_{1,2} = - \sqrt{\frac{\hbar^2}{2m}}\sqrt{-E_F \pm i\Omega} \tag{D.10}$$

$$k_{3,4} = + \sqrt{\frac{\hbar^2}{2m}}\sqrt{-E_F \pm i\Omega} \tag{D.11}$$

where $\Omega = \sqrt{\Delta^2 - E^2}$.

For the required boundary conditions to be satisfied, only $k_{1,2}$ is a valid solution. We want only evanescent waves for energies less than the superconducting gap. Writting $k_{1,2}$ explicitly as a complex number and keeping only the lowest order in Ω/E_F^2 we get:

$$k_{1,2} = -\frac{1}{\xi_0}\frac{\Omega}{\Delta} \pm ik_F(1 + \Omega^2/E_F^2), \tag{D.12}$$

where $\xi_0 = \hbar v_F/\Delta$, $v_F = \sqrt{2E_F/m}$. The general form of the $u(x)$ solution can be written as:

$$u(x) = \alpha_1 e^{-\frac{1}{\xi_0}\frac{\Omega}{\Delta}x} e^{ik_F(1+\Omega^2/E_F^2)} + \alpha_2\alpha_1 e^{-\frac{1}{\xi_0}\frac{\Omega}{\Delta}x} e^{ik_F(1+\Omega^2/E_F^2)} \tag{D.13}$$

Substituting this form into Eq. (D.6), one can obtain the hole part of the wave function:

$$v(x) = \beta_1 e^{-\frac{1}{\xi_0}\frac{\Omega}{\Delta}x} e^{ik_F(1+\Omega^2/E_F^2)} + \beta_2\alpha_1 e^{-\frac{1}{\xi_0}\frac{\Omega}{\Delta}x} e^{ik_F(1+\Omega^2/E_F^2)}, \tag{D.14}$$

where $\beta_1/\alpha_1 = E/\Delta + i\Omega/\Delta$ and $\beta_2/\alpha_2 = E/\Delta - i\Omega/\Delta$. One can show that $E/\Delta \pm i\Omega/\Delta$ is a complex number with unit magnitude and will only contribute as a phase difference between the electron and hole wave functions (Φ_A):

$$\Phi_A = -\arctan\frac{\Omega}{E} \tag{D.15}$$

$$= -\arccos\frac{E}{\Delta} \tag{D.16}$$

$$= \arcsin\frac{\Omega}{\Delta}, \tag{D.17}$$

$-\pi/2 < \Phi_A < 0$.

We can now write a general form of the solution for $x > 0$ and $E < \Delta$:

$$u(x) = \alpha sin[k_F x + \phi_e] e^{-\frac{\sin\Phi_A}{\xi_0}x} \tag{D.18}$$

$$v(x) = \alpha sin[k_F x + \phi_e - \Phi_A] e^{-\frac{\sin\Phi_A}{\xi_0}x} \tag{D.19}$$

The continuity of the wave function and of it's first derivative at $x = 0$ will give the final solution:

$$\begin{cases} u(x) = Asin[k_e(x+a)] & -a < x < 0 \\ v(x) = Asin[k_h(x+a) - n\pi] & -a < x < 0 \end{cases} \tag{D.20}$$

$$\begin{cases} u(x) = Asin(k_F x + k_e a)e^{-\frac{\sin\Phi_A}{\xi_0}x} & x > 0 \\ v(x) = Asin(k_F x + k_h a - n\pi)e^{-\frac{\sin\Phi_A}{\xi_0}x} & x > 0 \end{cases} \tag{D.21}$$

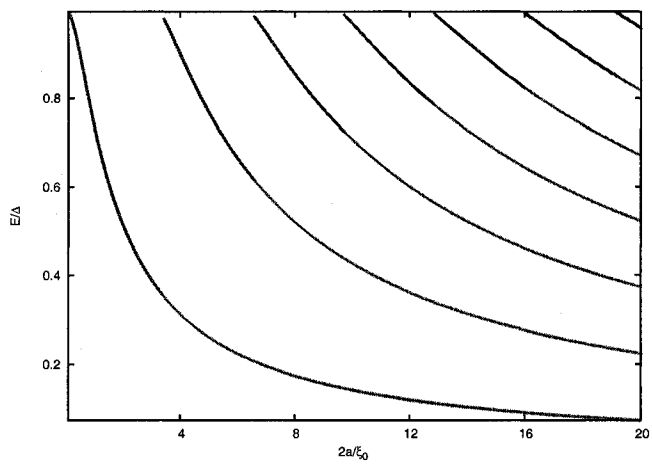

Figure D.2: Position of the Andreev levels as a function of the size of the normal-metal layer

The phase difference between the electron and the hole wave function obeys the following condition:

$$2ka + \Phi_A = n\pi \tag{D.22}$$

If one substitutes the definitions for Φ_A and k as functions of excitation energy E, one obtains a quantization condition:

$$\frac{2a}{\xi_0}\frac{E}{\Delta} = n\pi + \arccos\frac{E}{\Delta} \tag{D.23}$$

In Figure D.2 we plot the energies of the Andreev levels as a function of the length of the normal-metal layer. The number of Andreev levels is proportional to the length of the normal-metal layer a and inverse to the superconducting coherence length. For $a \ll \xi_0$ there is always one Andreev state which as a decreases, is shifted towards the gap edge.